ADVANCEMENTS IN PROCESS DEVELOPMENT AND MECHANICAL PROPERTIES OF RECYCLED GLASS BUILDING MATERIALS THROUGH EXPERIMENTATION AND ANALYTICAL MODELING

Renuka Prabhakar

A dissertation
submitted in partial fulfillment of the
requirements for the degree of

Doctor of Philosophy

University of Washington
2017

Reading Committee:
Ramulu Mamidala, Chair
Per Reinhall
Mark Tuttle

Program Authorized to Offer Degree:
Mechanical Engineering

ABSTRACT

Over the past 50 years U.S. consumers and municipalities have made efforts to decrease landfill waste and reduce raw material extraction through recycling. The rate of recycling has risen tenfold over that time period and many materials, such as paper and aluminum, can be efficiently and effectively recycled into new products. However, this is often not the case for glass. Currently, over 11 million tons of post-consumer glass enters the municipal solid waste stream annually and the majority is collected for recycling. Unfortunately, less than 30% of the collected glass is successfully recycled into new products, while the remaining ~7.5 million tons is ultimately sent to landfills.

A new, energy efficient glass recycling technology is being developed at EnVitrum, Inc., a UW spinout based in Seattle. The process uses waste glass as the primary feedstock in the manufacture of high recycle-content building materials. This technology is compatible with post-consumer and post-industrial waste glass and may provide a commercial outlet for the vast quantities of post-consumer glass that cannot be recycled using current technology. Moreover, due to reduced process temperatures and densification times, the materials produced through this process would have lower embodied energy and shorter production cycle times than traditional products. This would be of great benefit to potential manufacturers and in addition, the end-products resulting from this process would provide the construction industry with a sustainable material alternative.

During the process, materials are consolidated through cold isostatic pressing and then densified at temperatures up to 55% lower than the melting temperature. Initial studies conducted by Marchelli and Prabhakar at EnVitrum, showed that densification through warm working was found to be compatible with common contaminants present in the glass waste stream and the

process resulted in porous materials that possessed up to 95% recycle content. In 2012, an exploratory study was undertaken by Prabhakar and the results indicated that overall, the physical and mechanical behavior of the material could be predictably calibrated by modification of process parameters (primarily densification temperature). However, the results presented were preliminary and it was hypothesized that inconsistencies stemmed from issues associated with processing. Therefore, advanced improvements of the process will be needed.

The purpose of the research described herein was to i) investigate improvements to material processing conditions that may have affected the preliminary results, ii) characterize the physical & mechanical behavior with respect to peak densification temperature, and iii) compare the mechanical properties to zero porosity values and evaluate the suitability of established porosity-property correlations. Through this work, several improvements were made to the formation and densification processes. As a result, it was determined that Marchelli and Prabhakar's process is compatible with post-consumer waste glass and high strength materials can be created at lower temperatures than indicated by previous investigations. Most importantly, the findings agree with Prabhakar's earlier assertion that the mechanical behavior of the material could be predictably calibrated by modification of process parameters and it was found that materials with sufficient strength for a variety of construction applications could be produced.

TABLE OF CONTENTS

LIST OF FIGURES

LIST OF TABLES

CHAPTER 1. INTRODUCTION & BACKGROUND

In recent years, there has been a growing desire to integrate waste stream materials into feedstocks for the manufacture of new products. There are three primary reasons for this shift: resource conservation, reduction of costs associated with solid waste storage and infrastructure, and reduction of manufacturing costs. For many materials, particularly metals and paper products, recycling techniques have been very successful; however, this is not the case with glass.

Although pure glass is infinitely recyclable, waste glass commonly found in the solid waste stream is littered with contaminants and because of this, current recycling methods for glass are extremely energy intensive and costly. This inefficiency has contributed to very low recycling rates. In 2013, 11.5 million tons of glass entered the municipal solid waste stream. Merely 27% of the glass waste stream was recovered for recycling, with the remaining 73% accumulating at solid waste facilities, amplifying the need for waste storage infrastructure [1].

New recycling technologies must be developed in order to turn waste stream glass into a raw material source for new products that are both environmentally responsible and economically viable. The research described in this document will build upon prior work conducted by Marchelli and Prabhakar at the University of Washington (UW) startup, EnVitrum[2]. In this work, pulverized glass was combined with organic binders, formed into green compacts via cold isostatic pressing (CIP) and then consolidated through a low-temperature heating process. The process was found to be compatible with contaminated glass and resulted in porous articles composed of over 95% waste glass. With funding from UW and the National Science Foundation, an exploratory evaluation of the compressive and flexural behavior was undertaken and the results indicated that these articles exhibited mechanical

properties similar to that of common porous building materials, such as masonry[3, 4]. Moreover, these materials were produced at ~45% of the melting temperature and data acquired through Prabhakar and Marchelli's work indicated that the embodied energy of these articles was nearly 70% lower than that of clay brick and 75% lower than that of common container glass.

However, a good deal of the data collected during mechanical testing in these initial studies was not well behaved, particularly in the lower porosity ranges. It was hypothesized that this was a direct result of inconsistencies in specimen preparation and/or data collection. The purpose of the proposed work is to investigate potential sources of error, reevaluate the compressive and flexural behavior of the EnVitrum's glass articles and compare the experimental data to existing experimentally and analytically derived models for approximating the strength and elastic modulus of sintered materials based on specimen porosity or relative density.

1.1 Overview of Solid Waste Recovery & Recycling

To understand the issues encountered with current glass recycling technologies, it is first necessary to understand the differences in where solid waste is generated and how it is handled. The four broadest areas of solid waste generation are i) industrial wastes, ii) municipal wastes, iii) hazardous wastes and iv) construction wastes. Each type of waste is handled separately and typically with separate infrastructure. As hazardous waste does not co-mingle with other types of waste, it is not relevant to this research and will be omitted from further discussion.

Industrial and construction wastes account for a large portion of the overall waste stream. Both waste streams are primarily comprised of metal, wood and paper products, although glass is often present in the form of windows (termed "plate glass"). Because of the relatively low number of material types and relatively large per item volumes of wastes present in the industrial

and construction waste streams, most materials can be efficiently and effectively sorted and subsequently recycled. The exception here is plate glass which is separated and either used in fiberglass manufacturing, where markets exist, or handled with other unrecyclable materials.

There are several reasons for this. First, plate glass rarely enters the waste stream on its own and is often attached to metal or wooden components. Separating the glass from the other materials is very labor intensive and the process cannot be automated effectively, therefore it is very costly to do so. Second, plate glass comes in many forms and with varying compositions. For example, the glass may be tinted, tempered, laminated or in the case of some safety glass, contain embedded wire mesh. These variations make sorting and subsequent recycling of plate glass cost prohibitive.

The last and most problematic category of waste is Municipal Solid Waste (or MSW), which includes waste generated at residential, commercial, and institutional locations. Recycling (or recovery) rates for even metals and paper products are significantly lower. National data on 2012 collection and recovery rates for various materials can be seen in Table 1-1.

Table 1-1. Generation, recovery and discard weights of materials in MSW (weights given in millions of tons)[5].

Material	Weight Generated	Weight Recovered	Recovery as Percent of Generation	Weight Discarded
Paper and paperboard	68.62	44.36	64.6%	24.26
Glass	11.57	3.20	27.7%	8.37
Metals				
Steel	16.80	5.55	33.0%	11.25
Aluminum	3.58	0.71	19.8%	2.87
Other nonferrous metals†	2.00	1.36	68.0%	0.64
Total metals	**22.38**	**7.62**	**34.0%**	**14.76**
Plastics	31.75	2.80	8.8%	28.95
Rubber and leather	7.53	1.35	17.9%	6.18
Textiles	14.33	2.25	15.7%	12.08
Wood	15.82	2.41	15.2%	13.41
Other materials	4.60	1.30	28.3%	3.30
Total materials in products	**176.60**	**65.29**	**37.0%**	**111.31**
Other wastes				
Food, other‡	36.43	1.74	4.8%	34.69
Yard trimmings	33.96	19.59	57.7%	14.37
Miscellaneous inorganic wastes	3.90	Negligible	Negligible	3.90
Total other wastes	**74.29**	**21.33**	**28.7%**	**52.96**
Total municipal solid waste	**250.89**	**86.62**	**34.5%**	**164.27**

† Includes lead from lead-acid batteries.
‡ Includes recovery of other MSW organics for composting.
Details might not add to totals due to rounding.
Negligible = less than 5,000 tons or 0.05 percent.

The table shows that the recovery rate (by weight) for glass in 2012 was 27.7%. From the table, we can also see that the total weight of glass waste generated was 11.57 million tons, which represents only ~4.6% of the total MSW stream and ~6.55 percent of the total materials collected from products (i.e. containers, packaging, durable goods, etc.). Although these may not seem like significant percentages at first, it is important to consider that unlike many other materials on the list, glass will never biodegrade and the impact of storing waste materials will only compound over time. In addition, the embodied energy of glass products is among the

highest of the materials present in MSW. That is, the energy expended in making glass products is extremely high, due to the fact that glass manufacturing processes are executed while the material is in its molten state; melting temperatures are quite high and temperatures must be held for long periods of time to minimize defects.

The majority of collected glass can be found in this waste stream in the form of containers. Of the recovered glass, nearly 90% is used to reduce the energy and materials costs associated with container manufacturing, where it was combined with traditional virgin materials. Unfortunately, the container glass manufacturing process is extremely sensitive to contaminants present in the waste stream, such as paper, plastic, metal, ceramics and adhesives. Even colored glasses are considered contaminants; their varying composition and melting temperatures have been shown to increase the number of defects present in finished products. These defects include pores, voids, micro-cracks, and inclusions. Therefore, before recovered glass can be used in container production, it must undergo intensive sorting and cleaning operations.

The energy expended on these processes is barely offset by the energy saved through diluting the virgin material stream; in fact, when the virgin materials are diluted by 10%, overall energy consumption is reduced by a scant 2-4%[1]. Moreover, manufacturers have found that as the percentage of post-consumer glass is increased, the quality of the manufactured container goes down in terms of both mechanical performance and aesthetics.

1.2 Collection & Processing of MSW Glass

The first recycling program for MSW glass in the United States was introduced in Oregon in 1971[6]. This took the form of the first US container deposit legislation, which was originally utilized in Ireland in the late 1700s. Essentially, container deposit legislation (CDL or

"bottle bills" as they are commonly known) is a state or federal law that requires that consumers pay a monetary deposit on goods that are sold in a specified type of packaging. This encourages consumers to participate in collection programs and also ensures that materials are not mingled with MSW and thus minimizes the opportunity for those materials to be contaminated with other materials as they make their way through the collection process. This method is extremely effective and municipalities within the reach of CDL have excellent recovery and recycling rates. Outside of the United States, many countries have successfully adopted this strategy. Within the United States, only nine additional states have successfully adopted such laws after the Oregon Bottle Bill was introduced.

Aside from a few states that quickly implemented CDL after Oregon, not a single curbside recycling program existed in the United States until 1973. At that time, the City of Berkeley began separated collection and recycling of newspapers. Other municipalities begin to follow suit and with the success of newspaper recycling, slowly began to separate collection of other products, such as aluminum cans and glass bottles. As recycling programs began gaining popularity, the first single-stream MSW processing plants opened in the United States. Single-stream recycling refers to the co-mingled collection of all recyclable wastes. This method has several advantages over the multi-stream collection and recovery method:

1. This method has been shown to increase recovery rates by an average of 30%[7].
2. The cost of curbside collection is reduced. The labor associated with picking up several containers and ensuring that they are correctly deposited on the collection vehicle is eliminated. As such collection time is reduced, as is the number of vehicles required[8].
3. With this method, it is easier to add new materials to the list of those acceptable for collection.

However, because the different wastes are co-mingled, there are important disadvantages to consider as well:

1. This method requires additional sorting at a Materials Recovery Facility (MRF). Sorting materials is costly, in terms of both and capital expenditures and labor.
2. With this method, no amount of sorting will eliminate cross-contamination, which in turn drives commodity prices down.
3. In the case of container glass, breakage is inevitable and recovery of material becomes much more difficult.

Of the >8,000 municipal recycling programs now active in the United States, over 64% utilize the single-stream collection method. Despite recent criticism of this method due to the increase in residual (or highly contaminated) materials and the subsequent reduction in percentage of useable recovered materials, single-stream recycling is unlikely to be replaced. The cost of implementing other methods outweighs the benefit to materials processing companies. Instead, more elaborate sorting methods have been developed and with respect to glass, an industry has arisen to deal with the broken and crushed glass (termed “cullet”) that cannot be handled effectively and efficiently at a primary MRF. An overview of the lifecycle of a typical glass container processed using single-stream collection can be seen in Figure 1-1.

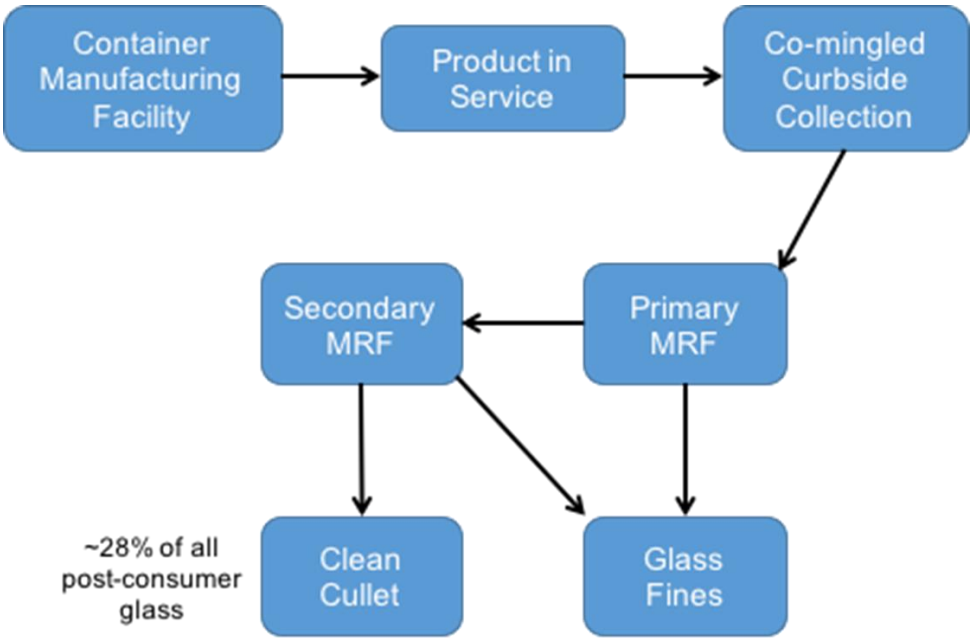

Figure 1-1. Overview of glass container lifecycle.

Once recyclables are collected through single-stream, curbside collection programs, they are sent to the primary MRF, where a variety of mechanical sorting methods are utilized to separate the waste stream into various commodity streams. The majority of these mechanisms leverage the density difference between different materials as the primary method of sorting and employ compressed air, magnets or in some special cases, infrared technology to assist. In almost all primary MRFs, a portion of the sorting and/or quality control measures are carried out by hand.

While the co-mingled recycling stream is being separated in this manner, the glass cullet is further degraded into smaller pieces. The larger pieces are easily removed from the waste stream, but primary MRF processes are not typically equipped to remove any cullet below 3/8-inch (this material is termed “3/8 minus” or “glass fines”). At this point, the glass cullet is sold to a secondary MRF that specializes in glass sorting. The commodity pricing is dependent on size and quality and the secondary MRF is predominantly interested in the larger, cleaner cullet. The

primary MRF must actually pay to have the secondary MRF accept delivery of the 3/8 minus material. This is because the 3/8 minus output is very heavily contaminated with paper, plastic and cardboard scraps (Figure 1-2). In fact, although the 3/8 minus material typically contains 40% glass by weight, it is so contaminated that, without the need for any sort of containment, it can actually be tightly compressed and baled with wire for shipping.

Figure 1-2. 3/8 minus material ready for baling.

The processes at the secondary MRF are much more sophisticated, often employing proprietary technologies that utilize lasers, optical systems and elaborate compressed air systems that can deliver focused puffs of air to individual glass pieces. The purpose of all of this is to sort the glass by color, so it can be sent to traditional container manufacturing facilities and combined in low quantity with virgin raw materials. (As mentioned earlier, glass container manufacturing processes are extremely sensitive to color.) Unfortunately, even after all of these processes are employed, only 27.7% of the glass collected from MSW is actually recycled into new products. In order to recover and reuse a larger percentage of the glass waste stream, new technologies must be developed that are compatible with “dirty” glass fines that contain colored glass and a variety of contaminants.

CHAPTER 2. LITERATURE REVIEW

The literature reviewed for the current study will be discussed in this chapter. The chapter is organized into three main sections. In the first section, literature regarding relevant glass technology and mechanical properties are described. In the following section, experimental investigations of alternative glass processing techniques are discussed. In the third section, established correlations developed to describe the relationship between porosity and mechanical properties in porous ceramics are presented and discussed.

2.1 GLASS TECHNOLOGY & MECHANICAL PROPERTIES

2.1.1. SODA-LIME SILICATE GLASS

Glass has been produced for 1000s of years and in that time many different compositions have been formulated. Today, glass is used primarily in the manufacture of containers and windowpanes. Plate or sheet glass and container or bulb glass can be manufactured through a variety of processes, all of which involve melting the virgin materials at temperatures of up to 1800°C. The majority of these glasses fall into the soda-lime silicate category and exhibit lower melting temperatures than glasses belonging to other families. Soda-lime silicate glasses are generally composed of 65-75% SiO_2, 13-18% Na_2O, 6-12% CaO, 0-7% K_2O 0-4.5% MgO, 0-4% Al_2O_3 and 0-1% Fe_2O_3 by weight[9-11]. The composition directly affects the mechanical properties of the resulting products and manufacturers adjust this for specific applications. Published values for the relevant physical and mechanical properties of common soda-lime silicate glasses are given in Table 2-1, on the following page.

Table 2-1. Physical and mechanical properties of common soda-lime silicate glasses.

Glass Type	Density (g/cm^3)	Compressive Strength (MPa)	Flexural Strength (MPa)	Elastic Modulus (GPa)	Poisson's Ratio
soda-lime silicate plate[12]	2.5				
Asahi AS soda-lime silicate[10]	2.49				
soda-lime silicate[13]	2.5				
soda glass[14]		2000-3000			
soda-lime silicate bulb[15]			102		
soda-lime silicate[11]			166		
soda-lime silicate[11]			135		
soda-lime silicate plate[12]				74	
soda-lime silicate[11]				67.1	
soda-lime silicate bulb[15]				70.3	
Asahi AS soda-lime silicate[10]				71.7	
soda-lime silicate[13]				69	
soda-lime silicate plate[12]					0.22
soda-lime silicate bulb[15]					0.24
soda-lime silicate[11]					0.215
Asahi AS soda-lime silicate[10]					0.21

2.1.2. Densification Through Sintering

Sintering is a powder process widely used in the manufacture of metals, plastics, ceramics and glasses. The powdered materials are first consolidated at high pressure and then densified through a heating process[16-19]. Densification takes place in four stages, which are shown in Figure 2-1 [20].

During the first stage in the densification process, the viscosity of the particles is reduced sufficiently to allow for the material to flow. This occurs slightly above the glass transition temperature, which for soda-lime silicate glasses is ~615°C. The particles begin to soften and behave in a more rubbery manner, which allows them to settle and become more densely packed. This increases the contact area between adjacent particles and they begin to fuse together.

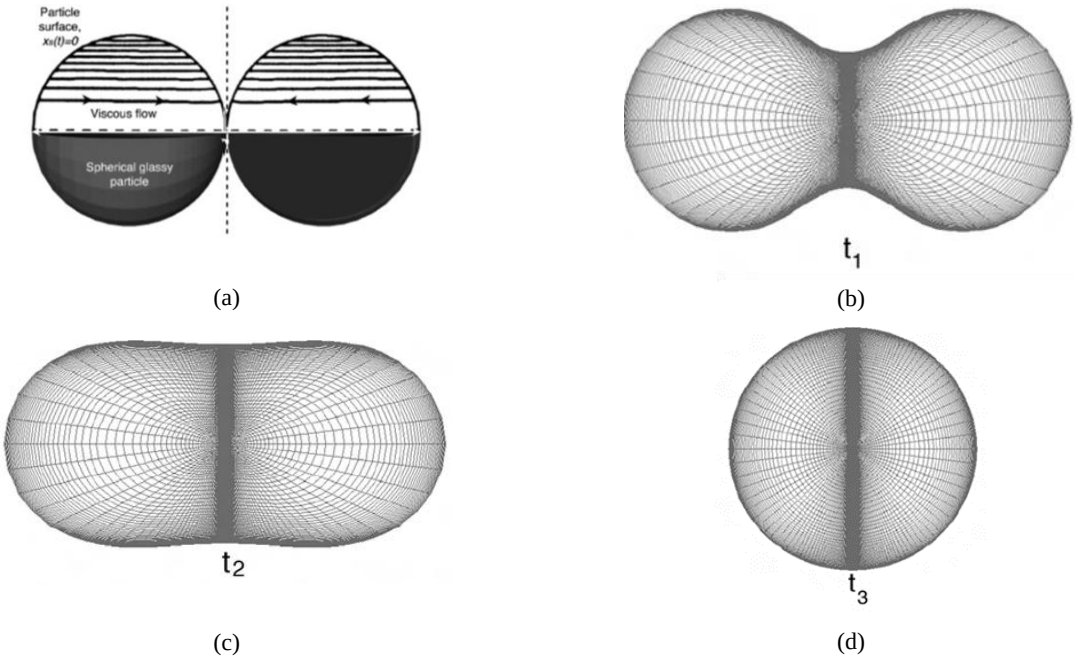

Figure 2-1. Graphical representation of necking between particles during the sintering process. (a) Depicts direction of viscous flow. b) Depicts contact area between particles at t=0. (c) Depicts the formation of a neck.

The second stage in the process occurs once the glass transition temperature is exceeded [20]. This stage is characterized by the onset of interparticle "necking". This behavior is driven by the system's need to reach a more favorable energy state. The free energy density is greater at the surface of a particle and the creation of necks reduces the total surface area of the bulk material, which in turn reduces the surface energy of the particle system. This can take place through a variety of mass transport processes and in glasses the predominant process is viscous flow. As the temperature is further increased, the particles continue to expand and are driven closer together, increasing the number of interparticle contact points and subsequently the number of necks. It is during the second stage that the porous network begins to form.

The third stage of sintering occurs as the temperature is further increased to the dilatometric softening point, the necks continue to grow while grain and pore formation begins. These phenomena cause alterations in the distribution of stress throughout the bulk material. As the stress distribution changes, the particles to move and twist in response, which typically

results in compaction of the bulk material. In fact, volumetric changes to the bulk material are most pronounced during this stage in the densification process.

The final stage of sintering is known as the crystallization stage and during this stage grain growth dominates. As the grains become larger, they begin to engulf the pores and isolate them from the porous network. After full crystallization, only a small percentage of isolated pores will continue to exist within the resulting solid body. In soda-lime silicate glasses crystallization takes places between ~750 and 975°C.

2.1.3. Mechanical Properties

The uniaxial compression test is a common technique for establishing the compressive strength of materials. Load and displacement data are used to calculate the engineering stress and strain at many points during testing using Equations 2.1 and 2.2, where σ_c is defined as the compressive stress, P_c is the compressive load, A_o is the initial cross sectional area of the specimen perpendicular to loading direction, Δl is the change in thickness of the specimen, and l_o is the initial thickness[21, 22].

$$\sigma_c = P_c/A_o \tag{2.1}$$

$$\varepsilon = \left(\frac{\Delta l}{l_o}\right) \tag{2.2}$$

In pure compression, the fracture plane is expected to form a 45° angle with the plane of maximum principal stress. This can be demonstrated using Mohr's circle (Figure 2-2) and Equation 2.3, where τ_{max} is the maximum shear stress and σ_1 and σ_2 are the principal stresses[21, 22]. In the case of pure compression σ_1 is equal to zero and solving for θ yields 45°.

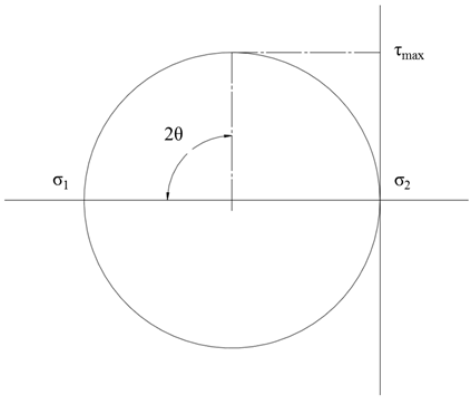

Figure 2-2. Mohr's circle for uniaxial compression.

$$\tau_{max} = \frac{(\sigma_1 - \sigma_2)\sin 2\theta}{2} \tag{2.3}$$

Brittle and porous materials are seldom subjected to pure tensile stresses in service, as their tensile strength is almost invariable much lower than their compressive strength. Further, tensile testing is often unsuccessful or yields inaccurate values of tensile strength, as failure generally occurs very near the grips. During the characterization of brittle material researchers often forego tensile testing in favor of flexural testing. This provides data regarding the transverse strength (or transverse rupture strength) of the specimen, which describes the material's ability to resist deformation under transverse loads, as well as data regarding the material's elastic modulus in flexure. Because of its relative ease, flexural testing is most commonly performed via the 3-point bending test, as shown in Figure 2-3, on the following page.

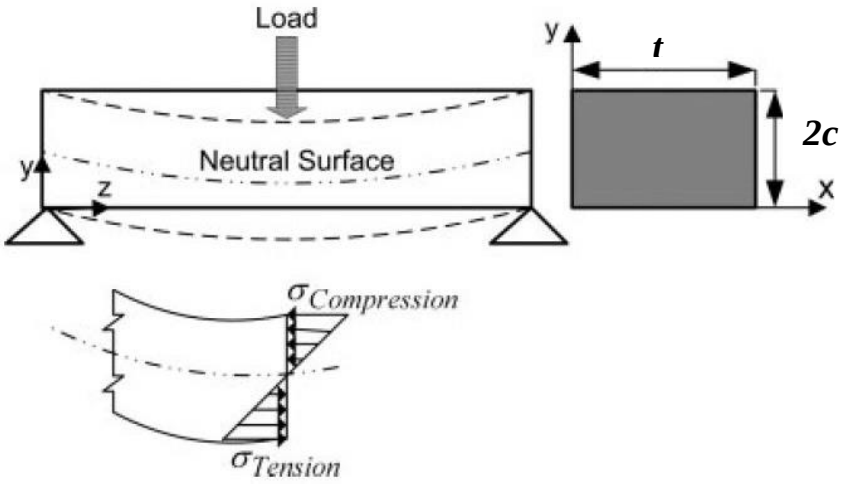

Figure 2-3. Prismatic specimen in 3-point bending.

In Figure 2-3, the upper left image depicts a prismatic specimen under 3-point loading. The specimen is supported on the underside in two locations and the load is applied from above at equal distance from both supporting members. The upper right image shows the cross-sectional view of a typical specimen. The lower image depicts the distribution of stresses induced in the specimen normal to the direction of loading, where it can be seen that the stresses vary with depth. The uppermost fibers are subjected to compressive stresses, while the bottommost fibers are subjected to tensile stresses. The central plane of the specimen is subjected to no stresses at all and is termed the neutral surface. The transverse stress in a specimen subjected to 3-point bending is given by Equation 2.6[21, 22], where σ_t is the transverse stress, M is the bending moment, I is the area moment of inertia, c is the distance from the neutral plane, P is the applied load, L is the support span, t is the width of the specimen. The transverse strain is defined as in Equation 2.7, where D is the deflection of the beam directly under the load.

$$\sigma_t = \frac{Mc}{I} \tag{2.4}$$

$$M = \frac{PL}{4} \tag{2.5}$$

$$I = \frac{2tc^3}{3} \tag{2.6}$$

$$\sigma_t = \frac{3PL}{8tc^2} \tag{2.7}$$

$$\varepsilon = \frac{12Dc}{L^2} \tag{2.8}$$

The elastic modulus describes a material's ability to undergo elastic deformation when subjected to loading. The elastic modulus can be calculated from the stress-strain data acquired through compressive, tensile or flexural testing. In isotropic materials, the values calculated from any of the three sets of data will be equivalent. In anistropic materials, these values will differ due to the inherent directionality of the material. The most common form of the elastic modulus is Young's modulus as shown in Equation 2.8, where E is Young's modulus, σ is the stress in compression, tension or flexure and ε is the corresponding strain. Young's modulus is used to describe materials that exhibit linear elastic behavior during the initial stages of loading and mathematically, it is the slope of the initial, linear portion of the stress strain curve [22].

$$E = \frac{\sigma}{\varepsilon} \tag{2.8}$$

It should be noted that although the 3-pointing test is most common, the 4-point bending test is often preferred. The differences between the two methods are illustrated in Figure 4-2.

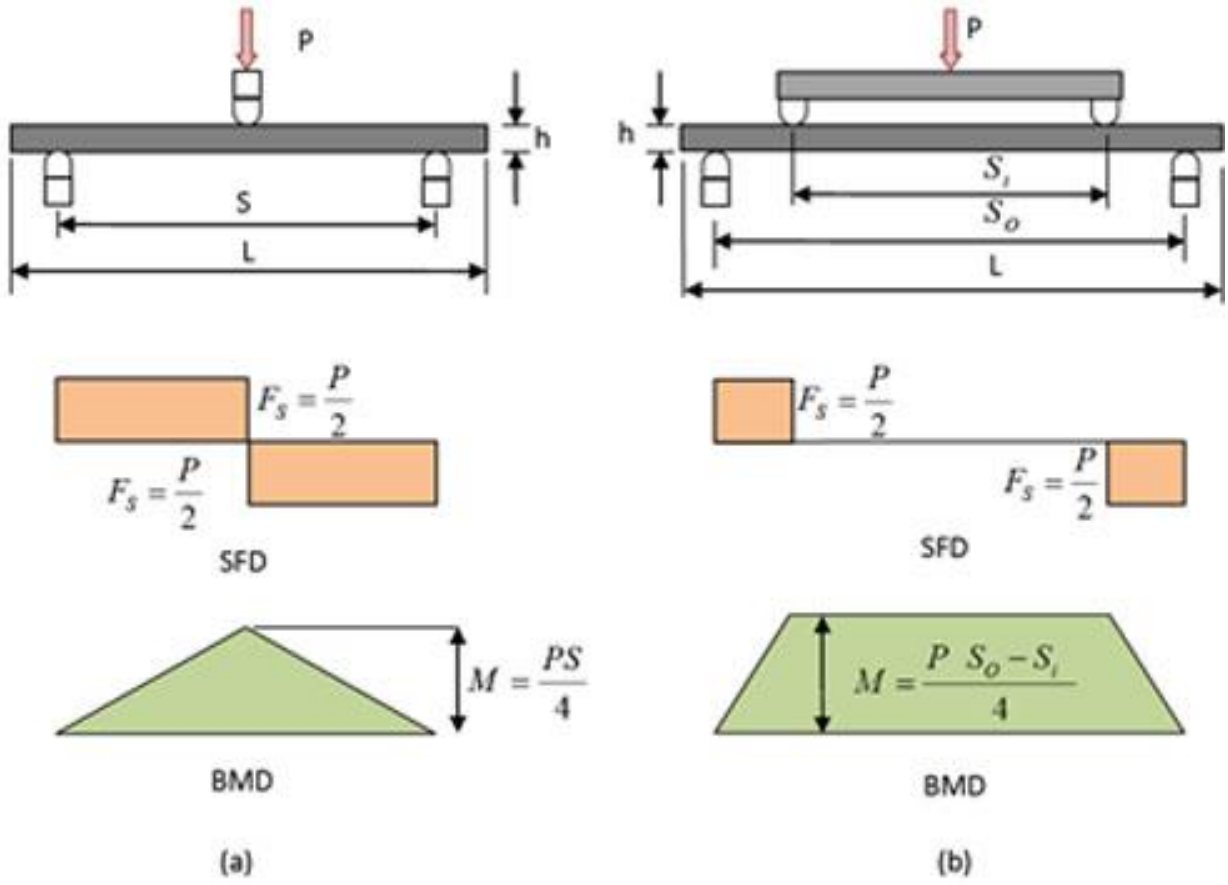

Figure 2-4. Illustration of 3-point bending setup (a) and 4-point bending setup (b).

In Figure 2-4, both test setups are shown, along with the corresponding shear force and bending moment diagrams below them. It can be seen that in 3-point bending, the specimen is subjected to both shear and bending stresses throughout the gage section. In addition, the maximum bending moment is experienced at an isolated, mid-span location. By contrast, the nature of the 4-point bending test eliminates shear stresses between the two loading surfaces and the specimen experience constant bending moment within in the gage section.

2.2. Experimental Investigations

2.2.1. Porous Glass

Porous glasses have become a topic of increased interest in recent years, particularly in the fields of confined matter, solid-phase biochemistry, optical chemosensors, composites,

membrane technology and bioengineering. The materials are typically produced through one of two processes: leaching of phase-separated alkali-borosilicate glass, or preparation via the sol-gel process[23]. The preparation of porous glass through leaching of phase-separated glass has been performed for nearly sixty years and has been the preferred method, as it produces open or closed cell materials with predictable geometry and controllable pore sizes in the 0.3-1000 nm range.

2.2.2. Foamed Glass

On a larger scale, porous glass materials have been produced for decades through foaming processes [24-28]. Materials produced via foaming are generally described as cellular, as they exhibit a large void to solid ratio and voids are arranged in a roughly geometric fashion[14]. Originally, this process involved the introduction of reactive gases into the molten glass during processing; this required high temperatures and was therefore very energy intensive. Another technique, first developed in the 1940s, allows for foamed glass materials to be produced through cold isostatic pressing (CIP) processes and then consolidated at lower temperatures (T = ~0.55T_m) [24, 25, 29]. This method has gained popularity in recent years because of its lower energy requirements.

In CIP processes, the glass is first pulverized to less than 50 microns and then a foaming agent is added in powder form, after which the mixture is formed into molds at high pressure. Recent work has shown that waste glass is compatible with this process [30-32]. Bernardo et al.[32] showed that several types of waste glasses can be densified successfully through foaming processes; unfortunately, the feedstocks used were refined wastes and did not contain contaminants typical of municipal waste glass. The materials used in these investigations

exhibited bulk densities ranging from 0.22 to 0.42 g/cm^3 and were found to agree with Gibson and Ashby's models for the compressive strength of foams[14].

2.2.3. Sintered Waste Glass

Several researchers have also demonstrated that waste glass can be successfully incorporated into high-density glass ceramics [33-36]. Bernardo's experimental work focuses on the crystallization of industrial wastes through fast sintering at slightly higher temperatures than used during foaming processes (T = ~0.6T_m) and results in materials with porosities ranging from 2.8% to 22%. However, in this investigation the waste glass was first fully melted and then cooled and pulverized to the desired size. Again, this work uses raw materials with a rather narrow particle size distribution (<37 microns). Their results indicate transverse rupture strength as high as 130.7 MPa and elastic moduli as high as 89.3 GPa at 3% porosity. At 22% porosity, they report values for the transverse strength and elastic modulus of 59.1 MPa and 48.8 GPa respectively.

More recent research performed by Marchelli and Prabhakar in 2011 led to the development of a high recycle content, glass composite that was intended for use in the manufacture of commercial and residential building products[2, 3]. Prabhakar and Marchelli's work was motivated by the desire to reduce production energy requirements and provide a means for capturing and reusing glass fines. The core technology was the formation of a high recycle content, glass composite precursor that could be plastically deformed in the cold state.

Historically, the brittle nature of glass has prevented the use of cold processes that typically rely on the use of pressure to consolidate powdered materials. In contrast to metals, which are often processed through CIP, glass does not undergo plastic deformation when subjected to pressures in excess of the yield strength. Instead, glass particles are further

pulverized and consolidation does not take place. With respect to the large-scale production of building materials, cold working is advantageous for two main reasons. First, the energy requirement for processing are greatly reduced. Second, given the large volume of units produced, unless materials can be consolidated to near net shape and demolded prior to densification, the overall cost of manufacturing would be prohibitive, as each unit would then need to be densified within its own mold. Moreover, the nature of the proprietary binding agents used in this process resulted in a precursor with a glass content of >95%, which enabled Prabhakar and Marchelli to densify materials at temperatures just over the glass transition temperature. The high glass to binder ratio maximizes the contact surface area of the glass particles, which accelerates the sintering phenomenon at low temperature. This provides further benefit in terms of energy usage and associated cost.

Additional research with respect to the physical and mechanical properties of EnVitrum's materials was presented by Prabhakar in 2012[4]. The main objectives of this work were to i) evaluate the effects of temperature on the bulk properties of the material and ii) characterize the relationship between porosity and mechanical properties. Specimens in the ~7-35% apparent porosity range were produced and tested. The mechanical test data were evaluated using the Weibull approach, which is common in the study of fracture mechanics of brittle media. The experimentally obtained data was also compared to established correlations that describe the relationship between porosity and mechanical properties presented in Section 2.3.

Prabhakar concluded that EnVitrum's process for creating macro-scale porous materials, from recycled glass resulted in predictable physical and mechanical behavior. In addition, the results supported the conclusion that the densification process used was compatible with contaminated waste glass and that the presence of micro-scale organic and inorganic

contaminants did not prevent sintering. Moreover, it was found that through manipulation of peak densification temperature, sufficient strength could be achieved for construction applications.

2.3. Porosity-Property Relations

The manufacture and mechanical characterization of porous ceramics have been topics of interest since the 1950s. Since that time, advanced ceramic materials have been used in a wide range of applications, including sensors, insulators, heat exchangers, particulate filters, refractories, building materials and more recently, bone scaffolds. Researchers have proposed many models to characterize the behavior of materials in relation to their porosity or bulk density. These models can generally be divided into two main types: those that make the assumption of spherical particles and those that approximate the material as composed of two phases.

One of the earliest models using the first approach was proposed by Duckworth, in his 1953 commentary on Ryshkewitch's work, wherein he proposed an empirical, exponential relationship between porosity and compressive (Eq. 2.9) [37, 38]. Spriggs then extended Duckworth's work to the relationship between porosity and elastic modulus in 1961 (Eq. 2.14) [39]. This was predicated on Knudsen's[40] research, which also assumed that the solid phase of the material was composed of spherical particles. Duckworth's empirical model was subsequently refined by a number of researchers. In 1964, Brown, Biddulph and Wilcox built on this work and proposed a 2/3-power relationship based on their investigation on the effects of pore geometry and orientation (Eq. 2.15)[41]. Wang's 1984 semi-empirical work focused on the effects of open versus closed cell pores and he proposed modifying Spriggs' model to included higher order terms (Eq. 2.16) [42]. This was found to agree with experimental data at the lower

end of the porosity range (≤ 0.32) and led to Phani and Niyogi's power model, which was meant to account for pore interconnectivity (Eq. 2.17) [43]. The Phani-Niyogi model was later simplified by Wagh, Singh and Poeppel, whose model assumes random pore geometry and packing density (Eq. 2.18) [44].

In second approach the bulk material is assumed to have two phases: the continuous phase, which corresponds to the solid material, and the disperse phase, which corresponds to inclusions or voids. Some of the earliest work was presented by MacKenzie in 1950, where he proposed a quadratic relationship between porosity and the elastic modulus of porous ceramics (Eq. 2.19)[45]. This was largely empirical in nature and has been found to fit wide range of experimental data. The main drawback of all of the models discussed so far is that they fail to satisfy the boundary conditions (e.g. a calculation with porosity equal to one would not result in an elastic modulus value of zero).

In response to this, in 1960 Hashin proposed a rigorous, theoretical model using the two-phase approach (Eq. 2.20) [46]. This model is based on an evaluation of strain energy in a loaded homogeneous body due to the presence of discontinuities or inclusion. It makes use of a composite sphere approach, where the bulk material is modeled as a series of solid spheres, each containing a spherical inclusion. The size distribution of these composite spheres is assumed to be such that there are no voids between the particles. Recognizing that such a size distribution of composite spheres is unrealistic, Hasselman simplified Hashin's correlation through a semi-empirical approach that accounted for the voids between adjacent spheres (Eq. 2.21) in 1962[47].

Realizing that porosity alone did not account for variations in mechanical properties, researchers began to recognize the importance of pore geometry. In 1993, Ramakrishnan built on the composite sphere model (Eq. 2.22) [48]. His correlation was based on the effective Poisson's

ratio of two-phase materials. In the early, 1990s Nielsen proposed a theoretical model that was found to successfully predict behavior in a broad range of materials, including porous glasses. His work focused on the relationship between porosity and stiffness (Eq. 2.23)[49, 50] and the models were based on pore size, pore geometry, and pore interconnectivity. In addition, materials could be characterized by the coarseness of the porous structure.

Gibson and Ashby also proposed relationships between the strength, elasticity and porosity of cellular materials[14]. This work was based on the relative density of the two-phase material and was largely theoretical. The models were built upon the geometry of the walls, which in cellular materials can be quite tightly controlled. Their models for open and closed cell foams were found to successfully predict compressive strength in a wide range of materials including ceramics, plastics and metals (Equations 2.10-2.12). Gibson and Ashby are often cited by researchers investigating glass foams and foaming techniques [32, 51].

The equations are shown in Table 2-2. In Equations 2.9-2.12, σ represents the compressive strength, σ_o is the zero-porosity compressive strength, P is the porosity, and ρ_r is the relative density, while a, b and φ are fitting parameters. The parameter φ describes the degree to which cells are open or closed and can vary between zero and one. In Equations 2.13-2.22, E_o is the zero-porosity value of the elastic modulus, v_o is the zero porosity Poisson's ratio and a, b, c, f_1 and f_2 are fitting parameters. In Equations 2.20 and 2.22 the data is fit by manipulating Poisson's ratio. In Equation 2.17, a describes the complexity of the pore structure, P_D is the critical porosity and M describes variation in interaction of the pores. Nielsen's work has shown that the elastic modulus of porous glasses is successfully predicted when P_D and M are equal to unity.

Table 2-2. Published models for strength and elastic modulus as a function of porosity.

Porosity vs. Strength			
Duckworth[38]	$\sigma = \sigma_o e^{-aP}$		(2.9)
Gibson-Ashby: Open Cell[14]	$\sigma = \sigma_o a {\rho_r}^{3/2}$		(2.10)
Gibson-Ashby: Open, high density[14]	$\sigma = \sigma_o a {\rho_r}^{3/2}\left(1 + {\rho_r}^{1/2}\right)$		(2.11)
Gibson-Ashby: Closed Cell[14]	$\sigma = \sigma_o a(\varphi\rho_r)^{3/2} + b(1-\varphi)\rho_r$		(2.12)
Porosity vs. Elastic Modulus			
Single-Phase Models			
Spriggs[39]	$E = E_o e^{-bP}$	$P \leq 0.5$	(2.14)
Brown -Biddulph-Wilcox[41]	$E = E_o(1 - aP^{2/3})$		(2.15)
Wang[42]	$E = E_o e^{[-(bP+cP^2)]}$	P ≤ 0.32	(2.16)
Phani-Niyogi[43]	$E = E_o(1-aP)^n$		(2.17)
Wagh-Poeppel-Singh[44]	$E = E_o(1-P)^n$		(2.18)
Empirical Two-Phase Models			
MacKenzie[45]	$E = E_o(1 - f_1 P + f_2 P^2)$		(2.19)
Hashin[46]	$E = E_o\left(\frac{1-P}{1+kP}\right)$ $k = \frac{(1+v_o)(13-15v_o)}{2(7-5v_o)}$		(2.20)
Hasselman[47]	$E = E_o\left[1 - \frac{aP}{1+(a-1)P}\right]$		(2.21)
Ramakrishnan[48]	$E = E_o\frac{(1-P)^2}{1+k_E P}$ $k_E = 2 - 3v_o$		(2.22)
Nielson[49, 50]	$E = E_o\left(\frac{1-P}{1+P/\mu}\right)$ $\mu = a(1-P/P_d)^M$		(2.23)

2.4. SUMMARY

Many investigations have explored the addition of waste glass into the virgin raw material stream. This work has been largely unsuccessful and currently, the energy and cost associated with incorporating waste stream materials outweighs any advantage. More promising research has been centered on incorporating waste glass into foaming and sintering processes. Both the foaming and fast sintering work has resulted in significant reductions in energy expenditures.

Marchelli and Prabhakar's process poses three significant advantages. First, the process temperatures used were ~15-30% lower than those used in prior investigations and the preliminary melting step was omitted entirely[2, 3]. This reduces the energy requirements of the process significantly. Second, their process can utilize raw materials with a broader particle size distribution. This may mean that less energy will be required to pre-process feedstocks. Third, their work was the first to utilize contaminated waste glass in a process that does not result in crystallization. This is compelling as crystallized materials have little utility in the built environment. Their density, stiffness and low strength to weight ratio make them appropriate only for a very narrow range of applications.

Although these initial findings were quite positive, industry adoption of this process will require further research. Prabhakar made several important points in her conclusions and recommendations for future work[4] as summarized below.

1. The mechanical testing data collected during Prabhakar's 2012 research were not well behaved. Although the data show predictable results with respect to densification temperature and its effect on volumetric strain, bulk density, and apparent porosity, the material did not exhibit stress-strain behavior consistent with brittle solids or cellular

porous material, particularly under compressive loading. In addition, calculated values for the elastic modulus obtained through compressive and flexural testing did not agree. At the conclusion of those studies, it was unclear if discrepancies were the consequence of inconsistencies in processing, irregular specimen geometry or inherent characteristics of the material.

2. Although established theoretical models have been shown to fit the experimental well. The accuracy of the models has not been evaluated for materials that exhibit <7% apparent porosity. Testing of additional specimens with lower porosity might aid in this evaluation.

3. The research would benefit from the characterization of the mechanical behavior through 4-point bending tests, rather than 3-point. In the 4-point bend test, the shear force between the two loading pins is zero and bending stresses are uniform over the entire area between the two loads. Because the area over which bending stresses are applied is larger, the probability of encountering a defect is larger as well. Hence, the 4-point method yields more realistic values of transverse rupture strength.

4. Analysis of the data using the 3-parameter Weibull distribution might provide more reliable information regarding the probability of failure in components, as this method provides more robust results.

5. The effects of specimen size on mechanical properties should be undertaken. It is widely recognized that the transverse strength of porous materials does not remain constant with changes in specimen size.

6. Investigation of the effects of varying contamination will be necessary. Very little work has been performed with contaminated waste glass. Successfully using waste glass as a primary

feedstock will require a comprehensive understanding of how contaminants in the supply will affect the microstructure and mechanical properties.

7. Processing via extrusion would be very helpful to commercialization. Although CIP methods are utilized by industry, the majority of masonry manufacturers have moved towards extrusion. CIP and extrusion have many aspects in common and this transition has been made with numerous masonry products. However, this material will present unique challenges due to the brittle nature of glass.

To summarize the empirical and theoretical investigations into the mechanical properties of porous materials, which were presented in Section 2.3, it is clear that these studies have resulted in a wide variety of models. Generally, these models are based on the assumption that the solid phase of the material can be approximated by spherical particles or that the material can be modeled as cellular. It is unclear how accurately these models will predict the behavior in a non-homogenous material.

CHAPTER 3. RESEARCH SCOPE AND OBJECTIVES

The research proposed herein is motivated by a desire to provide the construction industry an energy efficient and cost effective recycled material that exhibits predictable and repeatable physical and mechanical performance, while simultaneously providing the recycling industry an outlet for their low value glass fines. In addition, because of the very high glass content of the material under investigation, the usefulness of this research extends beyond Marchelli and Prabhakar's material and will contribute more broadly to the understanding of porous ceramics.

Many types of porous brittle materials, such as brick, concrete and tile, are used commonly in the construction industry. Brick and similar masonry products are generally used in applications where design loads are compressive in nature. However, in several of these applications, materials are also expected to withstand transverse loading. The requirements for compressive and flexural strength in structural ceramics are established by American Society for Testing and Materials (ASTM). This section presents the scope and objectives of the proposed work.

3.1 RESEARCH SCOPE

As discussed in the previous chapter, a number of research issues were outlined. These were directed at furthering the industry adoption Marchelli and Prabhakar's process and contributing to the scientific understanding of the physical and mechanical behavior of materials that utilize powder processing techniques in their manufacture[4]. In prioritizing the recommendations, it became clear that before any addition tasks could be undertaken, the process itself would have to be scrutinized, as many of the inconsistencies present in the data may be attributable to imprecise specimen processing and irregular specimen geometry.

3.2 Research Objectives

The research performed subsequently and outlined in this document endeavors to address these questions. Successful completion of this work may provide the manufacturing and construction industries with sustainable alternatives to standard products, while also providing a commercial outlet for the large quantities of waste stream glass that cannot currently be recycled. Further, this work will contribute to the scientific understanding of porous materials, particularly with respect to contaminated waste glass. The objectives of this research are as follows:

1. Process Development: Investigate potential processing problems that may have led to geometric or microstructural irregularities during specimen formation and subsequent scattering of mechanical testing data[4].
    a. Investigate potential issues with specimen formation via hydraulic press:
        i. In the previous studies, the applied force was measured directly from the press, which measures applied load based on the hydraulic pressure developed when the piston is extended into the hydraulic chamber by means of a pump. Given the range and resolution of the machine, as well as the indirect nature of the measurement, it was suspected that inconsistencies in applied press force may have contributed to irregularities in the data.
        ii. All specimens were formed using 1 ton of force (~8900 N). This was done in an effort to simulate the process used in the industrial production of clay brick and comparable masonry products. However, forming both the square and rectangular specimens using the same force would result in

different applied hydrostatic pressure. This, in turn, would mean that the results of compressive and flexural testing could not be directly compared.

iii. The effects of formation pressure on the mechanical properties of the material were not investigated. It is well known that the applied pressure during formation has a strong effect on the packing density of the particles. This in turn effects the sintering phenomena and subsequently, the physical and mechanical properties.

b. Investigate the role that geometric distortion of the specimens may have played on stress-strain behavior: Dimensional distortion was observed after densification, particularly with respect to specimens fired at higher temperatures. It was thought that these distortions gave rise to inconsistent behavior during mechanical testing. In the masonry industry, this issue is overcome by "capping" each specimen with mortar, in order to fill concavities and create a flat loading surface. Due to the small size of the specimens being tested here, the capping method would not be feasible.

2. Evaluate potential errors due to machine compliance: All strain data analyzed during the prior study was calculated based on crosshead displacement and not collected through direct measurement via strain gages or extensometers located on the specimens[4]. These calculations did not account for possible deformation of the loading system itself. This may have led to inaccurate observations of stress-strain behavior and subsequently errors in estimation of the elastic modulus.

3. Characterize the mechanical behavior with respect to peak densification temperature: Once the process development tasks were complete, specimens were formed using

constant formation pressure while the peak densification temperature is varied for separate batches. The collected data was used to investigate how the peak densification temperature effects the mechanical behavior of the material under compressive and transverse loading.

4. Theoretical modeling:

    a. Once mechanical testing was completed the data was analyzed via the 2-parameter Weibull distribution. The results from compressive and flexural testing will be compared. In addition, the effects of process development improvements will be evaluated.

    b. The experimental data describing the mechanical behavior will be compared to zero porosity values and subsequently the suitability of established porosity-property correlations will be evaluated.

5. Fractography: Once mechanical testing was complete, the general fracture behavior of specimens densified at different peak temperatures was characterized.

CHAPTER 4. EXPERIMENTAL METHODS & PROCEDURES

4.1 PROCESS DEVELOPMENT

4.1.1. MATERIALS

The materials used in this research were collected from the municipal waste stream in the greater Seattle area. The composition of collected glass can vary significantly. After collection, it was processed by TriVitro® into a product called VG105, which contains irregularly shaped particles of differing size and color, as well as both organic and inorganic contaminants. This product is generally sold as a sandblasting medium and is screened to the appropriate size for that particular application. Independent particle size analysis was performed prior to experimentation and data was obtained via sieve analysis. The results of the analysis are shown in Figure 4-1.

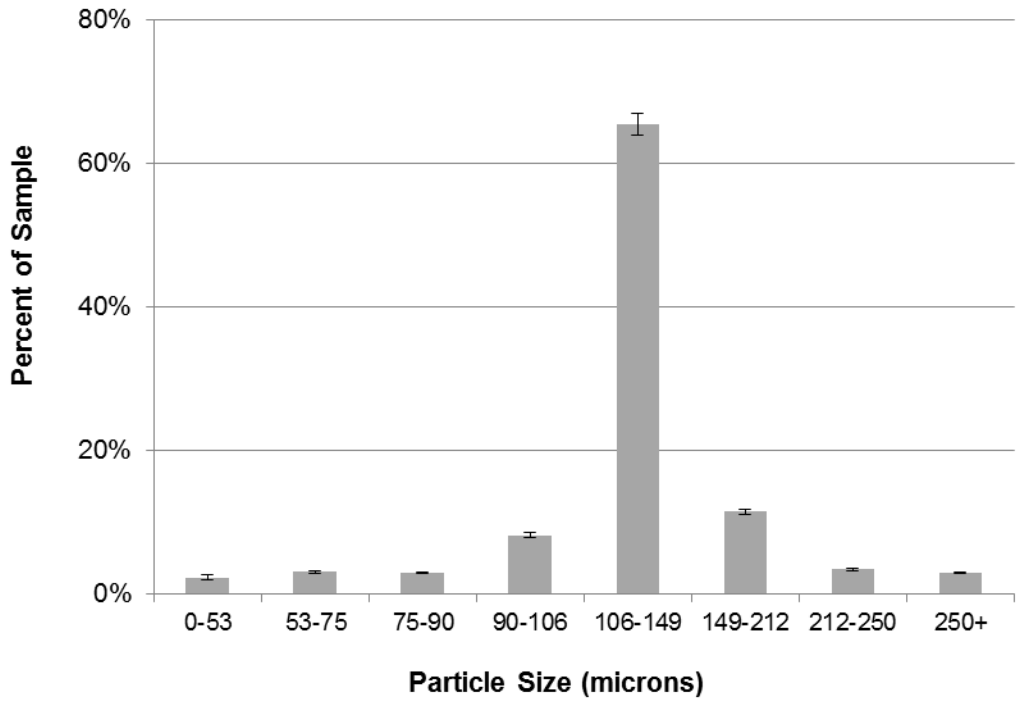

Figure 4-1. Particle size distribution of waste glass feedstock. Results were obtained through sieve analysis.

The particle size distribution exhibits Gaussian behavior, with particles being concentrated in the 106-149 micron range. The as-received glass was not processed in any way prior to experimentation. It was not further screened or sorted for color and contamination was not removed.

4.1.2. Green Compact Formation & Densification

Specimens composed of soda-lime silicate waste glass were formed using the method described by Marchelli and Prabhakar; green compacts were formed in the cold state using a CIP method[2]. Materials were formed in aluminum molds and hydrostatic pressure was slowly applied by means of a Wabash 30-1515-2TMB four-post hydraulic press with an operating range of 0 to 30 tons (0-266.9 kN).

Prismatic specimens with two specific geometries were formed in batches of 20. The first type of specimen was to be used in subsequent compressive testing and these specimens were formed to nominal green dimensions of 1.25” x 1.25” x 0.5” (31.75mm x 31.75mm x 12.7mm). The second type of specimen was to be used in subsequent flexural testing and these specimens were formed to nominal green dimensions of 1.75” x 0.75” x 0.5” (44.45mm x 19.05mm x 12.7mm). Formation parameters and testing types can be seen in Table 4-1.

Table 4-1. Test matrix describing specimen processing and testing.

	# of Specimens	Feedstock	Specimen Formation and Preparation															Data Collected				
			Formation Pressure (MPa)							Polished	Peak Densification Temperature (∘C)							Volumetric Strain	Bulk Density	Apparent Porosity	Compressive Testing	Flexural Testing (3-pt Bend)
			5.2	6.8	8.8	17.3	25.5	34.5	43.1		704.4	718.3	732.2	746.1	760.0	773.9	787.8					
Formation Pressure Evaluation	20	VG105	x							No				x				x	x	x	x	
	20	VG105		x						No				x				x	x	x	x	
	20	VG105			x					No				x				x	x	x	x	
	20	VG105				x				No				x				x	x	x	x	
	20	VG105					x			No				x				x	x	x	x	
	20	VG105						x		No				x				x	x	x	x	
	20	VG105							x	No				x				x	x	x	x	
	20	VG105	x							No				x				x	x	x		x
	20	VG105		x						No				x				x	x	x		x
	20	VG105			x					No				x				x	x	x		x
	20	VG105				x				No				x				x	x	x		x
	20	VG105					x			No				x				x	x	x		x
	20	VG105						x		No				x				x	x	x		x
	20	VG105							x	No				x				x	x	x		x
Geometric Distortion and Peak Densification Temperature Evaluations	20	VG105				x				No	x							x	x	x	x	
	20	VG105				x				No		x						x	x	x	x	
	20	VG105				x				No			x					x	x	x	x	
	20	VG105				x				No				x				x	x	x	x	
	20	VG105				x				No					x			x	x	x	x	
	20	VG105				x				No						x		x	x	x	x	
	20	VG105				x				No							x	x	x	x	x	
	20	VG105				x				No	x							x	x	x		x
	20	VG105				x				No		x						x	x	x		x
	20	VG105				x				No			x					x	x	x		x
	20	VG105				x				No				x				x	x	x		x
	20	VG105				x				No					x			x	x	x		x
	20	VG105				x				No						x		x	x	x		x
	20	VG105				x				No							x	x	x	x		x
	20	VG105				x				Yes	x							x	x	x	x	
	20	VG105				x				Yes		x						x	x	x	x	
	20	VG105				x				Yes			x					x	x	x	x	
	20	VG105				x				Yes				x				x	x	x	x	
	20	VG105				x				Yes					x			x	x	x	x	
	20	VG105				x				Yes						x		x	x	x	x	
	20	VG105				x				Yes							x	x	x	x	x	
	20	VG105				x				Yes	x							x	x	x		x
	20	VG105				x				Yes		x						x	x	x		x
	20	VG105				x				Yes			x					x	x	x		x
	20	VG105				x				Yes				x				x	x	x		x
	20	VG105				x				Yes					x			x	x	x		x
	20	VG105				x				Yes						x		x	x	x		x
	20	VG105				x				Yes							x	x	x	x		x
	840	Total Specimens																				

4.1.3. EXPERIMENTAL METHODOLOGY

In completing the research discussed herein, a Futek FTH500 load cell with an operating range of 0 to 20,000 lbs. (0-88.96 kN) and readability & non-linearity of ±0.5% of rated output was employed. The load cell was placed between the lower press platen and the frame (Figure 4-2), directly in line with the applied force. Data was acquired through a National Instruments 9219 Data Acquisition module and collected via LabVIEW.

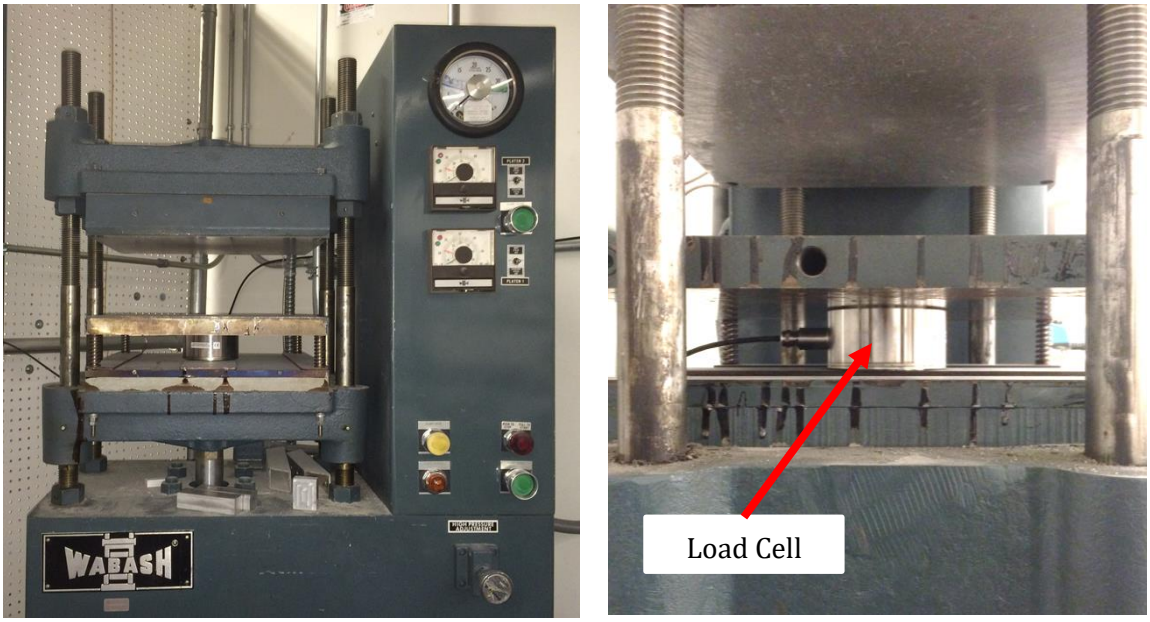

Figure 4-2. Location of load cell installation on Wabash hydraulic press.

Specimens were formed using an applied force that would result in equivalent hydrostatic pressure for both specimen geometries. Once formed, the green compacts were removed from the molds and allowed to dry under ambient conditions for 48 hours. The specimens were then kiln-dried for 24 hours at ~120°C in order to ensure the removal of any residual moisture. This was evaluated through mass loss data and visual evaluation of an "indicating desiccant" that marks the presence of moisture via color change.

At this time the green dimensions were recorded; width and length were measured using 6-inch Mitutoyo Absolute Digimatic calipers (Model 500-171) with accuracy of +/- 0.001inches

(+/- 0.0254 mm). Thickness was measured using a Mitutoyo 570 Series height gage with accuracy of +/-0.002 inches (+/- 0.0508 mm) in combination with a AA laboratory grade precision granite surface plate with +/- .000025" overall accuracy. Two measurements were recorded for the length, two for the width and three for the thickness of each specimen. Specimens were then fired on one inch (2.54 mm) thick vermiculite in a Cress C181822-DWH electric furnace with chamber dimensions of 18”H x 18”W x 22”D (0.457m x 0.457m x 0.559m) and chamber uniformity of +/- 25°F (+/- 14°C). Vermiculite is a low-density material often used in the densification of ceramics. Because of its low thermal mass, specimens that are fired on vermiculite rather than directly on the firebrick or on alumina kiln furniture, experience more uniform heat transfer and deformation during densification is minimized.

In all cases, once the densification process was complete, dimensional measurements of each specimen were recorded using the procedure described above for the green state specimens. These data were then used to calculate the mean and standard deviation of volumetric strain for each batch. The apparent porosity and bulk density were calculated using the Archimedes’ test method[52]. All data used in calculations based on the Archimedes’ method were taken using an Ohaus Adventurer laboratory scale with +/- 0.001g readability. Once the specimens were fired, their dry mass (*D*) was recorded. The specimens were then boiled in distilled water at 100°C for 5 hours and allowed to soak at ambient temperature for an additional 24 hours following the boil. Each specimen was then suspended in a bath of distilled water using the Archimedes’ test apparatus and the suspended mass (*S*) was recorded. Finally, once the saturated mass (*M*) of each specimen was recorded, the apparent porosity and bulk density of each specimen was calculated using Equations 3.2-3.8. In these equations, V is the exterior volume, V_{OP} is the volume of the open pores, V_{IP} is the volume of the impervious portions, P is the apparent porosity (in percent),

A is the water absorption (in percent), *T* is the apparent specific gravity and *B* is the bulk density (in g/cm^3). During these calculations, the assumption is made that the density of water at room temperature is 1 g/cm^3 as specified by ASTM [52].

$$V = M - S \tag{3.2}$$

$$V_{OP} = M - D \tag{3.3}$$

$$V_{IP} = D - S \tag{3.4}$$

$$P = 100\left[\frac{(M-D)}{V}\right] \tag{3.5}$$

$$A = 100\left[\frac{(M-D)}{D}\right] \tag{3.6}$$

$$T = \frac{D}{D-S} \tag{3.7}$$

$$B = \frac{D}{V} \tag{3.8}$$

As "capping" of these small specimens would not be feasible, prior to collection of mechanical test data, the loading surfaces of all specimens were polished flat and parallel in accordance with ASTM E9[53]. This was performed via a mechanical polisher equipped with 80 grit silicon carbide discs and verified using the metrology equipment and procedures outlined above.

4.2. Mechanical Property Evaluation

4.2.1. Specimen Geometry

The images in Figure 4-3 are representative of two batches of compression specimens following densification. The specimen in Figure 4-3a through 4-3c was fired at a peak temperature of 1300°F (~705°C), while the specimen in Figure 4-3d through 4-3f was fired at 1450°F (~790°C).

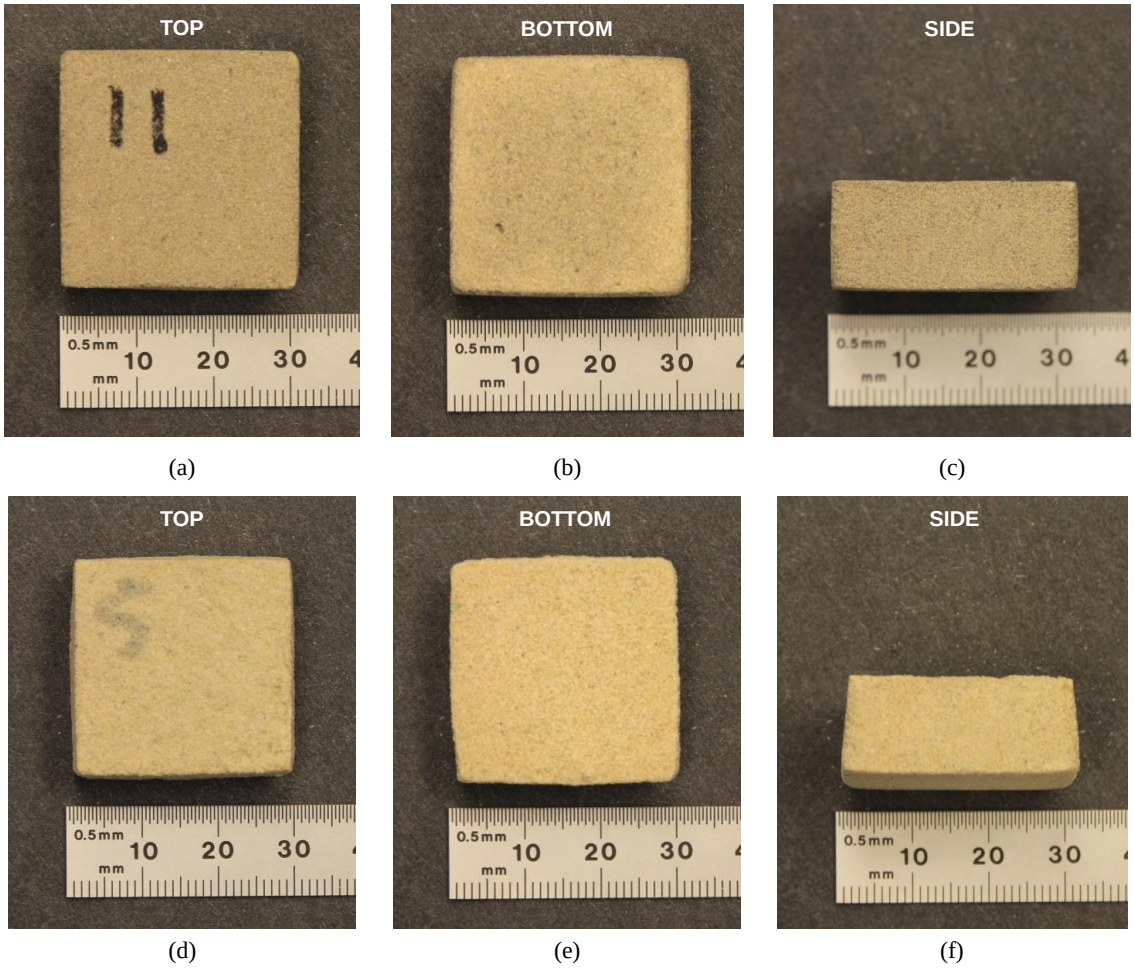

Figure 4-3. Compression specimen after densification. (a-c) Fired at peak temperature of 1300°F (~705°C). (d-f) Fired at peak temperature of 1450°F (~790°C).

Visual inspection of the two specimens indicates that the specimen fired at 705°C appears to have undergone negligible dimensional distortion. The edges and face remained relatively planar and square after densification. A similar inspection of the specimen fired at 790°C shows considerable dimensional distortion along all three axes. From the side view the specimen appears trapezoidal.

The images in Figures 4-4 are representative of two batches of flexure specimens following densification. The specimen in Figure 4-4a through 4-4c was fired at a peak temperature of 1300°F (~705°C), while the specimen in Figure 4-4d through 4-4f was fired at 1450°F (~790°C).

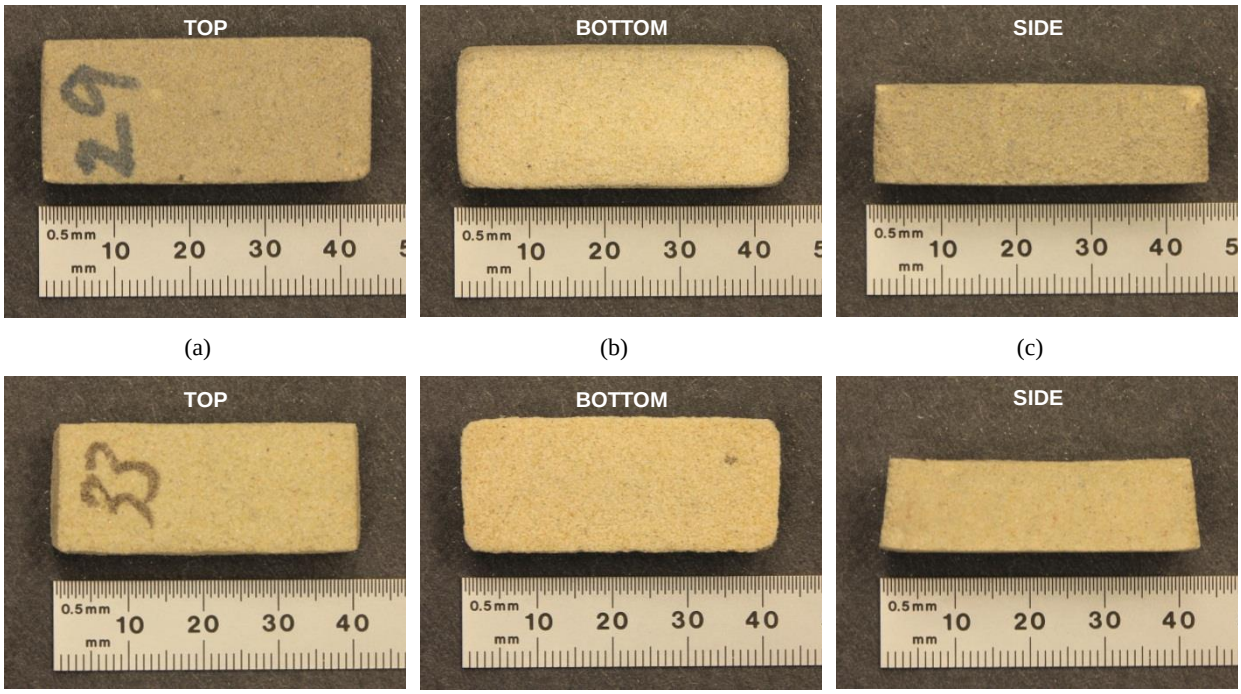

Figure 4-4. Flexure specimen after densification. (a-c) Fired at peak temperature of 1300°F (~705°C). (d-f) Fired at peak temperature of 1450°F (~790°C).

Visual comparison of the two specimens follows the same pattern as was observed for the compression specimens. As the peak densification temperature is increased, specimens undergo a higher degree of dimensional distortion. This seems to be more pronounced in the flexure specimens.

Preliminary SEM micrographs of the exterior surfaces of two representative specimens are shown in Figure 4-5, where it can be seen that surface irregularities and imperfections are much more pronounced in high porosity specimens.

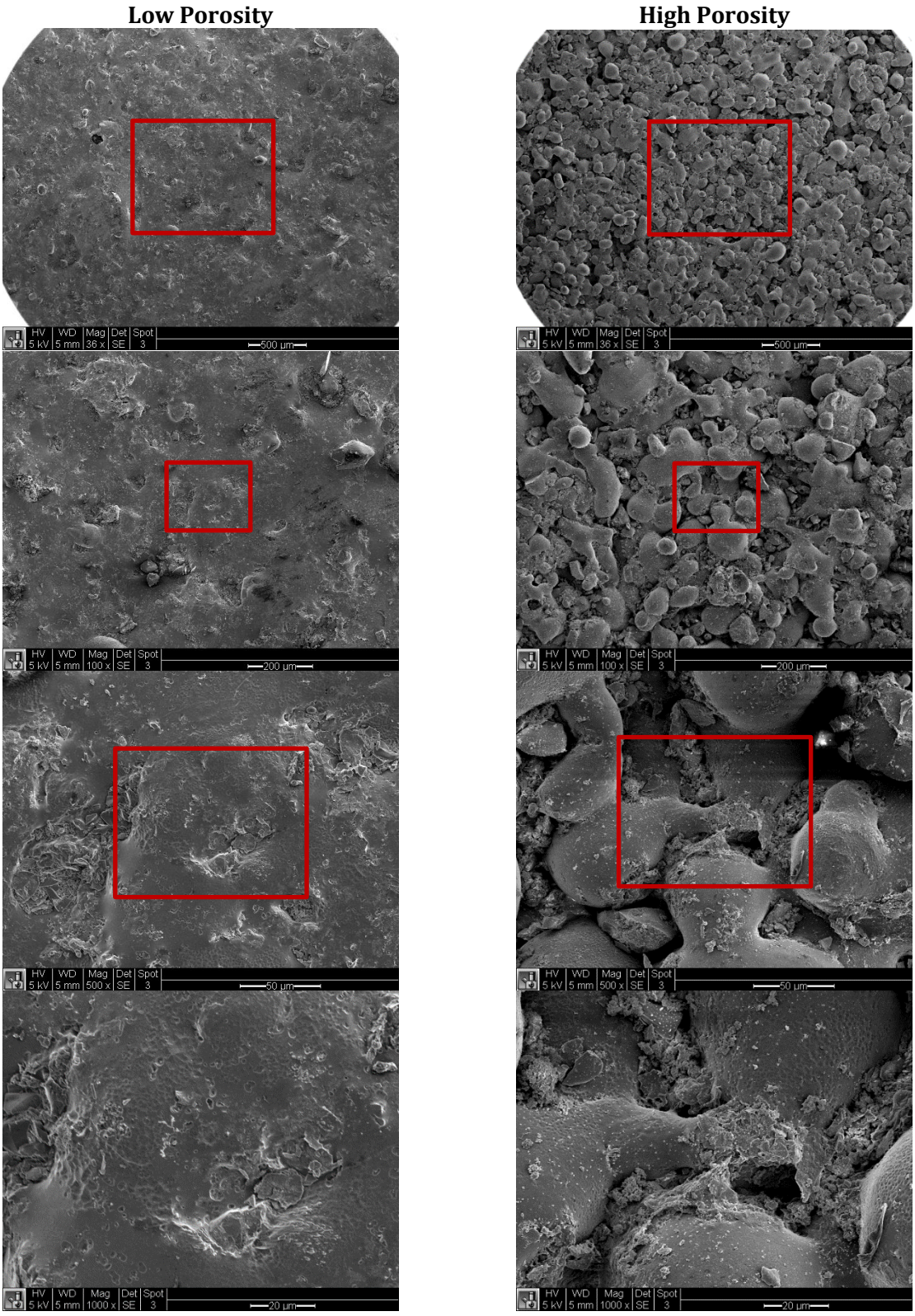

Figure 4-5. SEM micrographs of exterior surfaces of characteristic compression specimens.

Optical micrographs of a characteristic polished specimen are shown in Figure 4-6, where it can be seen that distortion of the loading surfaces is negligible after polishing. Although some dimensional variation in the 4 sides of the specimens still exists, distortion of the loading surfaces has been minimized.

Top Bottom Side

Figure 4-6. Characteristic compression specimen after polishing.

4.2.2 Mechanical Testing & Analysis Procedures

4.2.2.1. Compression Test System: Compressive testing took place using an INSTRON 5585H series floor model load frame equipped with a 250 kN load cell. To the extent that was possible, compressive testing took place in accordance with ASTM testing standards for structural ceramics [54]. Specimens were placed on a spherically seated bottom bearing surface, which was free to rotate in the longitudinal and transverse directions as shown in Figure 4-7.

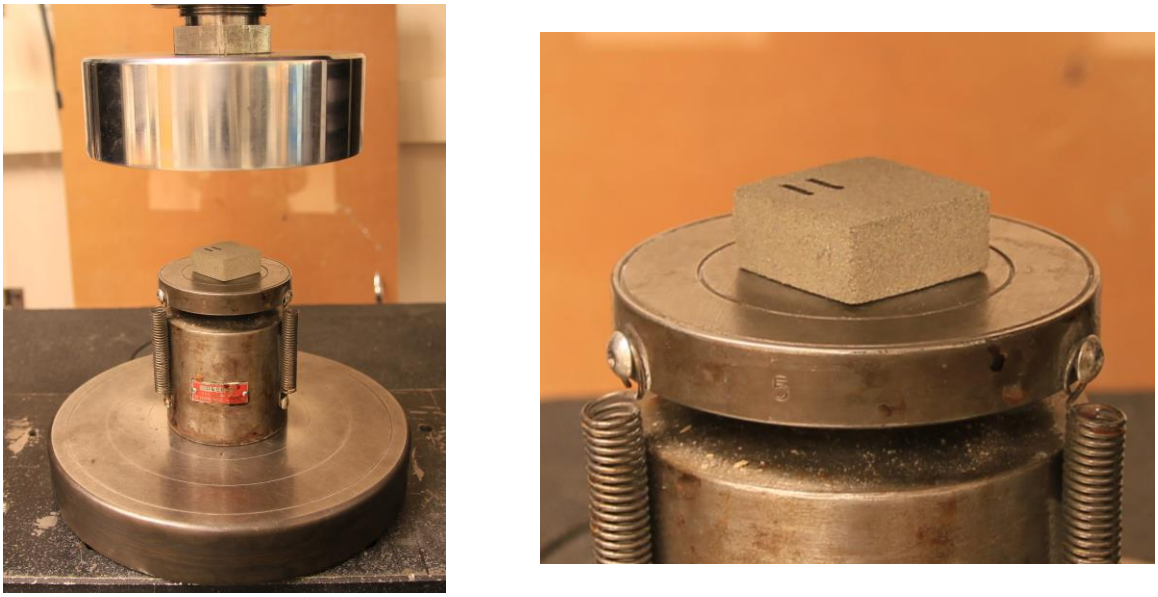

Figure 4-7. INSTRON 5585H outfitted with spherically seated bottom bearing plate.

Once the specimen was centered upon the bottom bearing surface, a preload of one pound was applied. During testing, the load was applied in two stages as per ASTM [54]. During the first stage, testing was performed at a speed of 0.1 in/min (2.54 mm/min) until an applied load of one half the expected maximum value was reached. During the second stage, the speed of testing was reduced by 50% (1.27 mm/min). Experimental data, including engineering stress, engineering strain, maximum compressive load and maximum compressive stress, were acquired through the Bluehill2 software package.

4.2.2.2. Flexure Test System: Flexural testing took place using the INSTRON 5585H as before. To the extent that was possible, testing took place in accordance with ASTM testing standards for structural ceramics, which is published in English units[54, 55]. The 3-point bending test fixture is shown in Figure 4-8, with and without a specimen loaded. The rate of testing was held constant throughout all batches tested at an extension speed of 0.05 inches per minute (1.27 mm/min) per ASTM[54]. Experimental data, including engineering stress, engineering strain,

maximum transverse load and transverse stress, were acquired through the Bluehill software package.

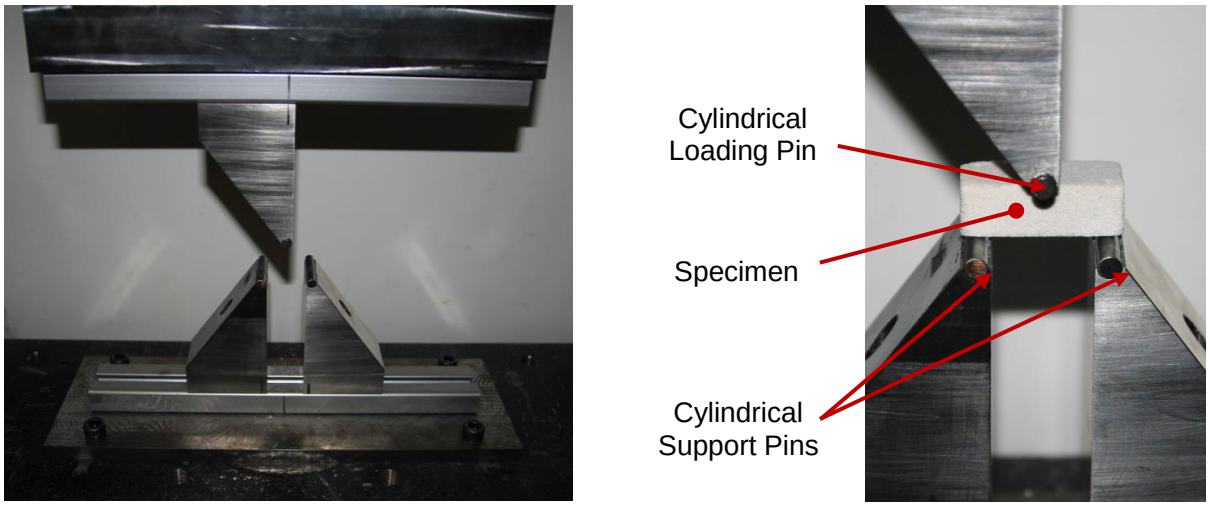

(a) (b)

Figure 4-8. Experimental setup for 3-point bending test. (a) Test fixture (b) Flexure specimen positioned in fixture.

4.2.2.3 Machine Compliance Correction: When specimens are tested using a universal load frame, the applied force is not simply applied to the specimen, but to the entire loading system. Therefore, deflection measurements taken at the crosshead are affected by not only the deflection experienced by the specimen, but also the deflection of the loading system as well. This well-known phenomenon can be described by Equation 4.1[56], where the apparent deflection (δ_A) is the raw deflection recorded by the software, the machine deflection (δ_M) is the deflection experienced by the loading system and the actual deflection (δ_S) is the deflection experienced by the specimen itself. Because the load applied to the system and the specimen is equivalent, this equation can be expressed in terms of compliance, as in Equation 4.2[56], where P is the applied load.

$$\delta_A = \delta_M + \delta_S \tag{4.1}$$

$$\frac{\delta_A}{P} = \frac{\delta_M}{P} + \frac{\delta_S}{P} \tag{4.2}$$

In order to determine the machine compliance, a specimen with well-known properties, typically a metal, is tested and the theoretical compliance is subtracted from the apparent compliance. Under uniaxial loading, cylindrical specimens are generally used and the compliance of the metal specimen is given by Equation 4.3[21, 22], where *L* is the length of the specimen, *E* is its elastic modulus and *A* is the area of the loading surface. Substituting this in to Equation 4.2 and rearranging to solve for the machine compliance yields Equation 4.4. Similar calculations based on the 3-point bending equations (Section 2.1.3) yield Equations 4.5[21, 22] & 4.6, where *t* is the specimen width and *c* is half of the specimen thickness. Once the machine compliance is calculated, it can be used to perform subsequent corrections to the crosshead displacement data collected from the universal load frame.

Uniaxial Testing

$$\frac{\delta_S}{P} = \left(\frac{L}{EA}\right)_S \tag{4.3}$$

$$\frac{\delta_M}{P} = \frac{\delta_A}{P} - \left(\frac{L}{EA}\right)_S \tag{4.4}$$

3-Point Bending

$$\frac{\delta_S}{P} = \frac{L^3}{4Et(2c)^3} \tag{4.5}$$

$$\frac{\delta_M}{P} = \frac{\delta_A}{P} - \left(\frac{L^3}{4Et(2c)^3}\right)_S \tag{4.6}$$

During this investigation, commercially available, precision ground, aluminum 6061-T6511 specimens were used to calculate the machine compliance. Under compressive loading, a cylindrical specimen was used with diameter of 2.000” +/- 0.024”, length of 0.5000” +/- 0.002”,

and a flatness tolerance of 0.010". Under transverse loading, a bar shaped specimen was used, with dimensions of 1.6" L x 0.7" W x 0.5" T and dimensional tolerances of +/- 0.0135. All calculations were carried out in MATLAB and the code can be seen Appendix B.

4.2.2.4. Mechanical Testing Data Analysis Procedure: After mechanical testing was complete and the machine compliance correction was performed, the stress-strain data was truncated to remove non-linear portions of the curve that occurred both during initial loading and after failure. Once the data was truncated to include only the linear portion of each stress-strain curve, Equation 2.8 was then used to calculate the modulus of elasticity. These calculations were performed in MATLAB and the code is shown in Appendix B.

Batch data was analyzed through the Weibull approach, which has been used widely in the field of fracture, particularly in brittle materials[57, 58]. The theory behind this model is that the specimen will fail when its weakest element fails and it is the preferred method for analyzing strength and fatigue data in ceramics and other brittle materials. This approach was used in analyzing both the strength and elasticity data. While analysis of the elastic modulus data via the Weibull distribution may not be worthwhile for homogeneous, isotropic materials, because the size and location of pores is unknown and randomly distributed, the weakest link model may apply in this case.

In analyzing the data through the Weibull approach, a probability plot was first constructed for each batch of data. This provides three important pieces of information. First, if the data can be fit reasonably well with a linear equation, this justifies the use of the two parameter Weibull distribution. Second, the slope of the line describes the degree of variability in the data set and is termed the shape factor or Weibull modulus. Third, the Weibull characteristic strength or scale factor is defined as the strength at which the probability of failure is 63.2%.

Using this information, the Weibull probability density function, cumulative distribution function, mean and standard deviation can be calculated. The Weibull probability density function (PDF) is given by Equation 4.9, where *a* is defined as the scale parameter and *b* is defined as the shape parameter. The Weibull cumulative distribution function (CDF) is given by Equation 4.10, which can be derived through integration of the PDF. The Weibull mean and standard deviation are given by Equations 4.11 and 4.12 respectively. All Weibull calculations were performed in MATLAB and the code is shown in Appendix B.

$$f(x|a,b) = \frac{b}{a}\left(\frac{x}{a}\right)^{b-1} e^{-(x/a)^b} \tag{4.9}$$

$$F(x|a,b) = 1 - e^{-(x/a)^b} \tag{4.10}$$

$$\mu = a[\Gamma(1 + b^{-1})] \tag{4.11}$$

$$\sigma = \sqrt{a^2[\Gamma(1 + 2b^{-1}) - \Gamma(1 + b^{-1})]^2} \tag{4.12}$$

CHAPTER 5. RESULTS

Data from all completed testing will be presented in this Chapter. Section 5.1 will focus on the results of the evaluation of formation pressure analyses. Section 5.2 will focus on the results from the evaluation of the effects of geometric distortion on stress-strain behavior. Section 5.3 will focus on the results from the evaluation of the effects of machine compliance. The results from compressive and flexural testing of specimens densified at varying peak temperature will be presented in Sections 5.4. Finally, established models for predicting mechanical properties based on porosity will be compared in Section 5.5.

5.1 FORMATION PRESSURE EVALUATION

5.1.1. PRESS FORCE DATA

Once the hydraulic press was outfitted with the load cell and data acquisition equipment, press force data was collected for each specimen during formation. Force was applied for ~20 seconds and the LabVIEW program was written to collect applied force data at 0.1 second intervals. In Figure 5-1, characteristic data can be seen for square specimens formed at applied loads of 0.5, 0.75 and 1 tons.

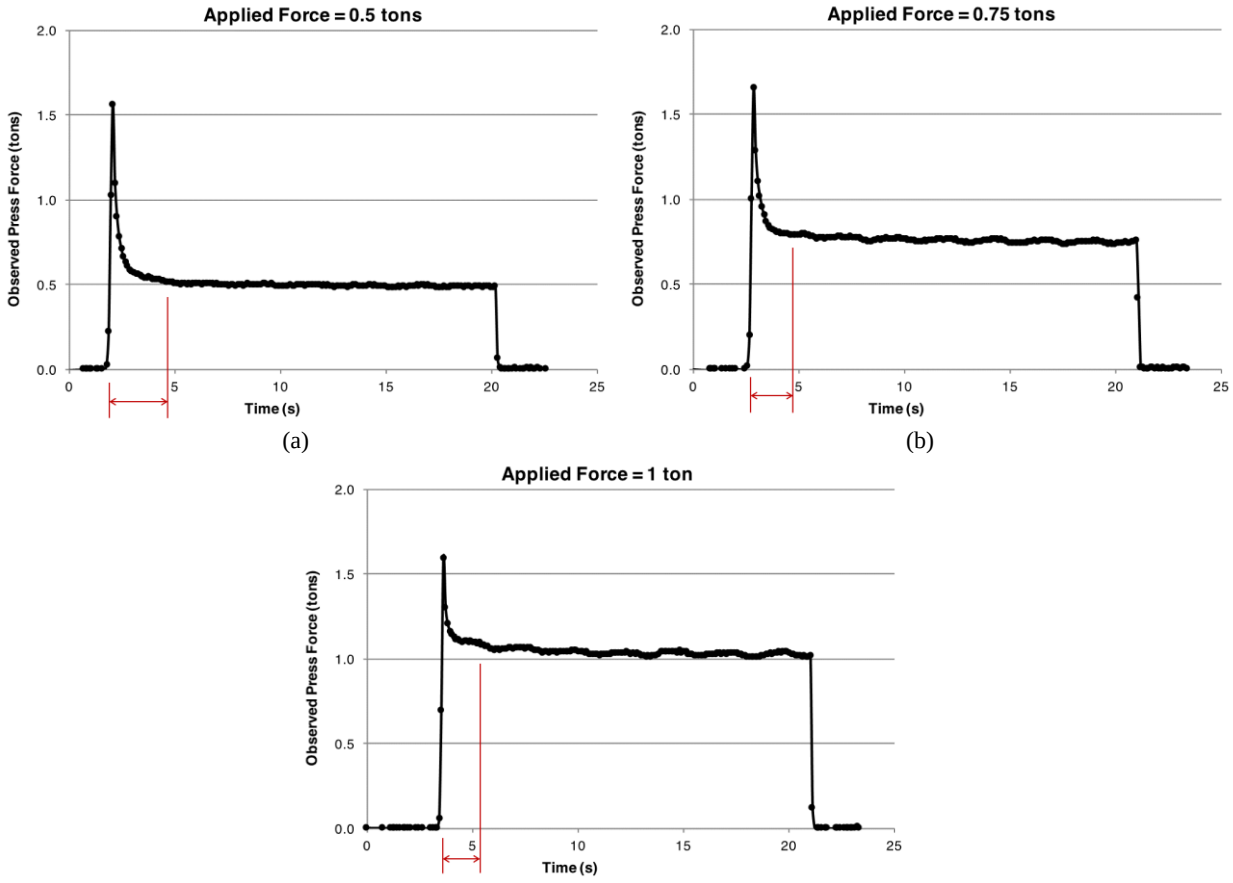

Figure 5-1. Press force versus time data collected for batches formed at applied force of (a) 0.5 tons, (b) 0.75 tons and (c) 1 ton.

Through this initial collection of applied force data, an important observation was made. From the figures above it appears that, although in all three cases the load does settle at the desired nominal force, in each case specimens experience an initial spike of ~1.6 tons before that occurs. This spike in pressure is common of hydraulic devices, particularly when operated in the lowest point of the equipment's operational range. The response time of the pump in that range is not adequate to prevent pressure buildup after the pump is stopped. In Figure 5-1, it can be seen that as the load is increased, the time to stability decreases (shown in red).

In order to ensure that subsequent experimental data was not affected by the observed spike, all subsequent specimens were formed at applied force of 1.75 tons or higher. Similar data for loads of 2, 3, 4, and 5 tons can be seen in Figure 5-2.

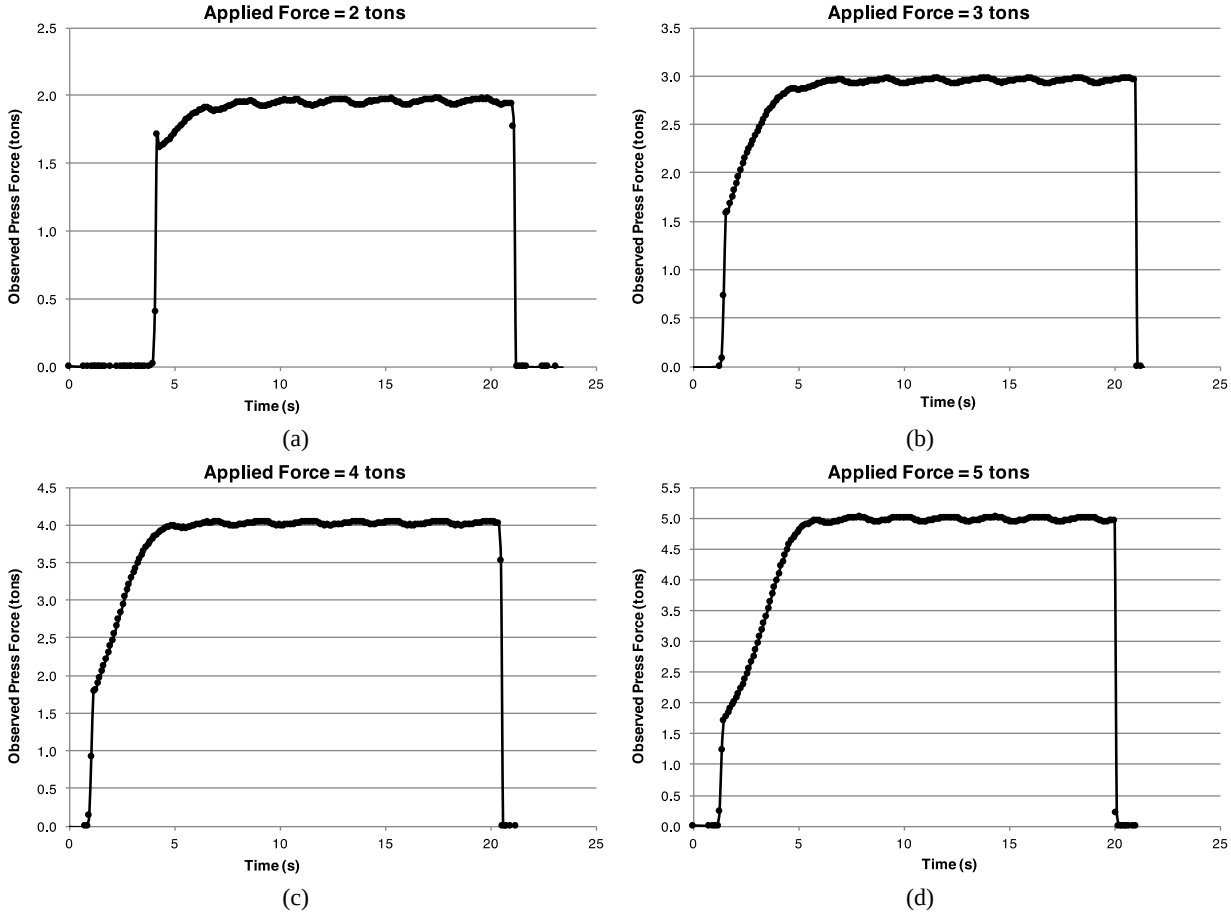

Figure 5-2. Press force versus time data collected for batches formed at applied force of (a) 2 tons, (b) 3 tons, (c) 4 tons and (d) 5 tons.

The data shown in Figure 5-2 confirms that once the applied force is increased beyond the value of the initial spike, no further spikes are observed. In subsequent analyses the applied formation pressure is discussed rather than the press force. Because CIP involves hydrostatic pressure and two different specimen geometries are being evaluated, a discussion of pressure (P) rather than force (F) is more suitable. In all cases the applied formation pressure will be

calculated using the following formula: $P = F/A_c$, where A_c is the area of the loading face of the specimen.

5.1.2. Physical Property Evaluation

Once the pre- and post- densification dimensional measurement data was collected, the volumetric strain ($\Delta V/V$) in each batch was compared to the applied formation pressure and the results can be seen in Figure 5-3.

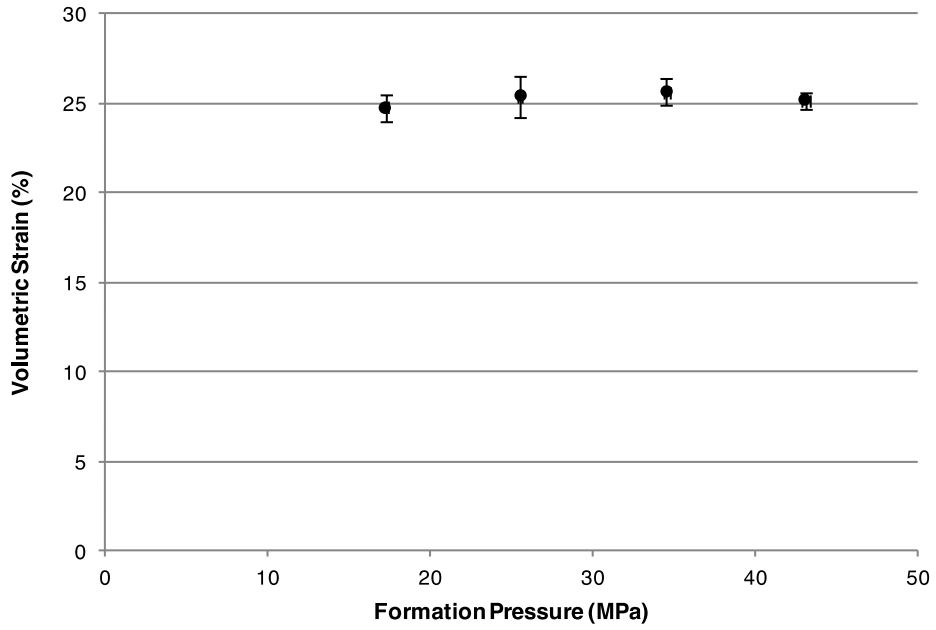

Figure 5-3. Relationship between applied formation pressure and volumetric shrinkage.

Figure 5-3 shows data for four batches of specimens formed at pressures between ~17.5 and ~43.5 MPa, which correspond to press forces of 2 and 5 tons. Each data point in the plot above represents the arithmetic mean of 20 square specimens. Variation in the volumetric strain exhibited by each batch is shown by the vertical error bars, which represent the arithmetic standard deviation. Variation in the formation pressure applied to each batch is shown by the horizontal error bars, which represent the arithmetic standard deviation. However, variations in applied pressure are quite small and can barely be seen in the plot.

Recall that it was hypothesized that, as the formation pressure was increased, the packing density would increase in proportion. It was therefore expected that the volumetric strain induced through densification would show a proportional relationship with applied pressure. However, this was not observed and from Figure 5-3 it can be seen that volumetric strain remains constant in this range of applied pressure. From this, it can be inferred that when the formation pressure is varied between 17.5 and 43.5 MPa, the effect on packing density is negligible.

Analysis of the specimens via the Archimedes' method resulted in mean values of apparent porosity ranging from ~8.38 to ~11.5%. The relationship between formation pressure and apparent porosity is shown in Figure 5-4.

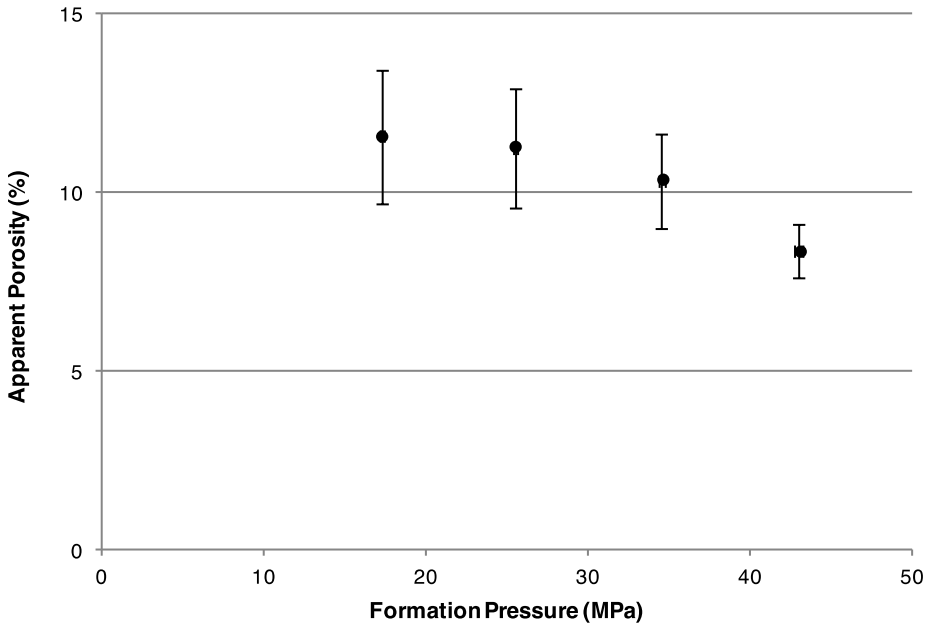

Figure 5-4. Relationship between formation pressure and apparent porosity.

The data points represent the arithmetic mean of 20 specimens. Variation present in the apparent porosity is shown by the vertical error bars, which represent the arithmetic standard deviation for each batch. Again, variations present in the applied formation pressure are small enough that they can barely be seen in the plot above. In this range of formation pressure, it

appears that as the pressure is increased, the apparent porosity decreases. However, a strong argument supporting this relationship cannot be made, because of the magnitude of the standard deviations and the overlap between standard deviations for pressures between ~17.5 and ~35 MPa.

Given this data and the desire to keep applied pressures as close as possible to those used in the masonry industry, formation pressures of 17.5 MPa were applied in the subsequent studies of the effects of geometric distortion and peak densification temperature on the physical and mechanical properties of the material.

5.2 Evaluation of the Effects of Geometric Distortion

The purpose of polishing the loading surfaces of specimens was primarily to ensure that specimens made full contact with the loading surface and load was therefore transferred to the entire specimen. It was expected that proper seating and loading would minimize the discontinuities observed in the elastic portion of the stress-strain curves. It was further hypothesized that observed non-linearities in the elastic region of the curves could, at least partially, be attributed to dimensional distortion exhibited in fired and unpolished specimens.

The effects of geometric distortion and peak densification temperature were evaluated simultaneously. 28 batches of 20 specimens (a total of 560) were prepared. 14 batches were polished after densification, while the other 14 were left unpolished. In each set of 14 batches, seven batches of square specimens were prepared for subsequent compressive loading and seven batches of rectangular specimens were prepared for transverse loading. Each batch in these subsets was densified at a peak temperature between 705 and 790°C. Variations between unpolished and polished specimens are shown in this section and the full set of data will be compared in the next section of this chapter (Section 5.3).

In Figure 5-5, the stress-strain curves generated from compressive testing of two similarly prepared batches of specimens is shown. All specimens in both batches were prepared in the same manner prior to densification. The batch shown in Figure 5-5b was polished after densification, while the batch shown in Figure 5-5a was not.

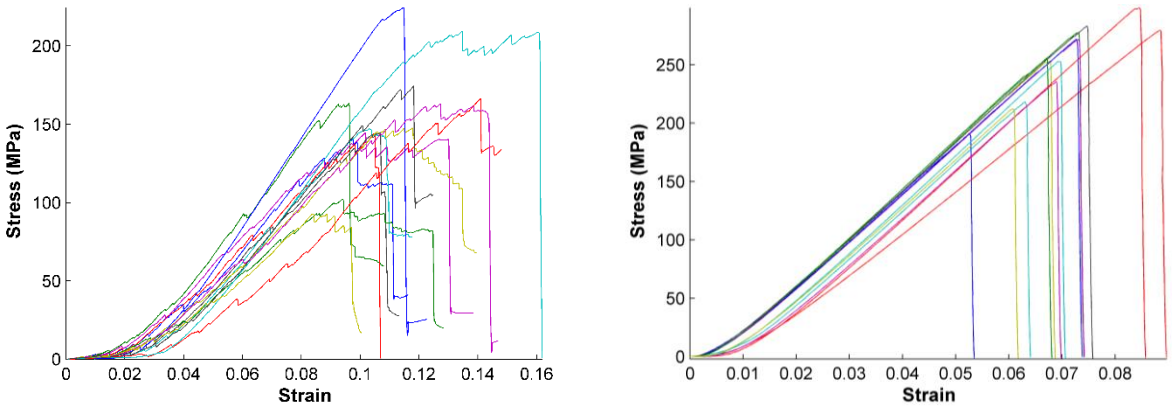

(a) (b)

Figure 5-5. Comparison of stress-strain behavior under compressive loading: (a) unpolished specimens and (b) polished specimens.

The data shown above is characteristic of all batches that were tested under compressive loading conditions. From the stress-strain plots, four significant observations can be made:

1. The plot of polished specimens shows an absence of discontinuities in the elastic portion of the curve. This is in stark contrast to the plot for the unpolished specimens.
2. Non-linearity in the elastic portion of the curve is limited to the region where strain is below ~0.015 for polished specimens, whereas the region extends to ~0.05 for unpolished specimens.
3. For polished specimens, the elastic portion of the curve terminates with a sharp drop in stress. This is associated with catastrophic failure of the specimens and is consistent with behavior observed in most brittle materials.

4. The maximum stress experienced appears to be, on average, higher for polished specimens and the values for maximum stress appear to be more tightly grouped.

In Figure 5-6, the stress-strain curves generated from flexural testing of two similarly prepared batches of specimens is shown. All specimens in both batches were prepared in the same manner prior to densification. Specimens in the batch shown in Figure 5-6b were polished after densification, while specimens in the batch shown in Figure 5-6a were not.

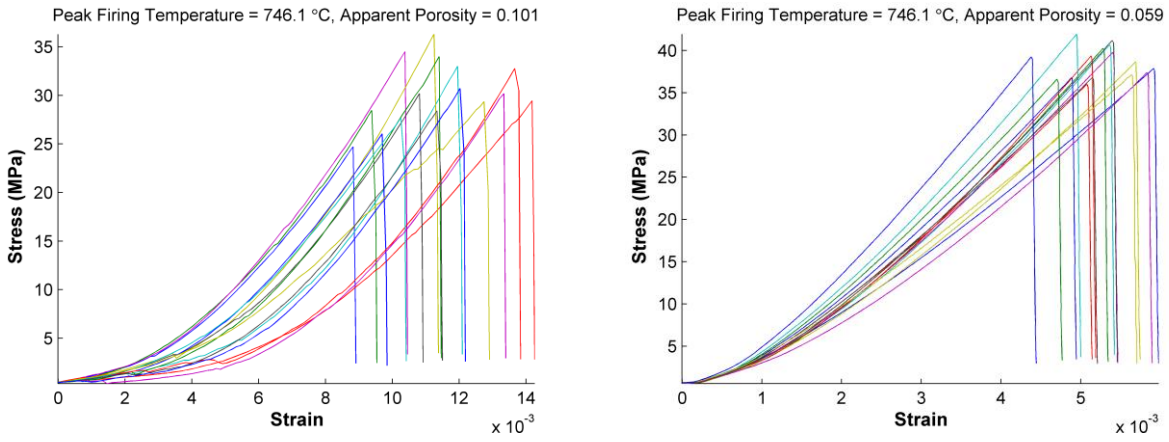

(a) (b)

Figure 5-6. Comparison of stress-strain behavior under flexural loading: (a) unpolished specimens and (b) polished specimens.

The data shown above is characteristic of all batches that were tested under transverse loading conditions. Although data from the unpolished specimens is a bit better behaved under transverse loading, similar observations can be made. Stress-strain curves generated from polished specimens showed an absence of discontinuities and the non-linear portion of the elastic region has been reduced. In addition, the maximum stress experienced is on average higher for polished specimens and variation in maximum stress appears to significantly be reduced

5.3 Evaluation of the Effects of Machine Compliance

Machine compliance was evaluated as described in Section 4.2.2. Once the load and crosshead deflection data was collected from testing of the calibration specimens, the machine

compliance and machine deflection were calculated using Equations 4.1 & 4.2. The results of these calculations can be seen in Figures 5-7 & 5-8, which show the results from compressive and transverse loading respectively. The apparent deflection is shown in blue, the specimen deflection is shown in grey and the machine deflection is shown in red.

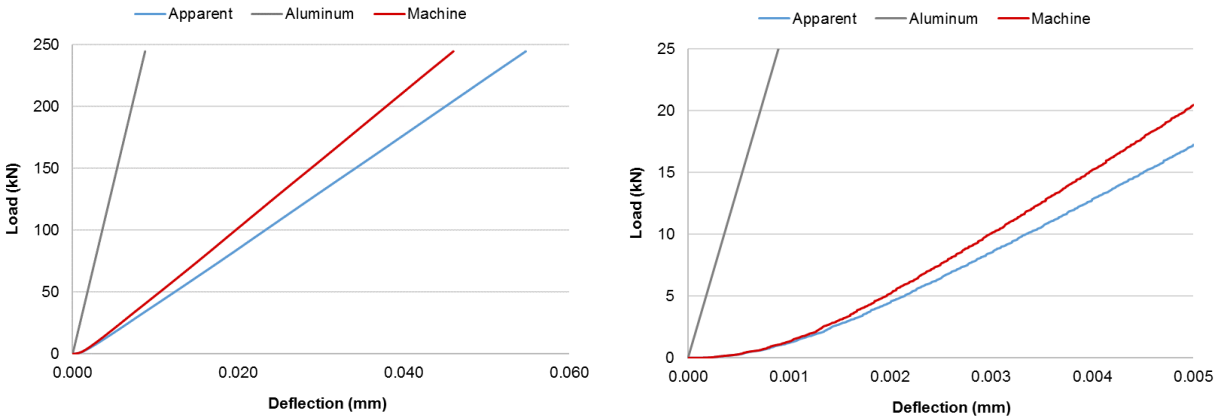

(a) (b)

Figure 5-7. Load-displacement data for machine compliance evaluation under compressive loading: (a) 0-250kN and (b) 0-25kN.

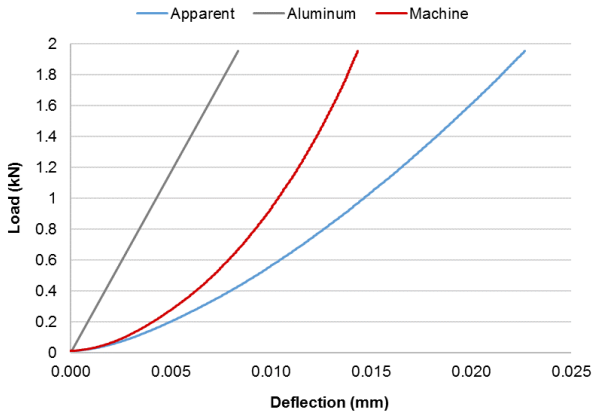

Figure 5-8. Load-displacement data for machine compliance evaluation under transverse loading.

Figure 5-7a shows that both the load-deflection curves for both the crosshead and the loading system are quite linear through most of the loading range. However, some non-linearity is present when loads under ~5kN are applied (Figure 5-7b). On the other hand, under transverse

loading the curves representing both the crosshead and the loading system are quite non-linear throughout the full loading range (Figure 5-8).

Once the machine compliance was calculated it was used to correct the experimentally obtained crosshead deflection data and calculate the actual deflection experienced by the porous glass specimens under investigation. The results from two characteristic specimens are shown in Figure 5-9, where the apparent deflection is shown in red, the machine deflection is shown in black and the actual deflection is shown in blue. Figure 5-9a and 5-9b depict the data from compressively loaded and transversely loaded specimens respectively.

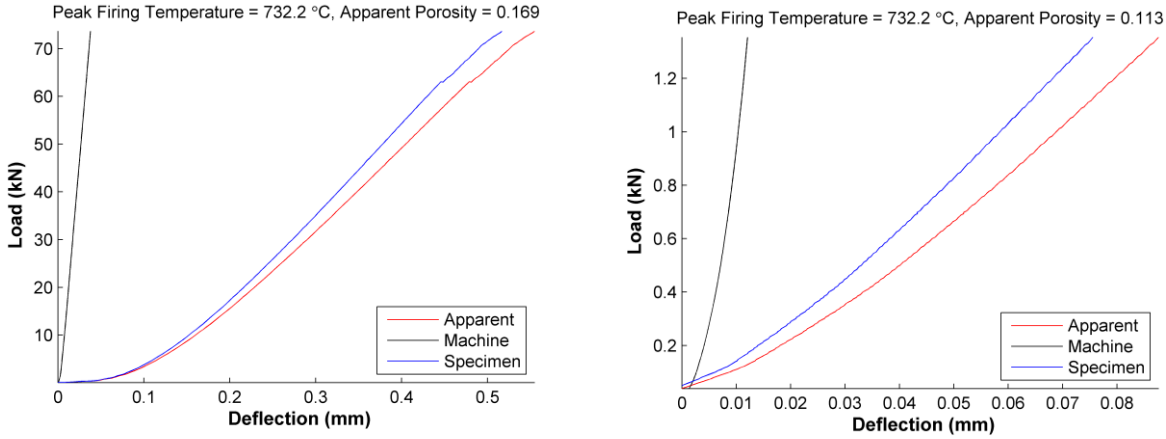

(a) (b)

Figure 5-9. Load-displacement data corrected for machine compliance: (a) compressive loading and (b) transverse loading.

From Figure 5-9a, two important observations can be made. First, it can be seen that the compliance correction had a negligible effect on the non-linear portion of the load-displacement curve. Therefore, it is hypothesized that the non-linearity is due to the behavior of the specimen itself. This non-linearity is somewhat common in porous materials; as a load is applied, dynamic modifications in the structure of the particles and the pore system may occur. Second, the slope of the linear portion of the curve is noticeably steeper, which will result in lower calculated

values for strain and subsequently a higher calculated value for the elastic modulus in compression.

Similar observations can be made with respect to transversely loaded specimens as shown in Figure 5-9b. The distinct initial non-linearity in the load-displacement curve appears to be unaffected by the machine compliance correction and the majority of the load-displacement curve appears to be noticeably steeper.

5.4 Evaluation of the Effects of Peak Densification Temperature

As discussed in the previous section, a total of 560 specimens were prepared and evaluated in batches of 20. Four sets of batches were created. The first set of 7 batches of specimens was unpolished and subjected to compressive loading. The second set was left unpolished and subjected to transverse loading. The third set was polished as described previously (Section 4.1.3) and subjected to compressive loading. The fourth set was also polished and then subjected to transverse loading.

5.4.1. Physical Property Evaluation

As all specimens were subjected to the same procedures until just prior to mechanical testing, the results from all four sets of data are shown together. Each data point in the subsequent plots in this section represents the arithmetic mean of 40 compression specimens and 40 flexure specimens.

5.4.1.1. Volumetric Strain: Once the dimensional measurement data was collected, the volumetric strain induced through densification was compared to the peak densification temperature, as shown in Figure 5-10.

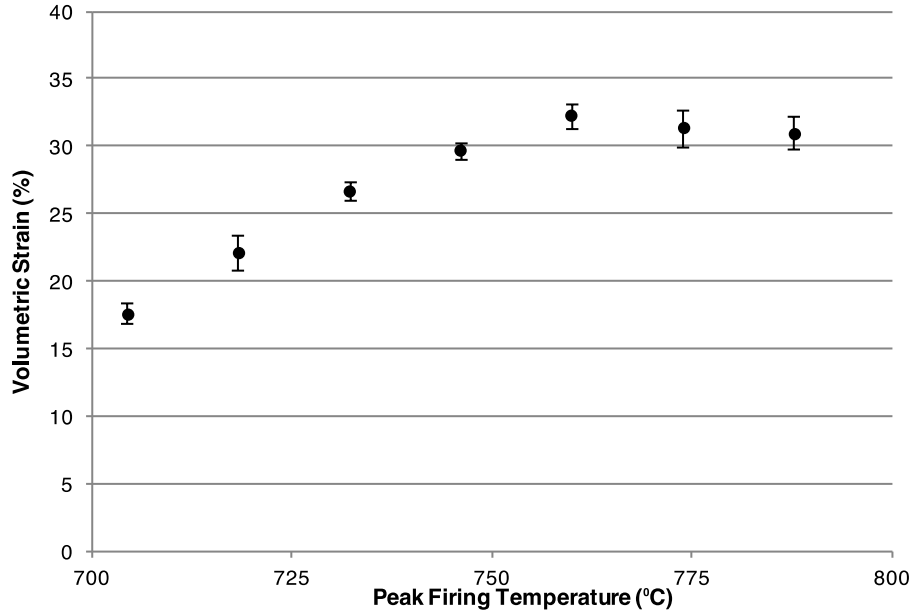

Figure 5-10. Relationship between peak densification temperature and volumetric shrinkage.

Variation in each batch is shown by the vertical error bars, which represent the arithmetic standard deviation. Figure 5-10 shows that, when peak densification temperatures are varied within 705 and 760°C range, the volumetric strain and the peak densification temperature are linearly related. Above 760°C the volumetric strain appears to stay steady at slightly over 30%. It should be noted that at these elevated temperatures geometric distortion is more severe and the accuracy of measurements may fall off.

5.4.1.2. Apparent Porosity & Bulk Density: Analysis of the specimens via the Archimedes' method resulted in mean values of apparent porosity ranging from ~0.6 to ~24.7% and bulk density ranging from ~1.8 to ~2.2 g/cm^3. Volumetric strain is compared with apparent porosity in Figure 5-11.

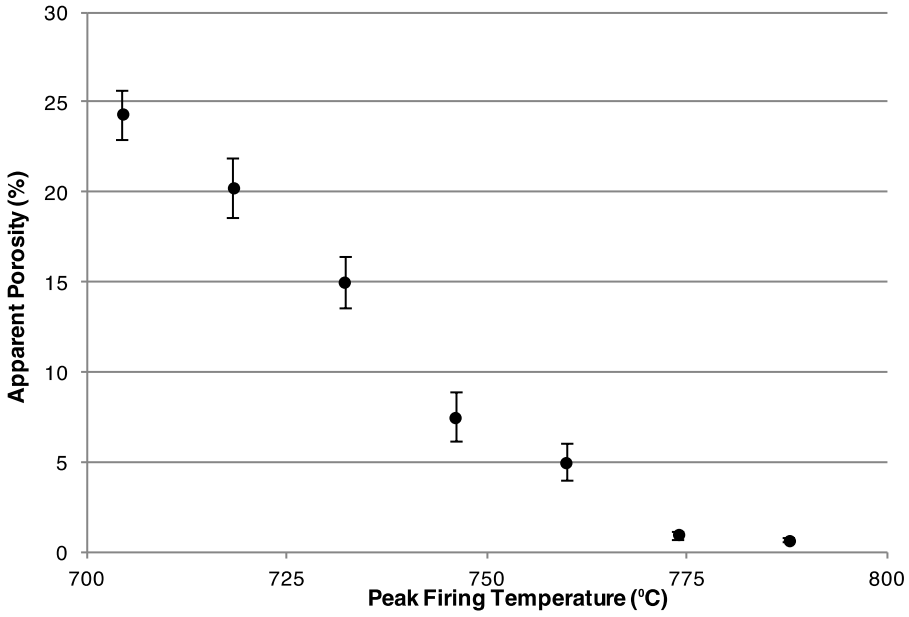

Figure 5-11. Comparison of peak densification temperature and resulting apparent porosity.

Variation present in the apparent porosity is shown by the vertical error bars, which represent the arithmetic standard deviation for each batch. Again, within the 705 to 760°C range, the porosity and the peak densification temperature appear to be linearly related. Above 760°C the apparent porosity appears to exhibit little change. This temperature corresponds to the onset of crystallization in soda-lime silicate glasses. Because of the variability in composition of the feedstock, some of the particles may have begun to crystallize while others not have.

The bulk density of the specimens as it relates to peak densification temperature is shown in Figure 5-12. The vertical error bars represent the standard deviation in bulk density.

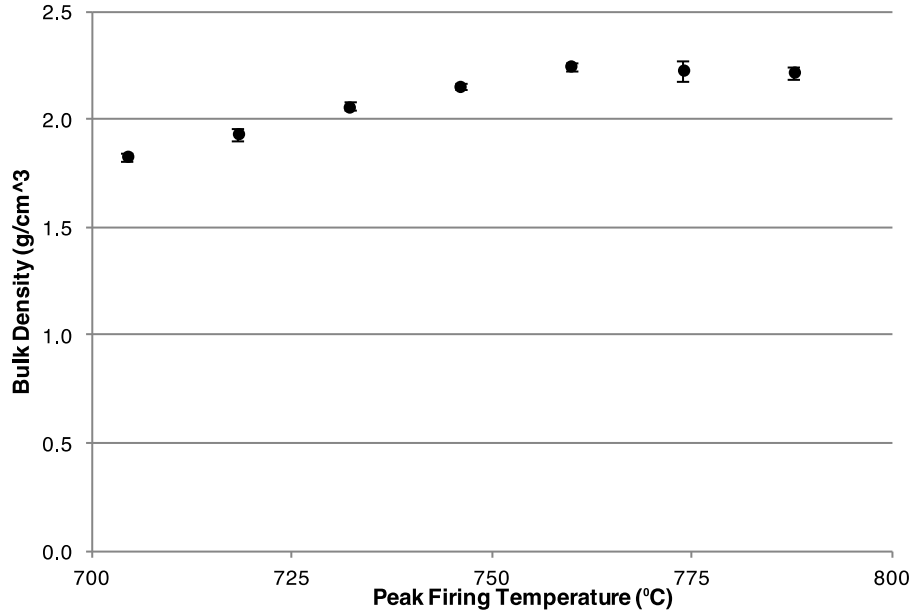

Figure 5-12. Relationship between peak densification temperature and bulk density.

Figure 5-12 indicates a linear relationship between densification temperature and bulk density in the range of 705 to 760°C, as expected from the previous results. Again, above ~760°C the bulk density appears to remain steady. It should be noted that the non-linear results shown for both apparent porosity and bulk density in the higher temperatures may also be due to limitations with the Archimedes' test method, which does not account for closed pores within the material. At elevated temperatures, it is expected that pores within the material, which were once open, begin to become isolated from the porous network and formation of closed pores is accelerated.

5.4.2. COMPRESSIVE BEHAVIOR

5.4.2.1. Stress-Strain Behavior Under Compressive Loading: The stress-strain behavior of the 14 batches of compressive specimens can be seen on the next few pages in Figures 5-13 through 5-19. The data is grouped in batches and is shown in order of ascending peak densification

temperature (705-790°C), which corresponds to apparent porosity values between 0.5 and 25.8%.

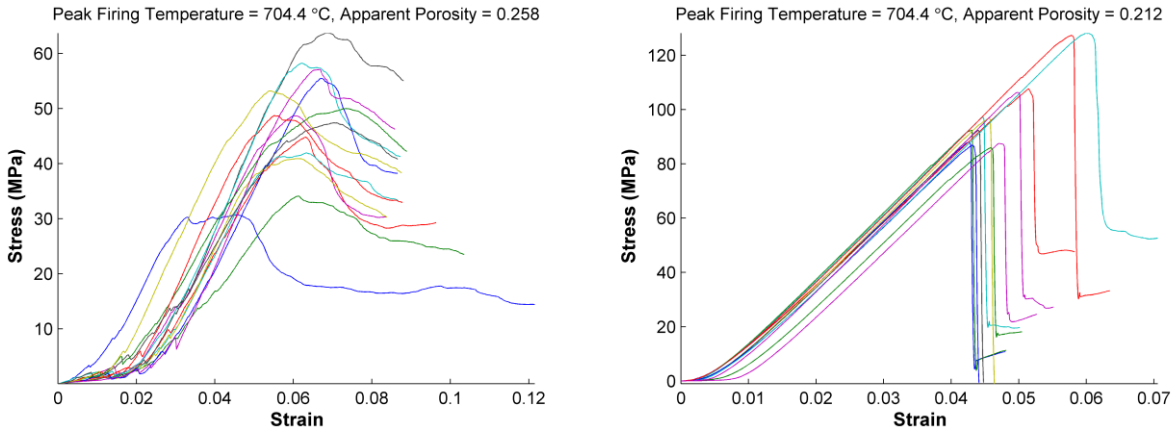

(a) (b)

Figure 5-13. Stress-strain curves for compressively loaded specimens densified at 704.4°C: a) unpolished and b) polished.

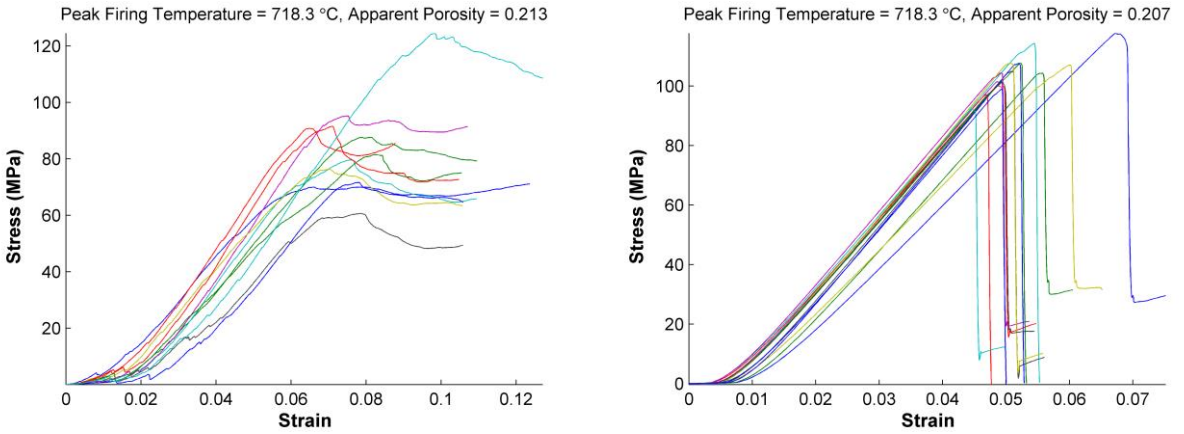

(a) (b)

Figure 5-14. Stress-strain curves for compressively loaded specimens densified at 718.3°C: a) unpolished and b) polished.

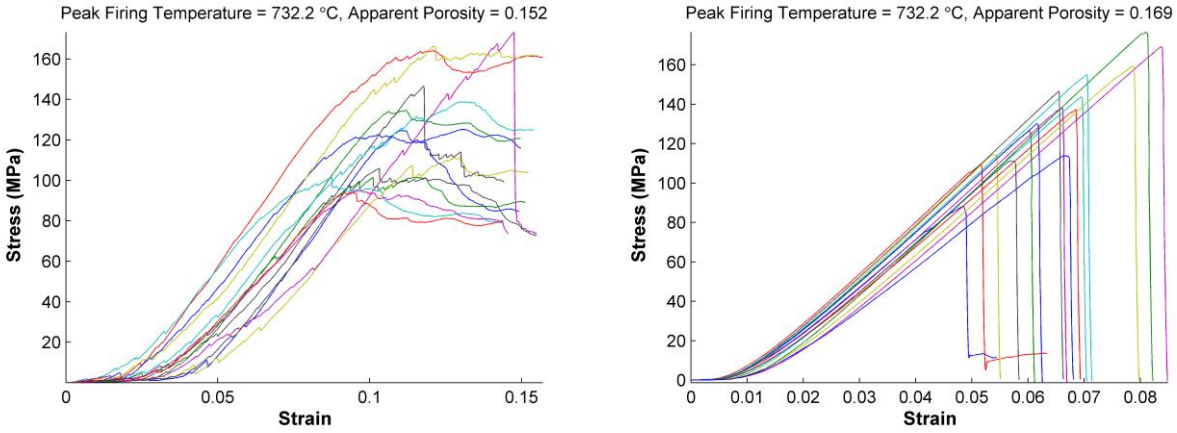

(a) (b)

Figure 5-15. Stress-strain curves for compressively loaded specimens densified at 732.2°C: a) unpolished and b) polished.

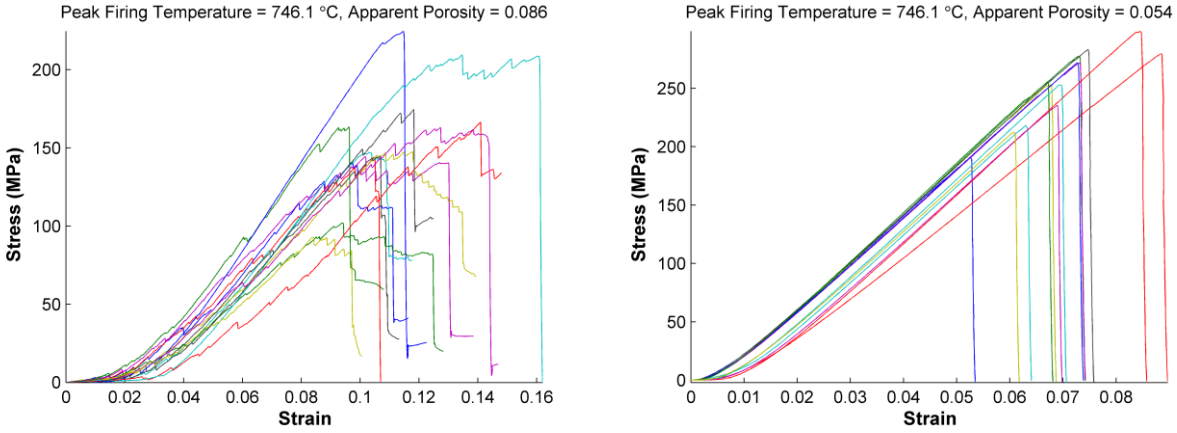

(a) (b)

Figure 5-16. Stress-strain curves for compressively loaded specimens densified at 746.1°C: a) unpolished and b) polished.

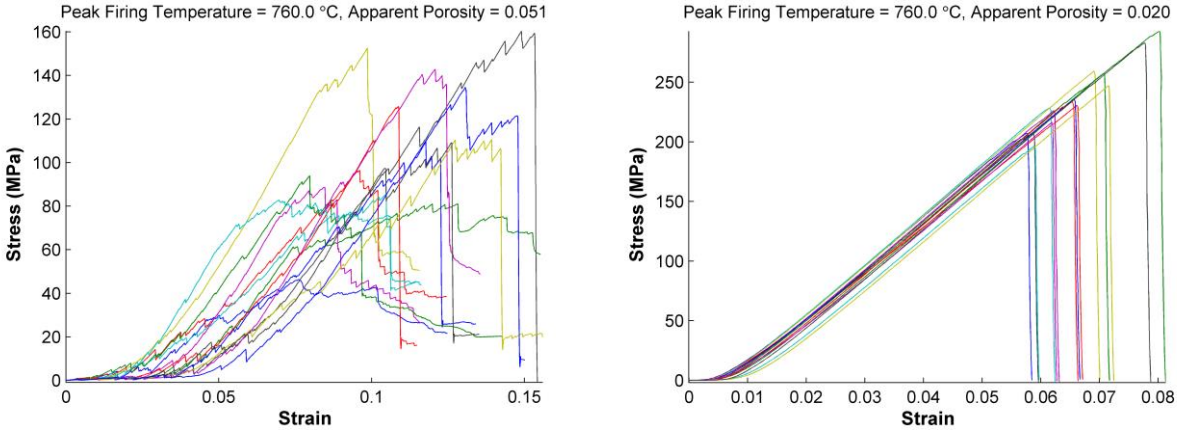

(a) (b)

Figure 5-17. Stress-strain curves for compressively loaded specimens densified at 760°C: a) unpolished and b) polished.

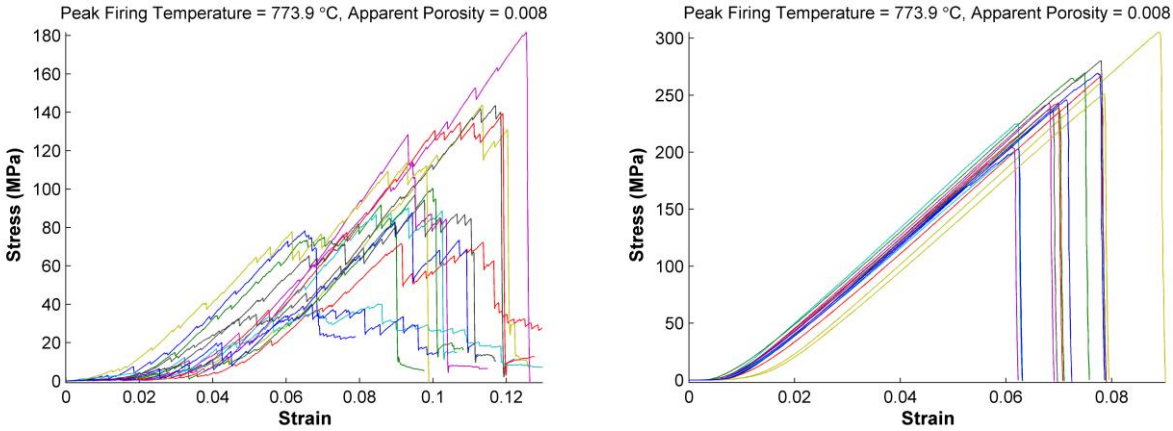

(a) (b)

Figure 5-18. Stress-strain curves for compressively loaded specimens densified at 773.9°C: a) unpolished and b) polished.

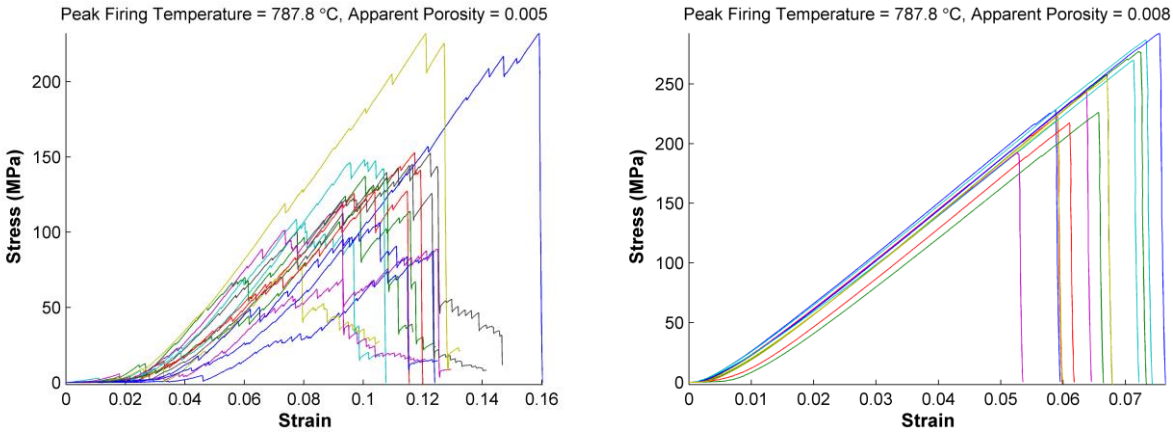

(a) (b)

Figure 5-19. Stress-strain curves for compressively loaded specimens densified at 787.8°C: a) unpolished and b) polished.

From Figures 5-13 through 5-19, it can be seen that, within each batch, the specimens behave similarly through the elastic portion of the curves. The data associated with polished specimens is very well behaved when compared to the data associated with the unpolished specimens; this is consistent with the previous results presented with respect to geometric distortion. It should be noted that, even in the case of polished specimens, the stress-strain behavior appears to be non-linear during initial loading. Inspection of the stress-strain curves also shows that the maximum stress exhibited by specimens in a given batch can vary considerably. In unpolished specimens, as the peak densification temperature increases,

scattering in the data increases alongside it, with some specimens exhibiting maximum stress values two to four times higher than other specimens in the same batch. However, although some scattering is present for polished specimens, that variation is less pronounced and does not increase with densification temperature. Further, polished specimens undergo sudden, catastrophic failure, while unpolished specimens appear to exhibit one or more plateau of reduced stress after the maximum stress is achieved.

5.4.2.2. Elastic Modulus Under Compressive Loading: In order to evaluate the elastic modulus, the stress-strain curves were corrected for machine compliance and truncated as described in Section 4.2.2. The linear portion of the stress-strain curves can be seen in Figures 5-20 through 5-26 on the following pages. Again, the results are shown in order of ascending densification temperature (705–790°C).

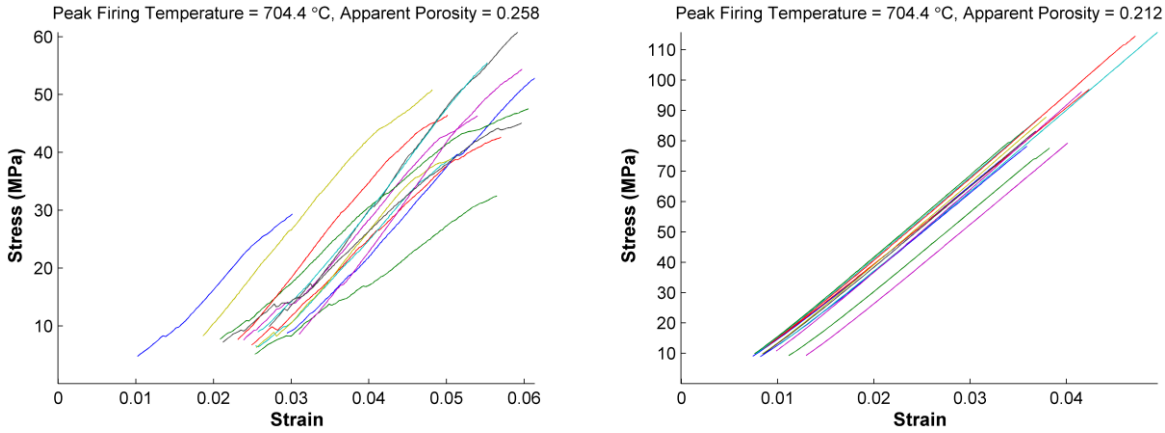

(a) (b)

Figure 5-20. Truncated stress-strain curves for compressively loaded specimens densified at 704.4°C: a) unpolished and b) polished.

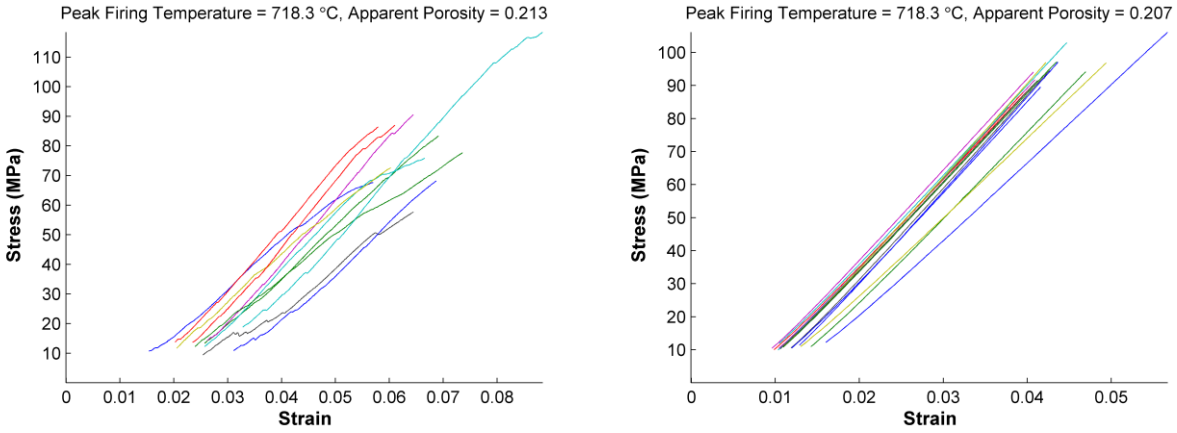

(a) (b)

Figure 5-21. Truncated stress-strain curves for compressively loaded specimens densified at 718.3°C: a) unpolished and b) polished.

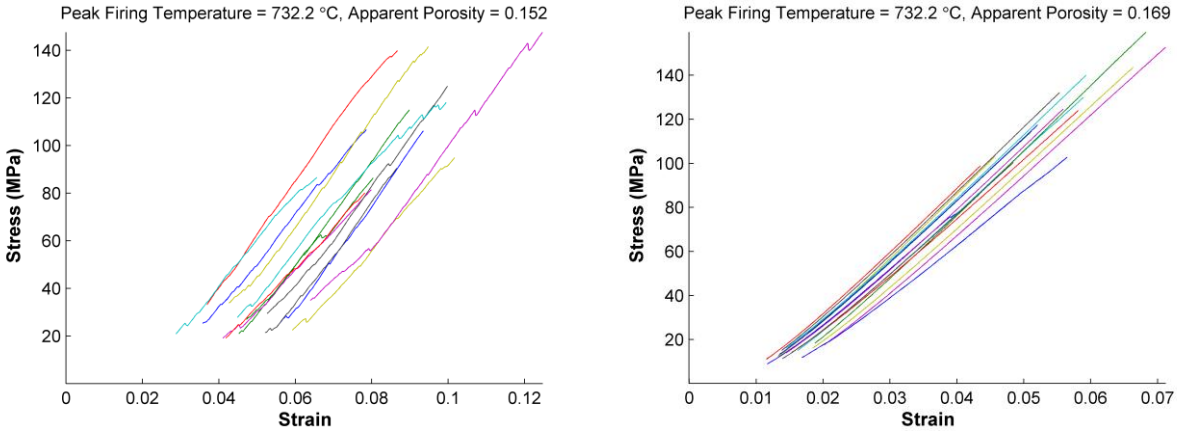

(a) (b)

Figure 5-22. Truncated stress-strain curves for compressively loaded specimens densified at 732.2°C: a) unpolished and b) polished.

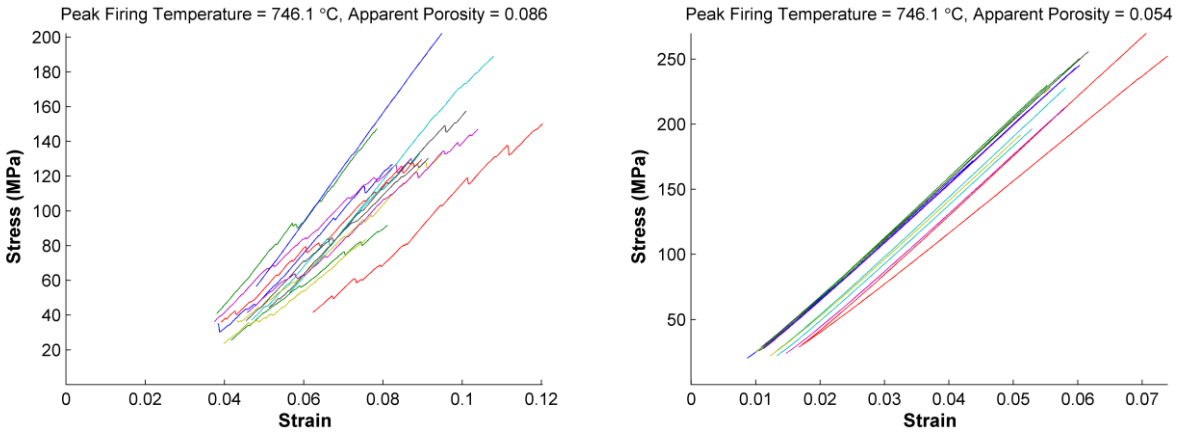

(a) (b)

Figure 5-23. Truncated stress-strain curves for compressively loaded specimens densified at 746.1°C: a) unpolished and b) polished.

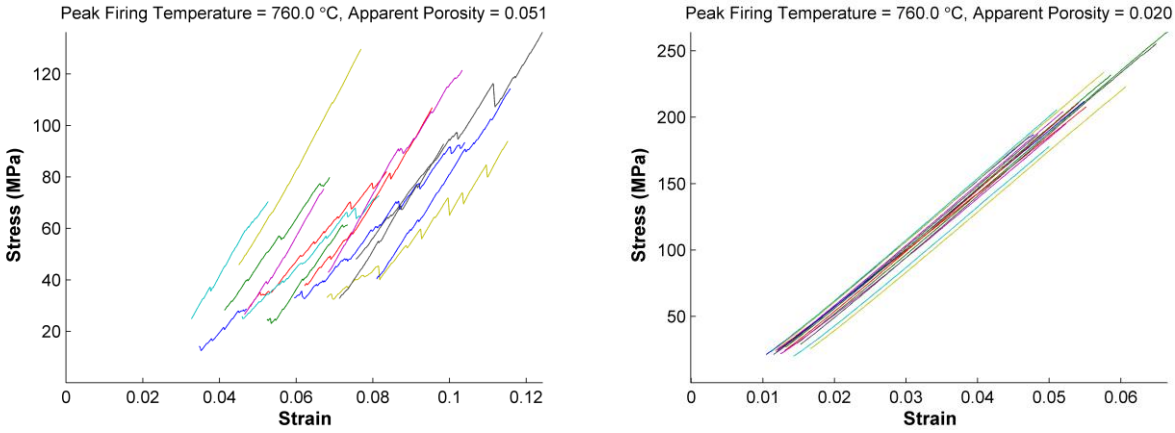

(a) (b)

Figure 5-24. Truncated stress-strain curves for compressively loaded specimens densified at 760°C: a) unpolished and b) polished.

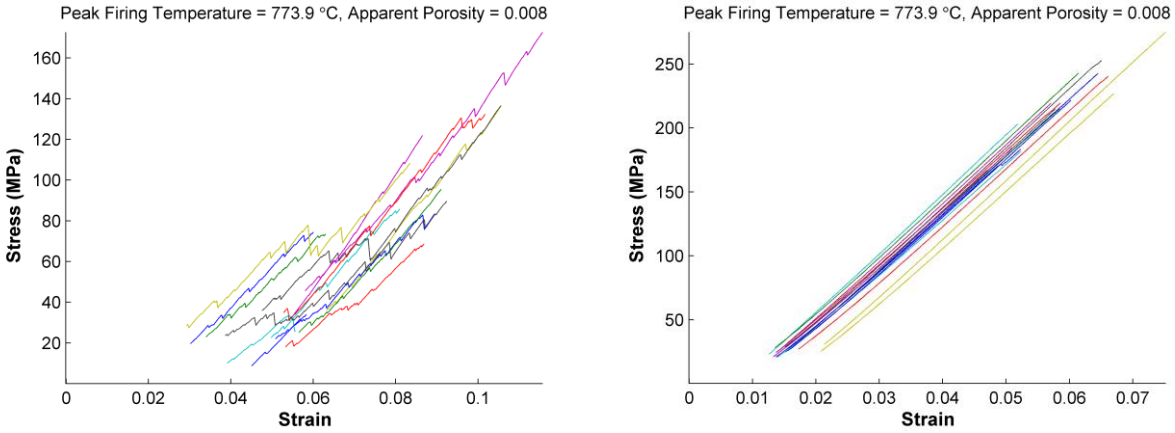

(a) (b)

Figure 5-25. Truncated stress-strain curves for compressively loaded specimens densified at 773.9°C: a) unpolished and b) polished.

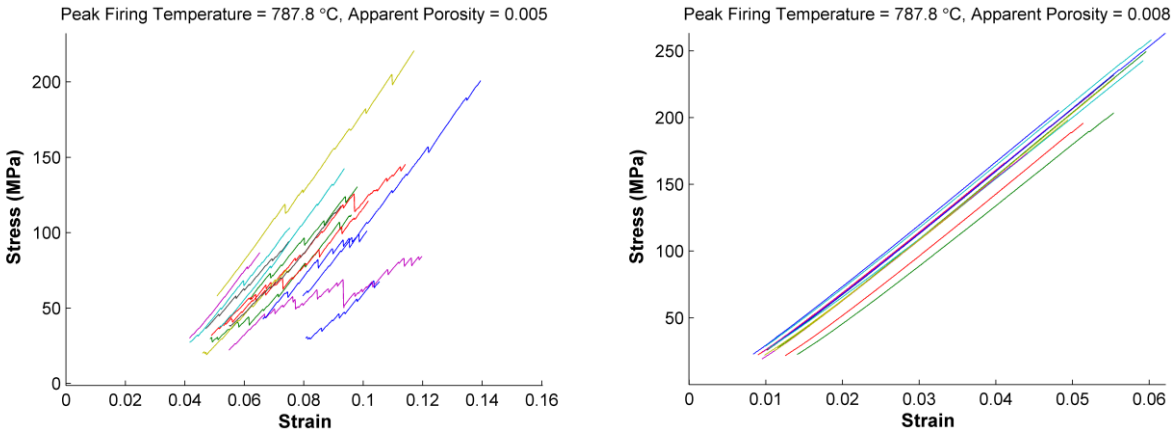

(a) **(b)**

Figure 5-26. Truncated stress-strain curves for compressively loaded specimens densified at 787.8°C: a) unpolished and b) polished.

The behavior observed throughout the elastic region of the stress-strain curves is quite different for unpolished versus polished specimens. In unpolished specimens, this region is marked by discontinuities and load drops with an increase in occurrence and severity correlating to increased temperature. For unpolished specimens, in the lower temperature ranges some roughly linear behavior can be observed and the slopes of these portions of the curves are somewhat similar within a given batch. As the temperature is increased, linearity decreases markedly and the slopes of any linear portions of the curves are quite dissimilar. For the polished specimens, once the initial non-linearity is omitted from the data, the elastic portion of the curves is quite well behaved for specimens fired at all temperatures. Discontinuities and load drops are not present and the curves can be characterized by linear behavior. Within any given batch, the slopes of the curves are observed to be very similar.

5.4.2.3 Weibull Analysis of Compressive Strength: Once data was collected from compressive testing, it was analyzed using the Weibull approach as discussed in section 4.2.2. The results of Weibull analysis are summarized in Tables 5-1 & 5-2 and Weibull probability plots are shown in Appendix C.

Table 5-1. Summary of Weibull data for compressive strength (unpolished specimens).

Apparent Porosity	Mean (MPa)	Std. Dev. (MPa)	Scale Factor (MPa)	Modulus
25.8038	48.2516	8.8963	51.8575	6.3322
21.3026	84.0462	18.8850	91.4259	5.1062
15.2209	114.6588	45.0285	128.8483	2.7515
8.5837	145.4308	40.2361	160.3078	4.0620
5.1337	108.1413	29.9428	119.2097	4.0585
0.8033	103.2072	37.8287	115.6238	2.9718
0.4497	135.7791	46.8493	151.6461	3.1789

Table 5-2. Summary of Weibull data for compressive strength (polished specimens).

Apparent Porosity	Mean (MPa)	Std. Dev. (MPa)	Scale Factor (MPa)	Modulus
21.2498	99.1981	17.1316	106.2090	6.7958
20.6624	104.1739	7.6069	107.4964	16.8763
16.9154	134.6681	24.6225	144.6612	6.3898
5.3815	254.5172	29.1717	266.9614	10.5263
1.9528	236.3286	31.8982	249.7550	8.8502
0.8404	245.0149	32.1210	258.5709	9.1290
0.8121	245.2810	31.3382	258.5362	9.3823

The tabulated data shows that for unpolished specimens, the mean compressive strength ranges from 48.25 to 135.78 MPa and values for the Weibull modulus vary from 2.75 to 6.33. For polished specimens, the values for both properties are much higher; compressive strength varies from 99.20 to 245.28 MPa and the Weibull modulus varies between 6.39 and 16.88.

Once the data was analyzed through the Weibull approach, the cumulative distribution function for each of the 14 batches of compressive specimens was calculated. The CDF plots are shown in Figures 5-27 through 5-33. In each of the figures, the experimental data is denoted by blue x's, the Weibull CDF is denoted by the solid red line and the 95% upper and lower confidence bounds are denoted by the dashed red lines.

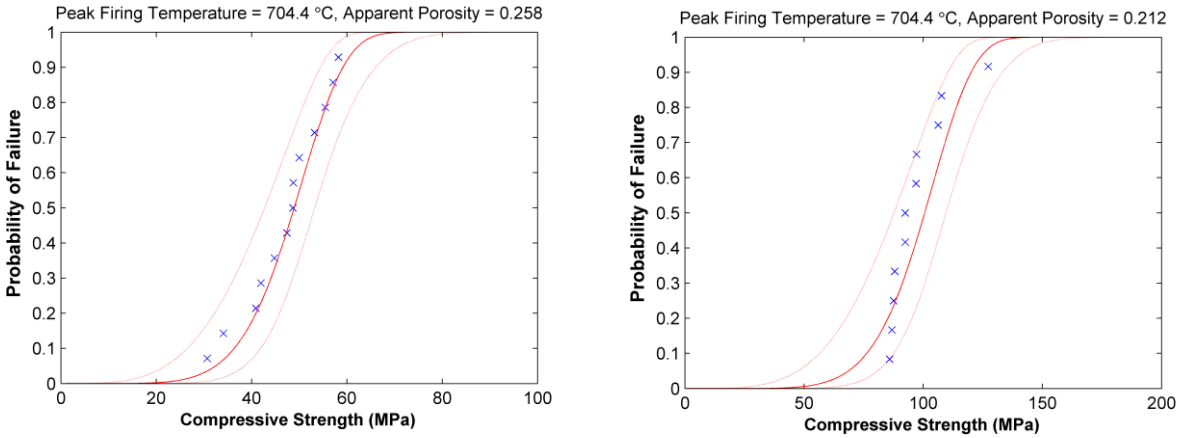

(a) (b)

Figure 5-27. Weibull CDF for compressive strength for specimens densified at 704.4°C: a) unpolished and b) polished.

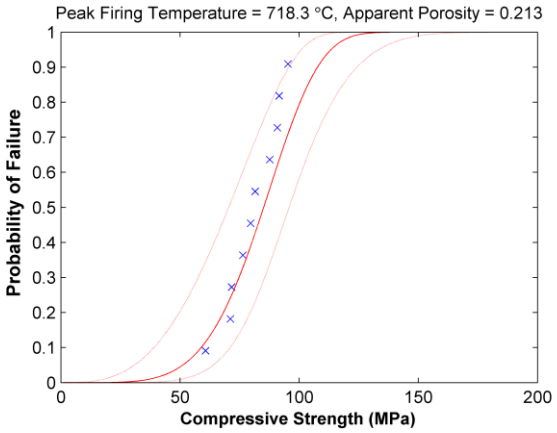

(a)

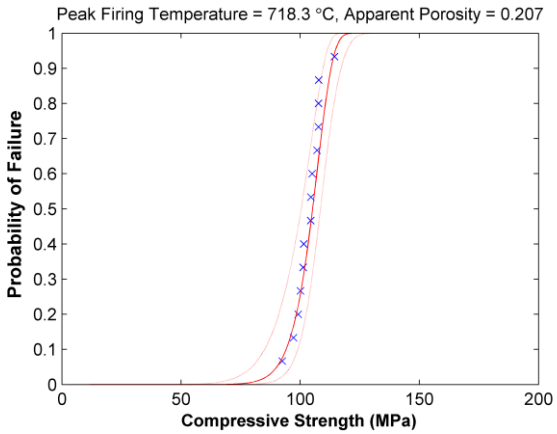

(b)

Figure 5-28. Weibull CDF for compressive strength for specimens densified at 718.3°C: a) unpolished and b) polished.

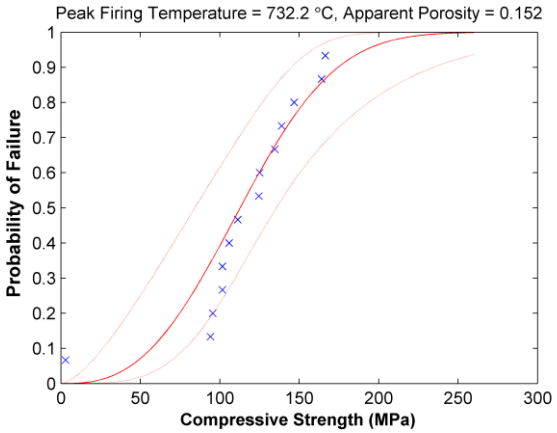

(a)

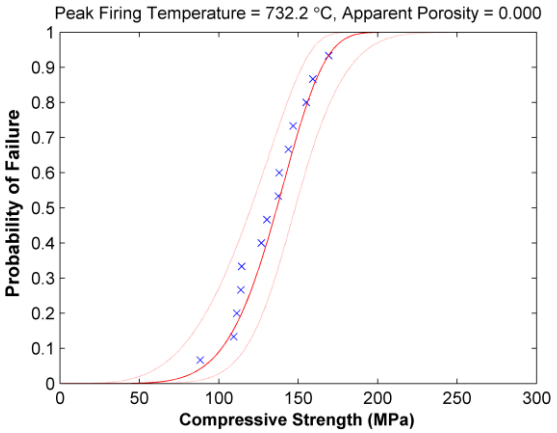

(b)

Figure 5-29. Weibull CDF for compressive strength for specimens densified at 732.2°C: a) unpolished and b) polished.

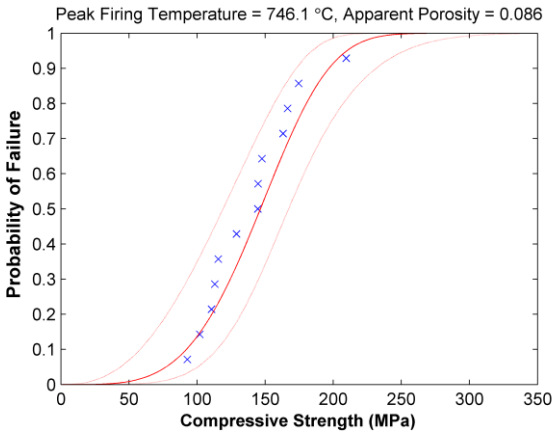

(a)

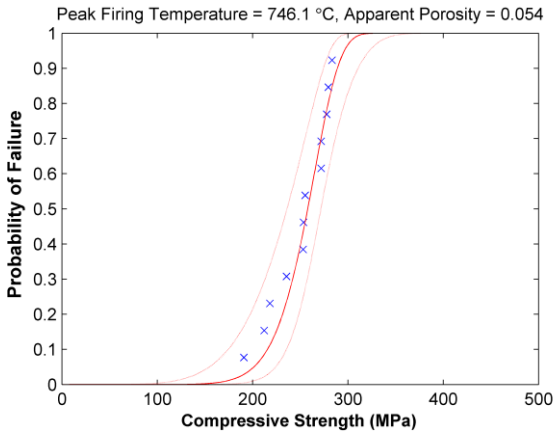

(b)

Figure 5-30. Weibull CDF for compressive strength for specimens densified at 746.1°C: a) unpolished and b) polished.

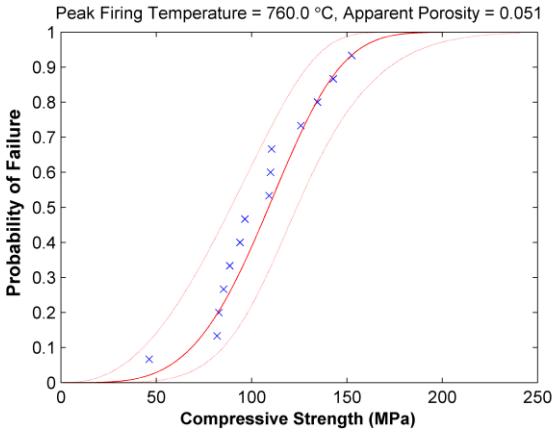

(a)

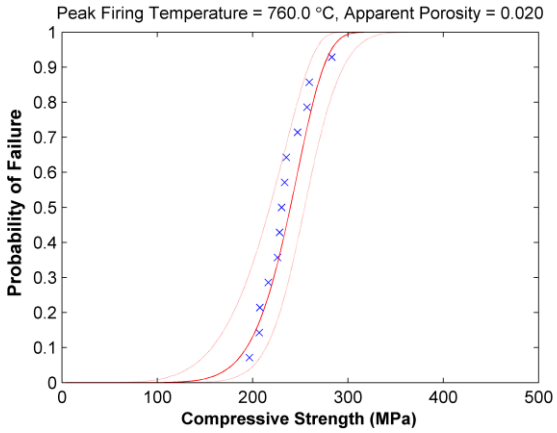

(b)

Figure 5-31. Weibull CDF for compressive strength for specimens densified at 760°C: a) unpolished and b) polished.

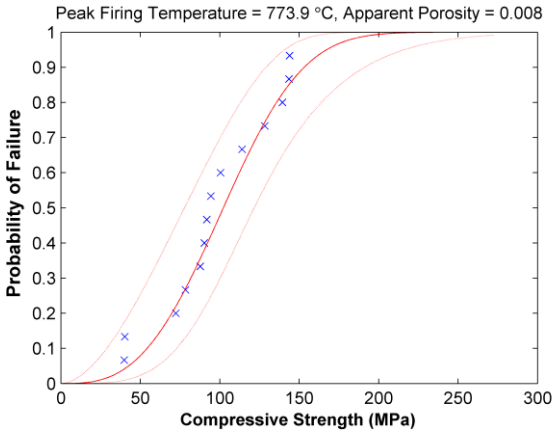

(a)

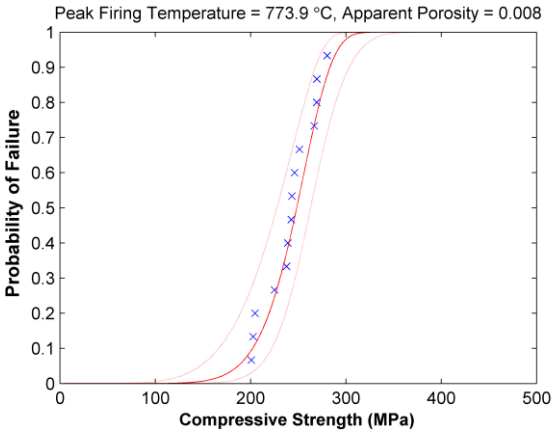

(b)

Figure 5-32. Weibull CDF for compressive strength for specimens densified at 773.9°C: a) unpolished and b) polished.

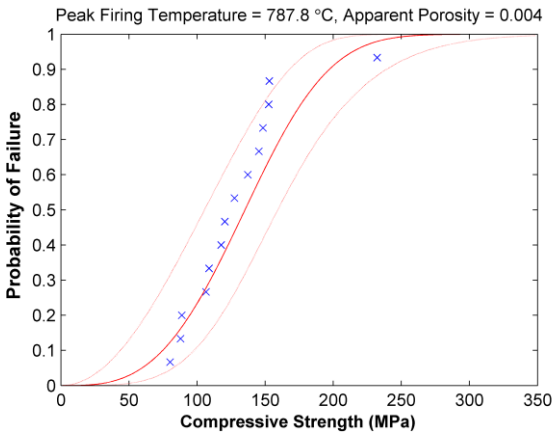

(a)

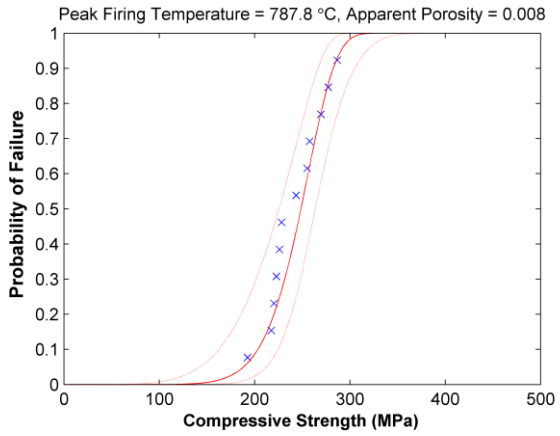

(b)

Figure 5-33. Weibull CDF for compressive strength for specimens densified at 787.8°C: a) unpolished and b) polished.

The Weibull analysis data for each batch of compression specimens is compared graphically in Figures 5-34 & 5-35. In Figure 5-34, the mean compressive strength is plotted against the mean porosity. In Figure 5-35, the Weibull modulus, or shape factor is plotted against mean apparent porosity.

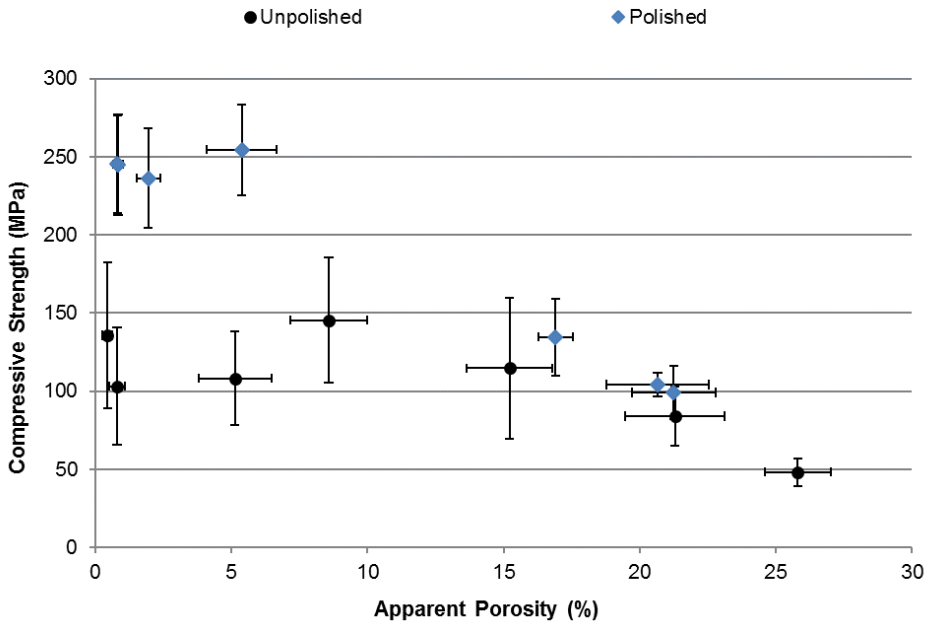

Figure 5-34. Mean compressive strength as a function of porosity.

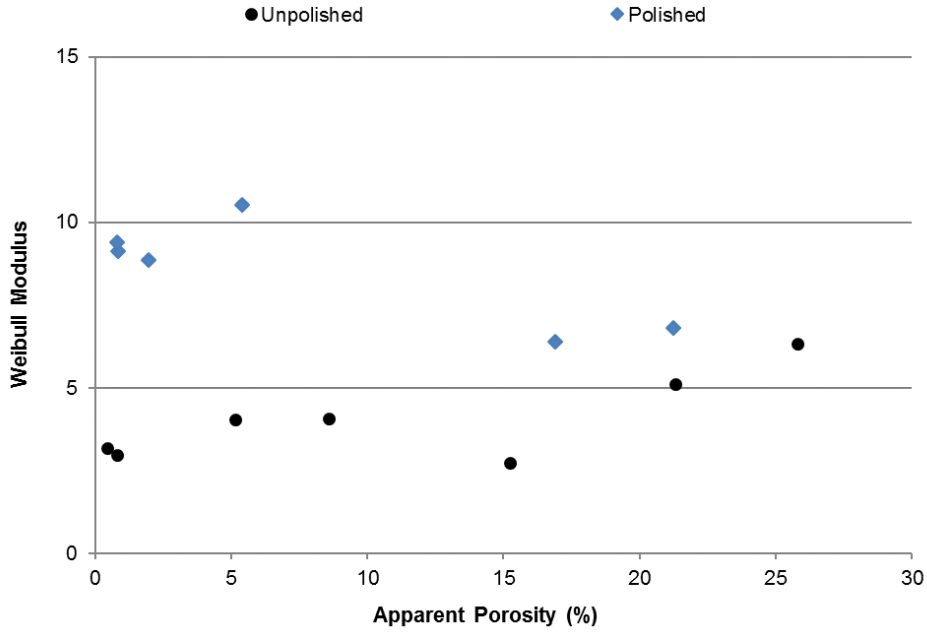

Figure 5-35. Weibull Modulus for compressive strength as a function of apparent porosity.

In Figure 5-34, the vertical error bars represent the Weibull standard deviation in strength, while the horizontal error bars represent the arithmetic standard deviation in apparent porosity. As expected, the mean strength was observed to increase with decreasing apparent porosity. However, the values calculated for compressive strength of specimens exhibiting porosity <10% appear to be grouped. Figure 5-34 also shows that the standard deviation in compressive strength for unpolished specimens varies widely and seems to increase slightly as the apparent porosity decreases. For polished specimens, the standard deviation in compressive strength does not show as much variability, although it does appear to be slightly smaller at higher porosity.

Although the standard deviation is a useful metric in measuring the variation between specimens in a batch, the Weibull modulus is generally a better indicator. This non-dimensional number correlates to the slope of the Weibull CDF and a larger value indicates less variation. In Figure 5-35, the only trend in the data that can be readily observed is that, in all cases, the values for the Weibull modulus are higher for polished specimens.

5.4.2.4 Weibull Analysis of Elastic Modulus Under Compressive Loading: As with the strength versus porosity data, Weibull analysis was performed on the elastic modulus data. The results of the Weibull analysis are summarized in Table 5-3 & 5-4.

Table 5-3. Summary of Weibull data for elastic modulus in compression (unpolished)

Apparent Porosity	Mean (GPa)	Std. Dev. (GPa)	Scale Factor (GPa)	Modulus
25.8038	1.3829	0.2226	1.4749	7.3290
21.3026	1.7089	0.2863	1.8266	7.0226
15.2209	1.9664	0.1995	2.0521	11.9716
8.5837	2.1525	0.4672	2.3364	5.3027
5.1337	1.9165	0.4122	2.0790	5.3564
0.8033	1.8773	0.4482	2.0500	4.7784
0.4497	2.0728	0.4782	2.2586	4.9606

Table 5-4. Summary of Weibull data for elastic modulus in compression (polished)

Apparent Porosity	Mean (GPa)	Std. Dev. (GPa)	Scale Factor (GPa)	Modulus
21.2498	2.6264	0.0659	2.6557	50.4286
20.6624	2.6632	0.1032	2.7090	32.3828
16.9154	2.7128	0.1273	2.7691	26.6206
5.3815	4.4617	0.1132	4.5122	49.8416
1.9528	4.5210	0.0765	4.5553	75.0484
0.8404	4.4505	0.1107	4.4998	50.8618
0.8121	4.5740	0.0706	4.6056	82.3945

The tabulated data shows that for unpolished specimens, mean values for the elastic modulus in compression range from 1.38 to 2.15 GPa and values for the Weibull modulus vary from 4.77 to 11.97. For polished specimens, the values for both properties are much higher; the elastic modulus in compression varies from 2.63 to 4.57 GPa and the Weibull modulus varies between 26.62 and 82.39.

Once the data was analyzed through the Weibull approach, the cumulative distribution function for each of the seven batches of compressive specimens was calculated. The CDF plots are shown in Figures 5-36 through 5-42. In each of the figures the experimental data is denoted by blue x's, the Weibull CDF is denoted by the solid red line and the 95% upper and lower confidence bounds are denoted by the dashed red lines.

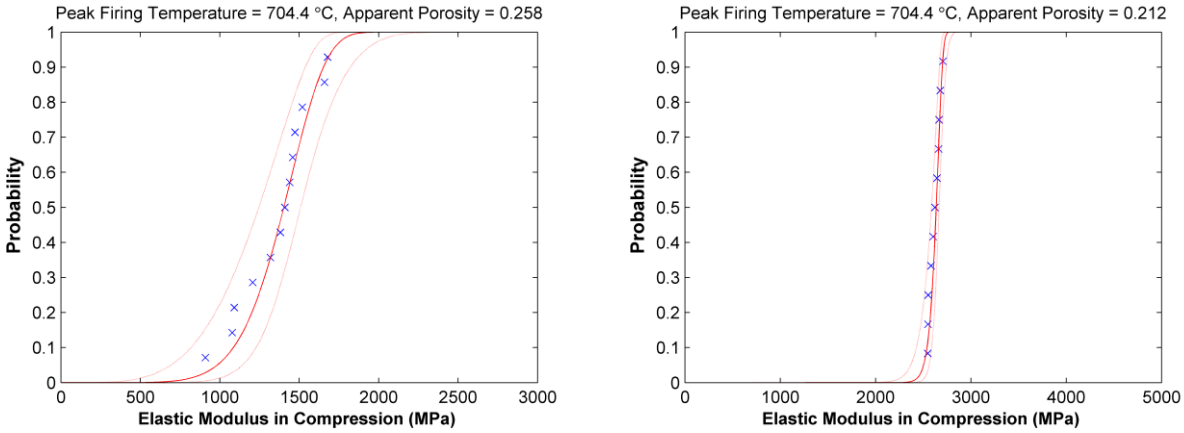

(a) (b)

Figure 5-36. Weibull CDF for elastic modulus in compression for specimens densified at 704.4°C: a) unpolished and b) polished.

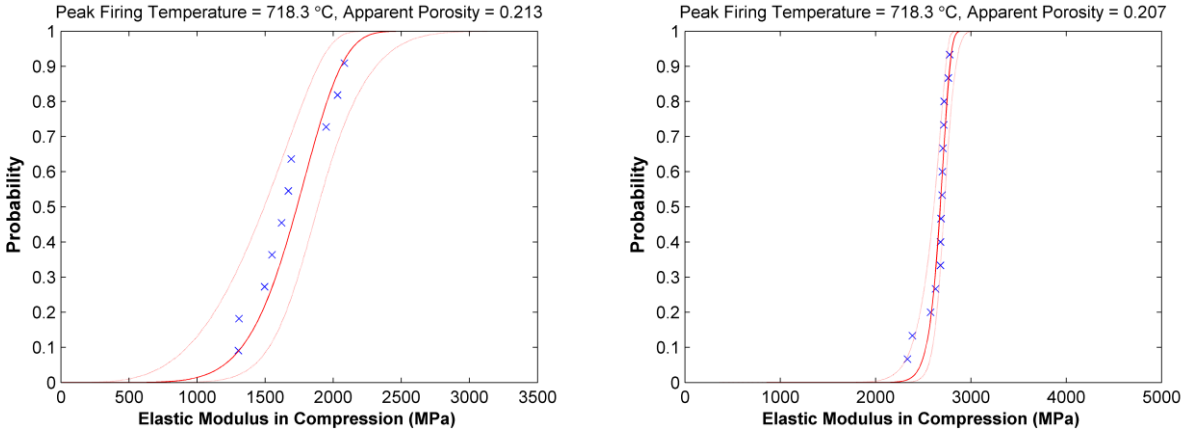

(a) (b)

Figure 5-37. Weibull CDF for elastic modulus in compression for specimens densified at 718.3°C: a) unpolished and b) polished.

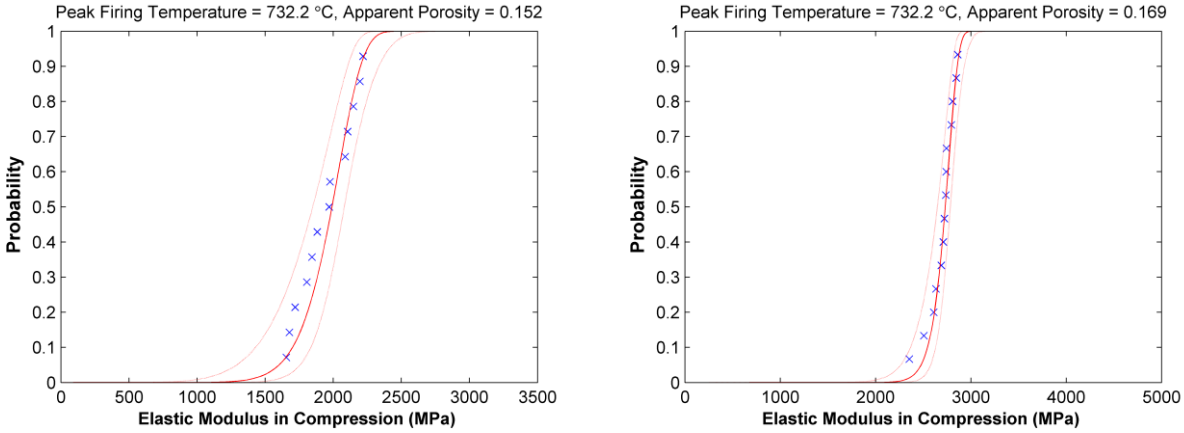

(a) (b)

Figure 5-38. Weibull CDF for elastic modulus in compression for specimens densified at 732.2°C: a) unpolished and b) polished.

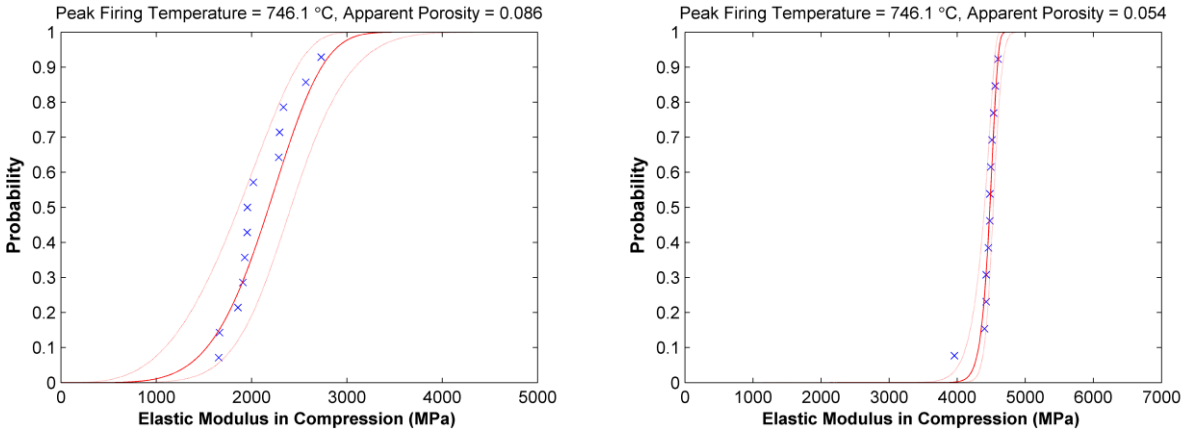

(a) (b)

Figure 5-39. Weibull CDF for elastic modulus in compression for specimens densified at 746.1°C: a) unpolished and b) polished.

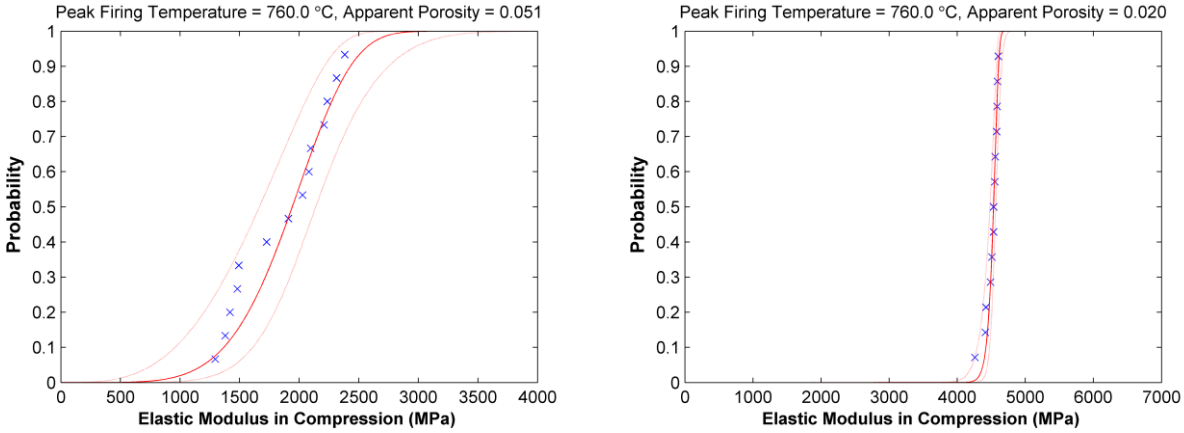

(a) (b)

Figure 5-40. Weibull CDF for elastic modulus in compression for specimens densified at 760°C: a) unpolished and b) polished.

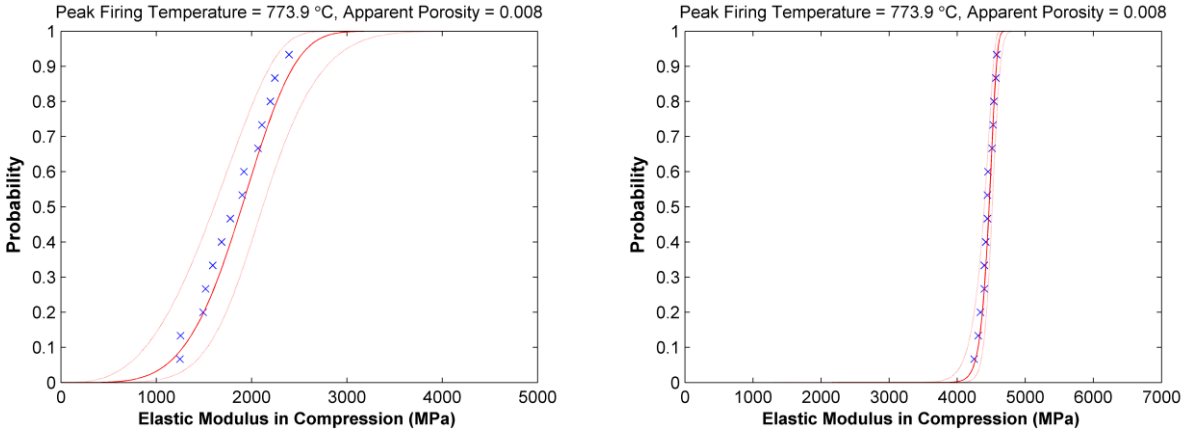

(a) (b)

Figure 5-41. Weibull CDF for elastic modulus in compression for specimens densified at 773.9°C: a) unpolished and b) polished.

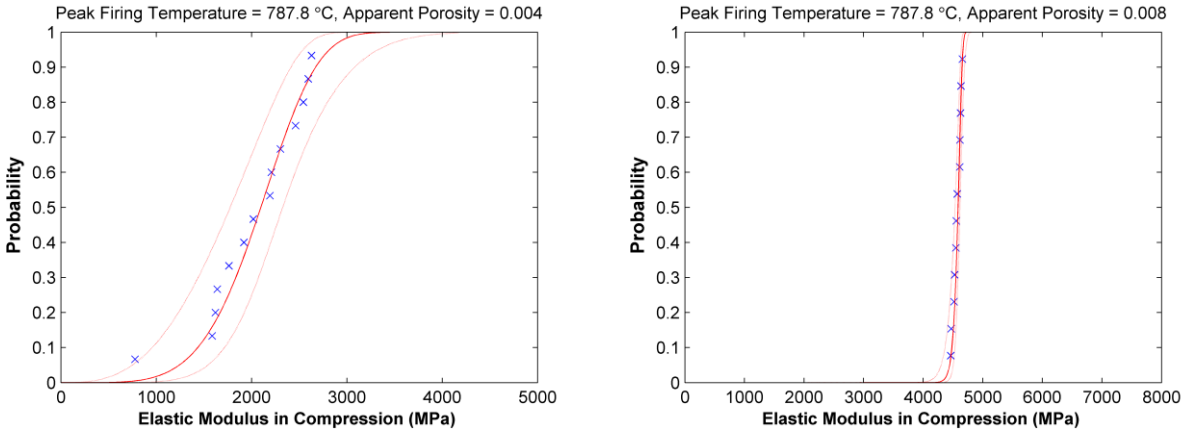

(a) **(b)**

5-Figure 5-42. Weibull CDF for elastic modulus in compression for specimens densified at 787.8°C: a) unpolished and b) polished.

The Weibull analysis for the elastic modulus in compression is compared graphically in Figures 5-43 & 5-44. In Figure 5-43, the mean value for the elastic modulus in compression is plotted against the mean porosity. In Figure 5-44, the Weibull modulus, or shape factor is plotted against mean apparent porosity.

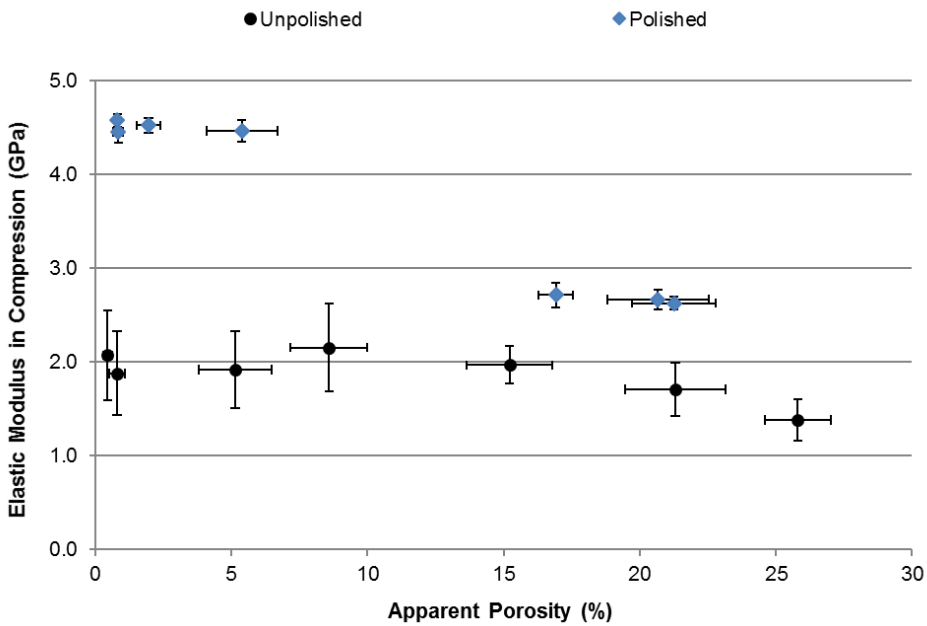

Figure 5-43. Mean value of the elastic modulus in compression as a function of porosity.

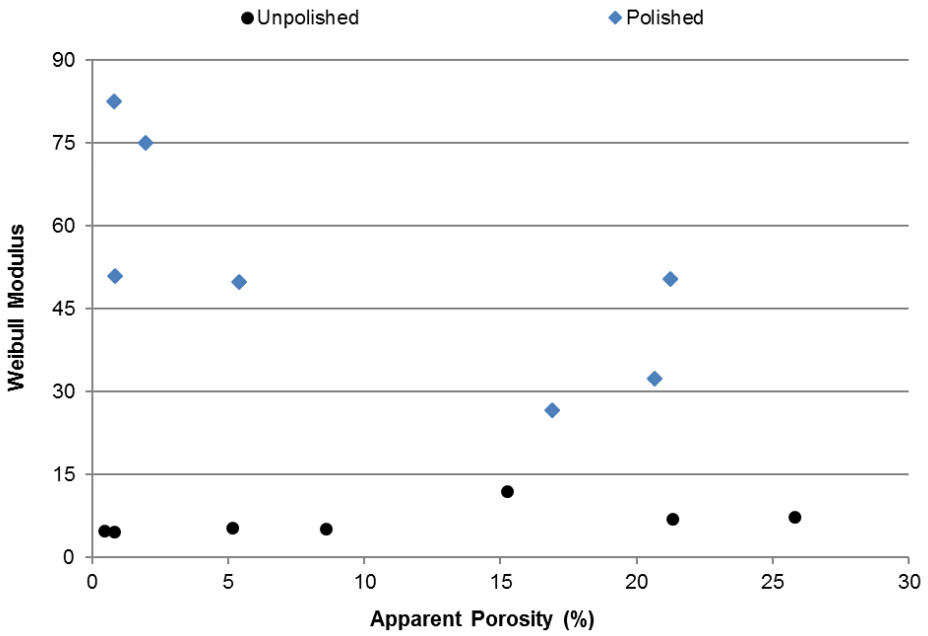

Figure 5-44. Graphical representation of the Weibull modulus for the elastic modulus in compression as a function of apparent porosity.

As expected, in both the unpolished and polished cases, the mean value of the elastic modulus can be observed to increase as apparent porosity decreases. However, that increase is much more pronounced in polished specimens. In addition, for polished specimens, elastic modulus values appeared to grouped for low and high porosity specimens. The size of the vertical error bars in Figure 5-43 also indicates that the elastic modulus data is less variable than the compressive strength data, particularly for polished specimens. In Figure 5-44, the only trend in the data that can be readily observed is that, in all cases, the values for the Weibull modulus are higher for polished specimens, as was the case with data obtained through compressive testing.

5.4.3. FLEXURAL BEHAVIOR

5.4.3.1. Stress-Strain Behavior Under Transverse Loading: The stress-strain behavior of all transverse specimens can be seen on the next few pages in Figures 5-45 through 5-51. Stress-strain data is grouped in batches and is shown in order of ascending densification temperature, which was between 705 and 790°C.

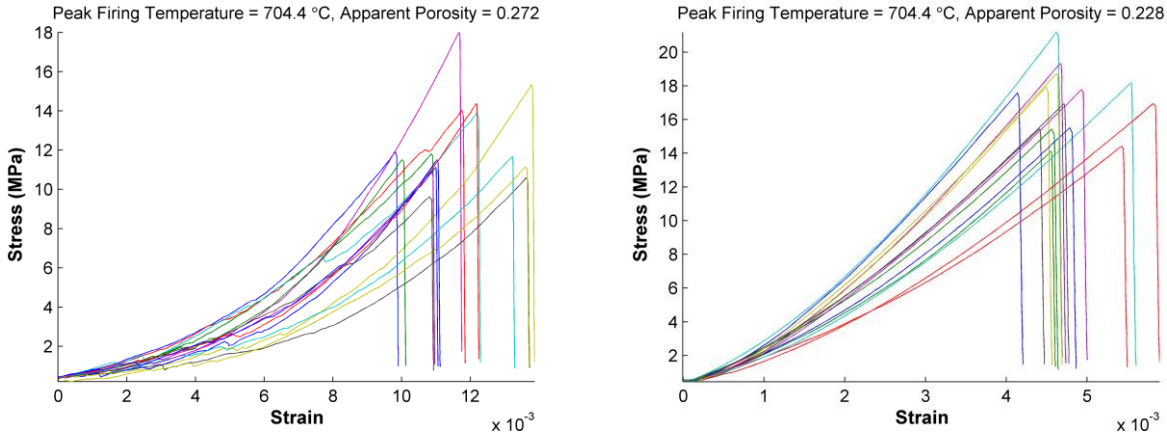

(a) (b)

Figure 5-45. Stress-strain curves for transversely loaded specimens densified at 704.4°C: a) unpolished and b) polished.

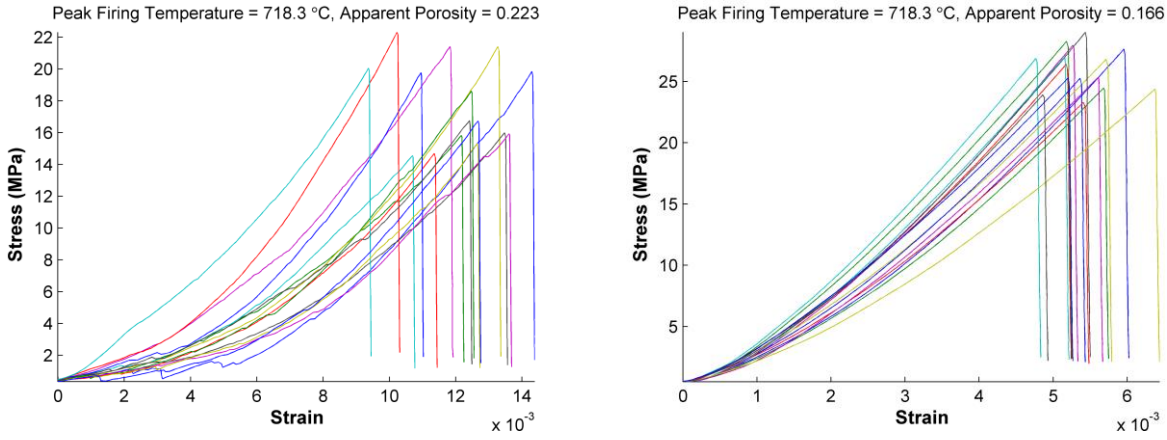

(a) (b)

Figure 5-46. Stress-strain curves for transversely loaded specimens densified at 718.3°C: a) unpolished and b) polished.

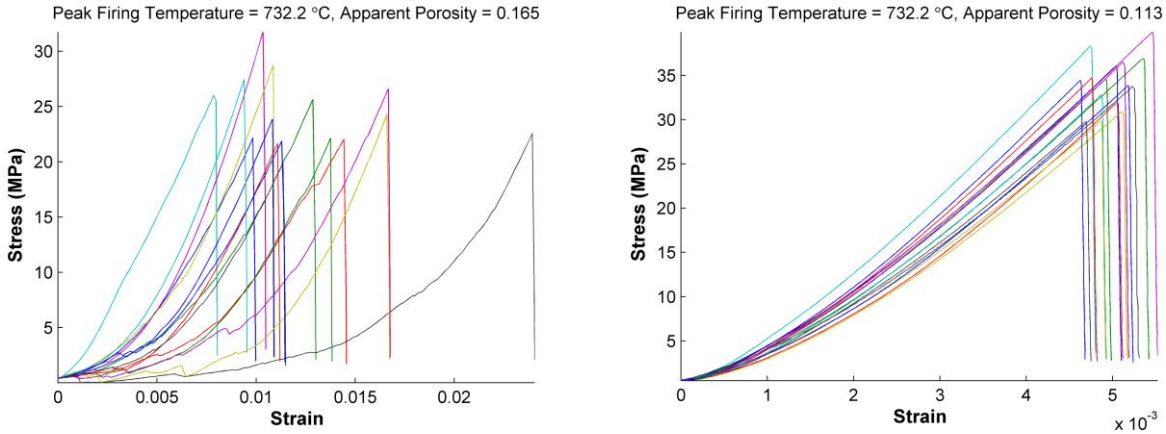

(a) (b)

Figure 5-47. Stress-strain curves for transversely loaded specimens densified at 732.2°C: a) unpolished and b) polished.

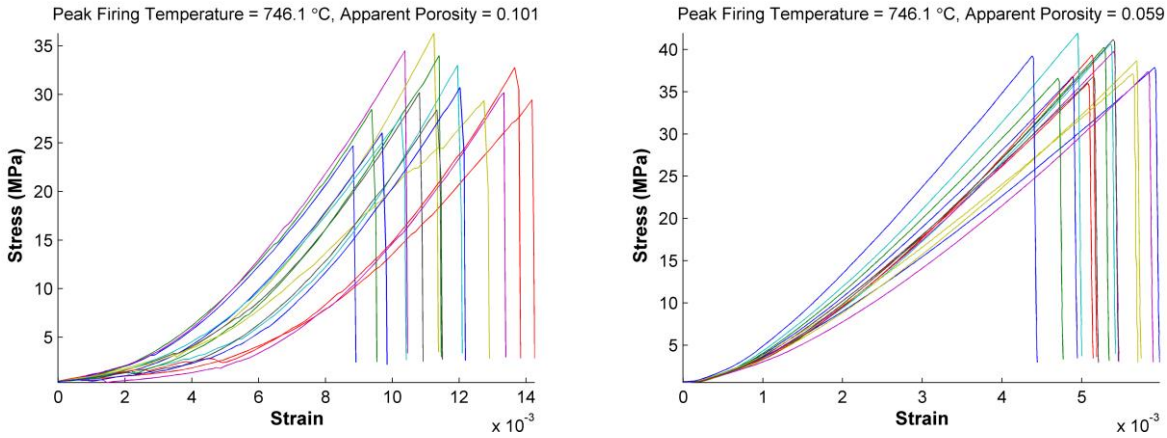

(a) (b)

Figure 5-48. Stress-strain curves for transversely loaded specimens densified at 746.1°C: a) unpolished and b) polished.

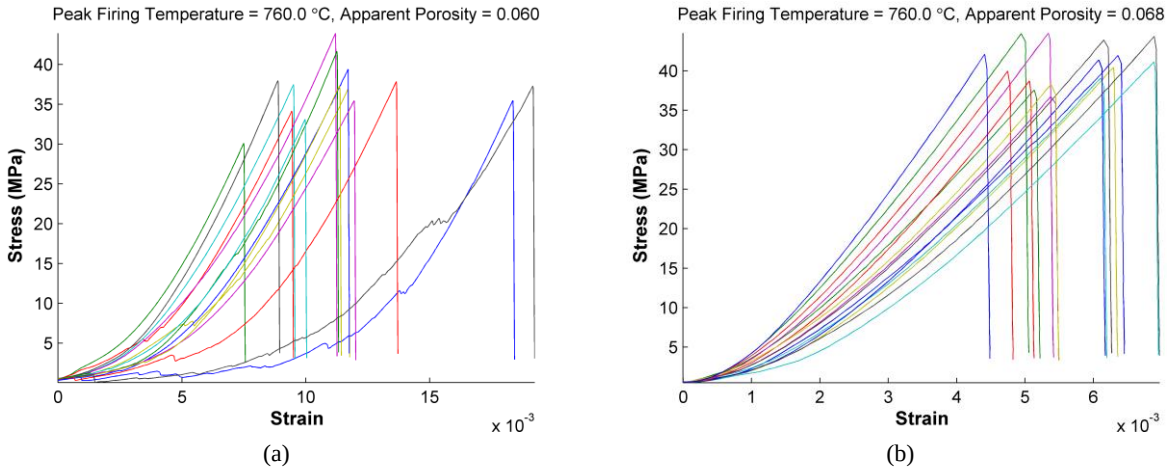

(a) (b)

Figure 5-49. Stress-strain curves for transversely loaded specimens densified at 760°C: a) unpolished and b) polished.

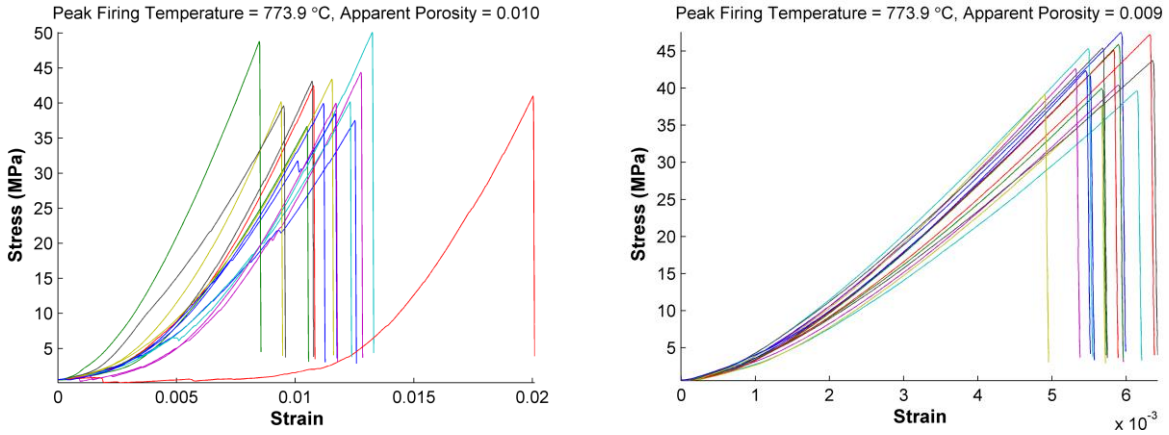

(a) (b)

Figure 5-50. Stress-strain curves for transversely loaded specimens densified at 773.9°C: a) unpolished and b) polished.

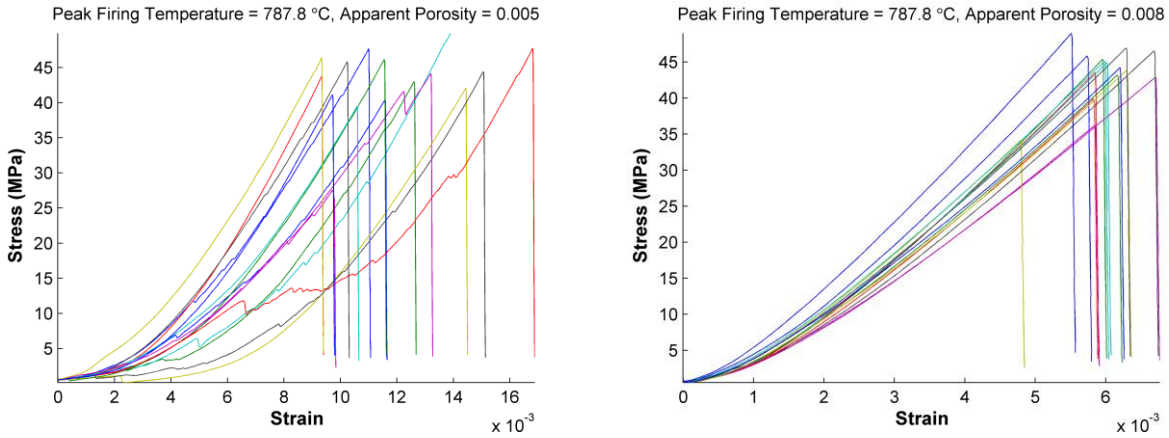

(a) (b)

Figure 5-51. Stress-strain curves for transversely loaded specimens densified at 787.8°C: a) unpolished and b) polished.

As expected, the flexural specimens exhibited behavior consistent with porous, brittle materials and did not undergo plastic deformation. Catastrophic failure occurred at the point when maximum stress was achieved. Unlike the compressive testing, stress-strain behavior, with the exception of maximum stress, was relatively consistent across the entire range of apparent porosity present. As was the case with the compressive data, the data associated with polished specimens is very well behaved when compared to the data associated with the unpolished specimens.

5.4.3.2. Elastic Modulus Under Transverse Loading: Before further analysis, the stress-strain data was truncated as described in Section 4.2.2. These calculations were performed in MATLAB (Appendix B). The linear portion of the stress-strain curves can be seen in Figures 5-52 through 5-58.

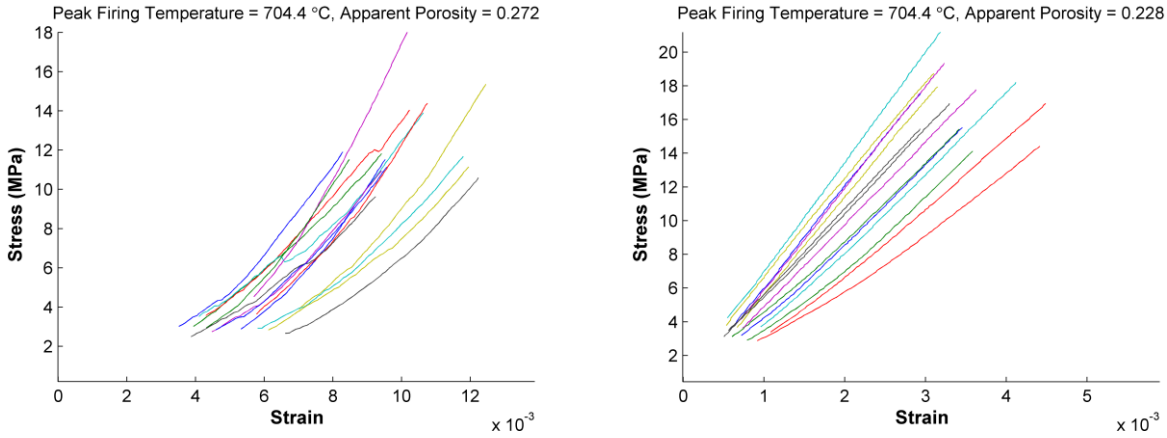

(a) (b)

Figure 5-52. Truncated stress-strain curves for transversely loaded specimens densified at 704.4°C: a) unpolished and b) polished.

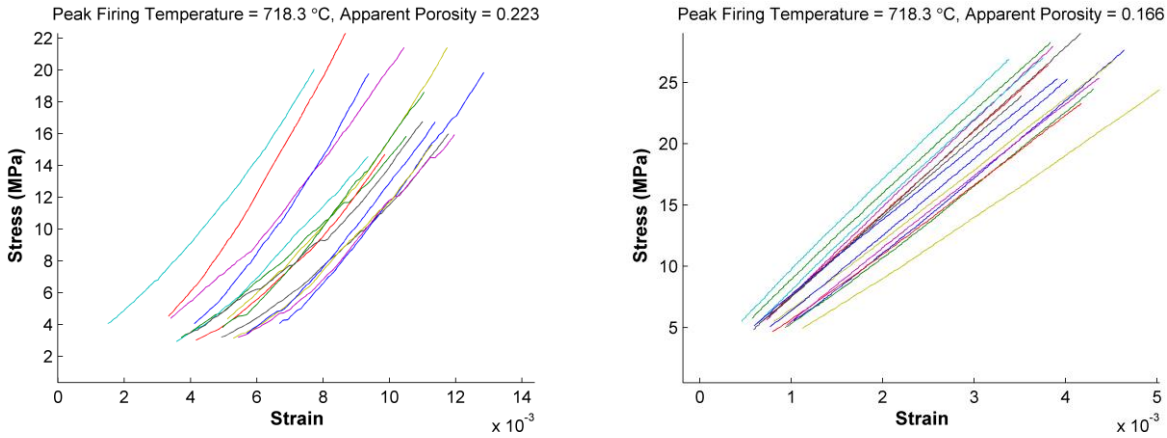

(a) (b)

Figure 5-53. Truncated stress-strain curves for transversely loaded specimens densified at 718.3°C: a) unpolished and b) polished.

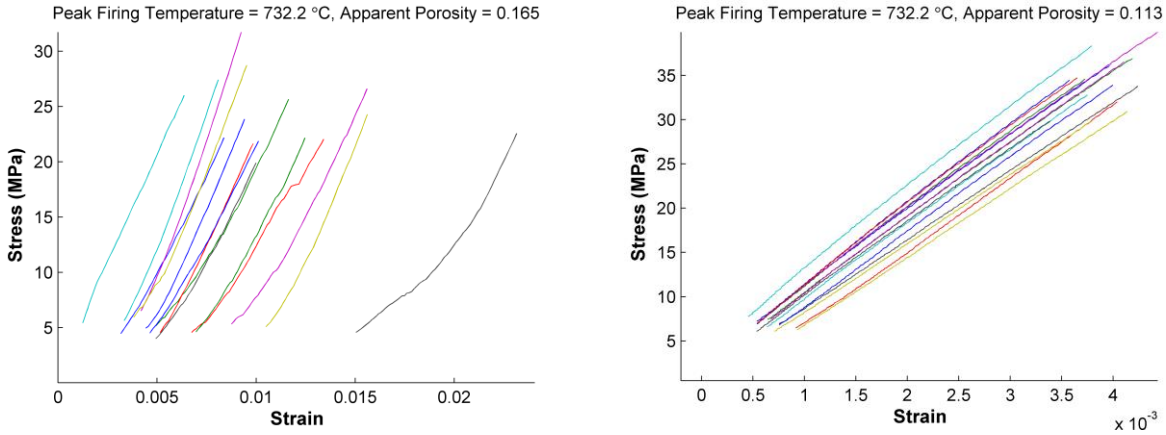

(a) (b)

Figure 5-54. Truncated stress-strain curves for transversely loaded specimens densified at 732.2°C: a) unpolished and b) polished.

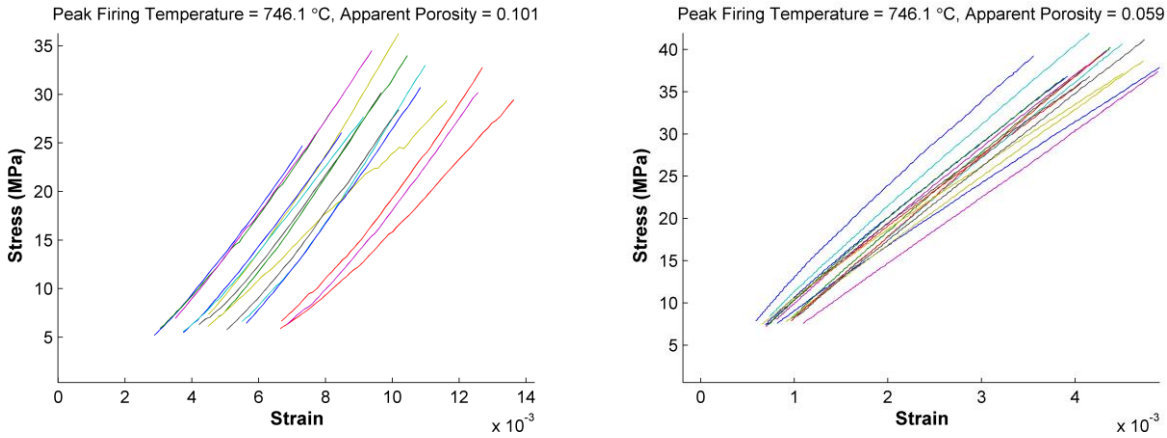

(a) (b)

Figure 5-55. Truncated stress-strain curves for transversely loaded specimens densified at 746.1°C: a) unpolished and b) polished.

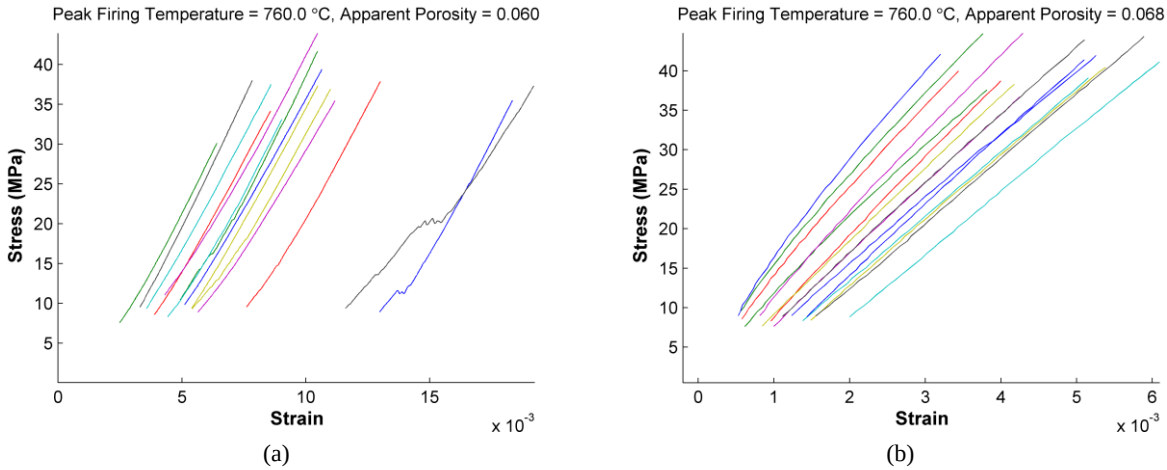

(a) (b)

Figure 5-56. Truncated stress-strain curves for transversely loaded specimens densified at 760°C: a) unpolished and b) polished.

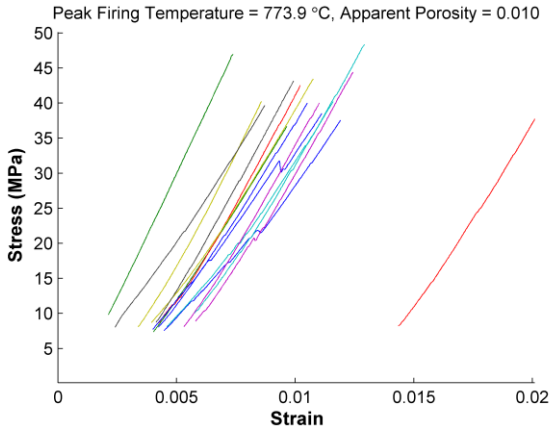

(a)

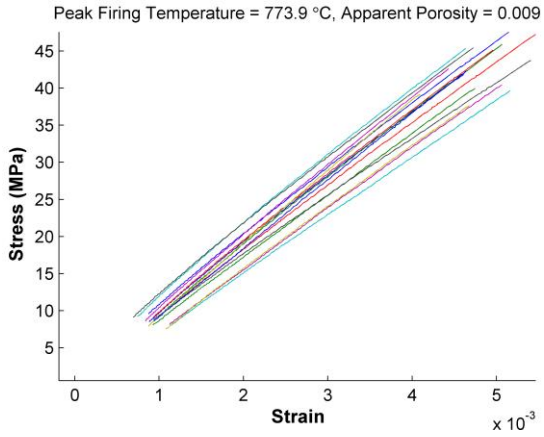

(b)

Figure 5-57. Truncated stress-strain curves for transversely loaded specimens densified at 773.9°C: a) unpolished and b) polished.

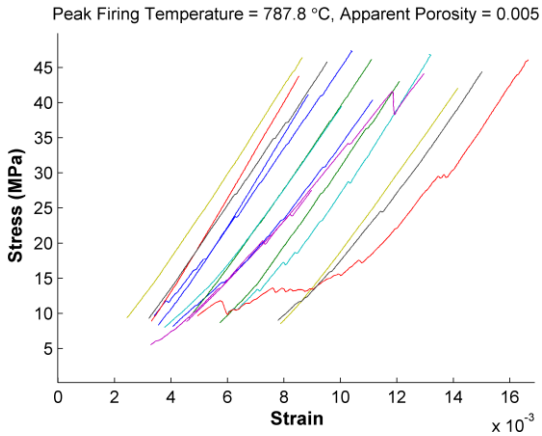

(a)

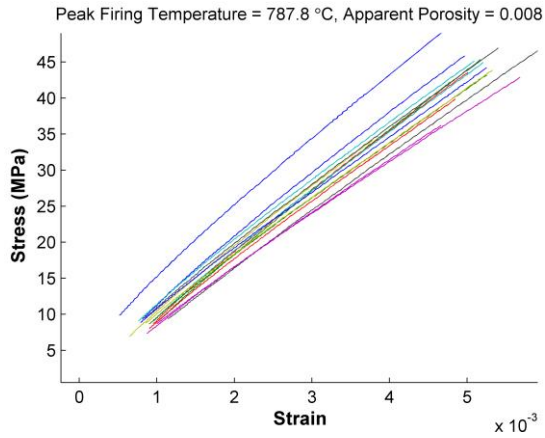

(b)

Figure 5-58. Truncated stress-strain curves for transversely loaded specimens densified at 787.8°C: a) unpolished and b) polished.

The behavior observed within the elastic region of the stress-strain curves is more similar for unpolished versus polished specimens subjected to transverse loading. The elastic portion of flexural stress-strain curves can be characterized by being generally linear, particularly as apparent porosity decreases. However, in almost all cases, the curves generated from unpolished specimens also show discontinuities and load drops, as was the case with the data obtained through compressive testing. For the polished specimens, once the initial non-linearity is omitted from the data, the elastic portion of the curves is quite well behaved throughout the range of peak densification temperature. Discontinuities and load drops are not present and the curves can be

characterized by linear behavior. However, within any given batch of polished specimens, the slopes of the curves are a bit more dissimilar.

5.4.3.3. Weibull Analysis for Transverse Strength: After flexural testing, the data was analyzed using the Weibull method. The results of the analysis for transverse rupture strength are summarized in Table 5-5 & 5-6, and Weibull probability plots are shown in Appendix C.

Table 5-5. Summary of results for Weibull analysis of transverse strength data (unpolished specimens).

Apparent Porosity	Mean (MPa)	Std. Dev. (MPa)	Scale Factor (MPa)	Modulus
27.1977	12.4227	2.5500	13.4375	5.6357
22.2905	17.9418	2.7707	19.0919	7.6643
16.5186	24.3143	3.7129	25.8574	7.7569
10.1077	30.2010	3.6041	31.7338	10.0864
6.0193	36.8787	3.8328	38.5244	11.6709
1.0256	41.5249	4.7008	43.5320	10.6650
0.5436	43.4192	4.2296	45.2422	12.4926

Table 5-6. Summary of results for Weibull analysis of transverse strength data (polished specimens).

Apparent Porosity	Mean (MPa)	Std. Dev. (MPa)	Scale Factor (MPa)	Modulus
22.8221	17.0547	2.1837	17.9781	9.3608
16.5621	26.1154	1.8345	26.9178	17.5688
11.3108	34.2226	3.2449	35.6233	12.8517
5.8603	38.5929	2.0956	39.5165	22.9215
6.7729	40.9680	2.8197	42.2022	17.9443
0.8730	42.9344	3.2167	44.3380	16.4318
0.7689	43.5388	3.4260	45.0308	15.6147

The tabulated data shows that for unpolished specimens, the mean transverse strength ranges from 12.42 to 43.42 MPa and values for the Weibull modulus vary from 5.64 to 12.49. For polished specimens, the values for strength are comparable and the values for the Weibull Modulus are noticeably higher; transverse strength varies from 17.05 to 43.54 MPa and the Weibull modulus varies between 9.36 and 22.92.

Once the data was analyzed through the Weibull approach, the cumulative distribution function for each of the seven batches of compressive specimens was calculated. The CDF plots are shown in Figures 5-59 through 5-65. In each of the figures, the experimental data is denoted by blue x's, the Weibull CDF is denoted by the solid red line and the 95% upper and lower confidence bounds are denoted by the dashed red lines.

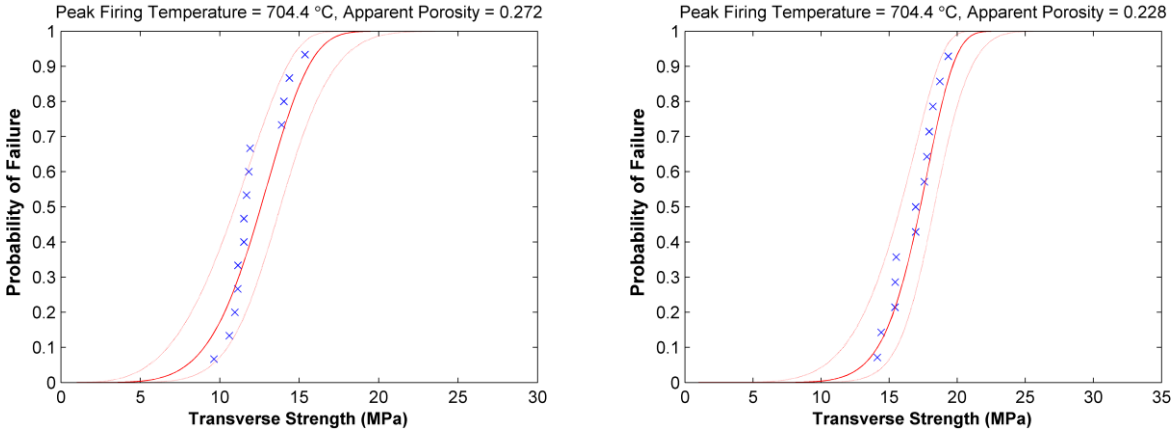

(a) (b)

Figure 5-59. Weibull CDF for transverse strength for specimens densified at 704.4°C: a) unpolished and b) polished.

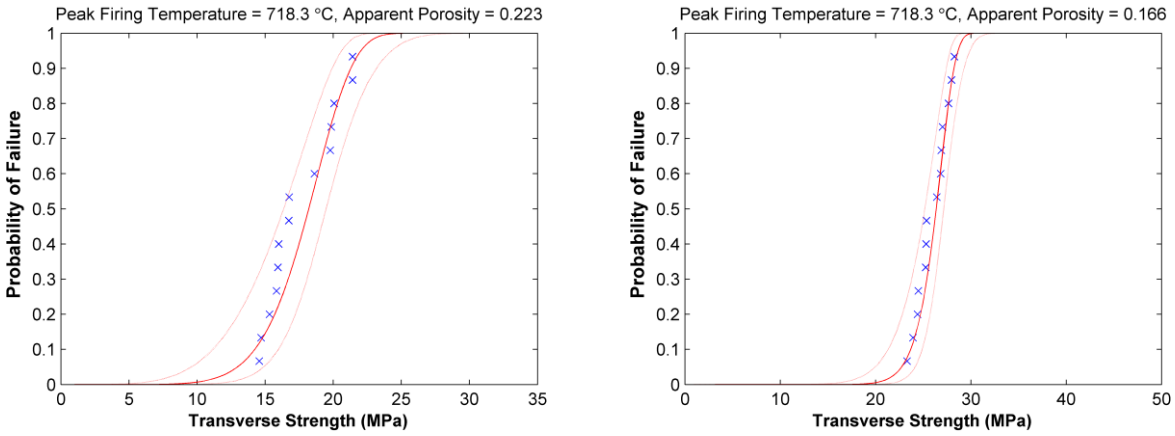

(a) (b)

Figure 5-60. Weibull CDF for transverse strength for specimens densified at 718.3°C: a) unpolished and b) polished.

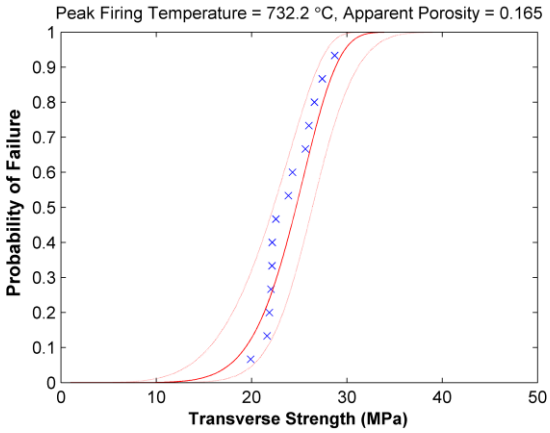

(a)

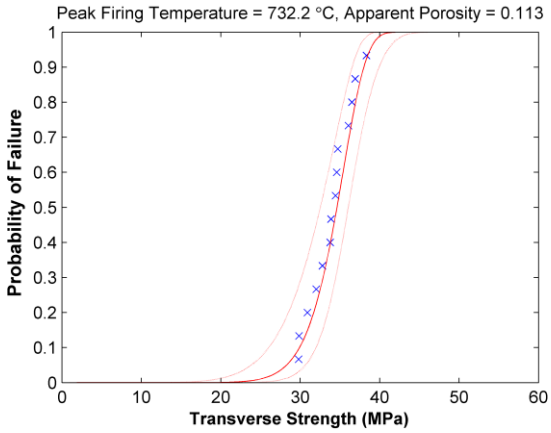

(b)

Figure 5-61. Weibull CDF for transverse strength for specimens densified at 732.2°C: a) unpolished and b) polished.

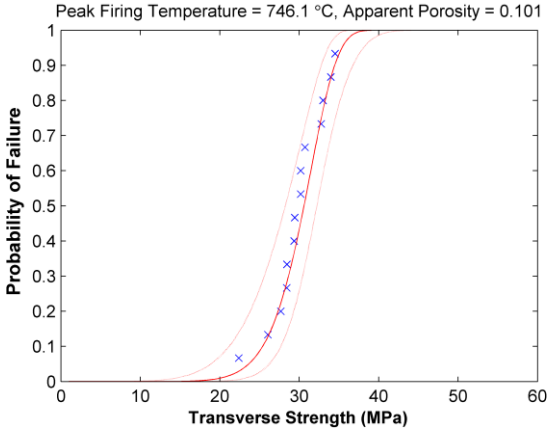

(a)

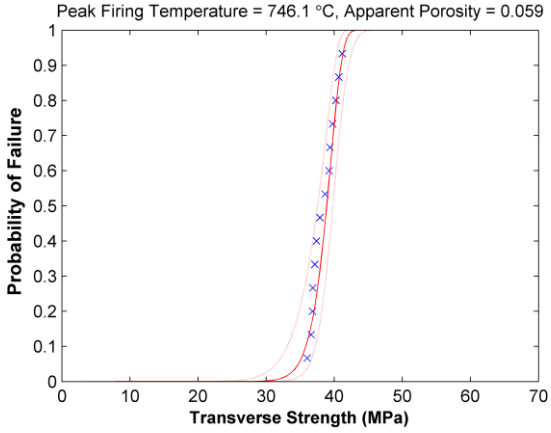

(b)

Figure 5-62. Weibull CDF for transverse strength for specimens densified at 746.1°C: a) unpolished and b) polished.

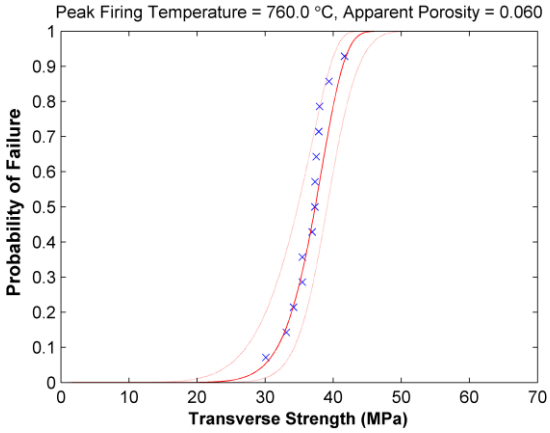

(a)

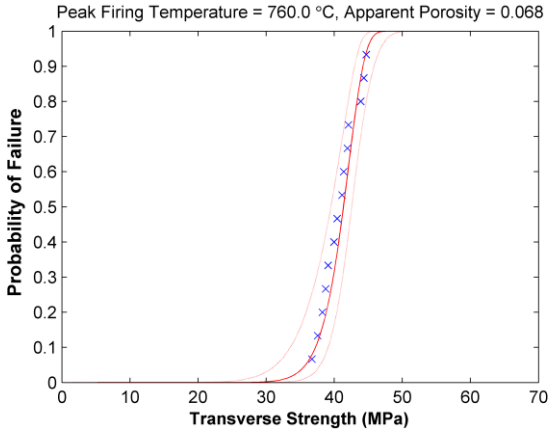

(b)

Figure 5-63. Weibull CDF for transverse strength for specimens densified at 760°C: a) unpolished and b) polished.

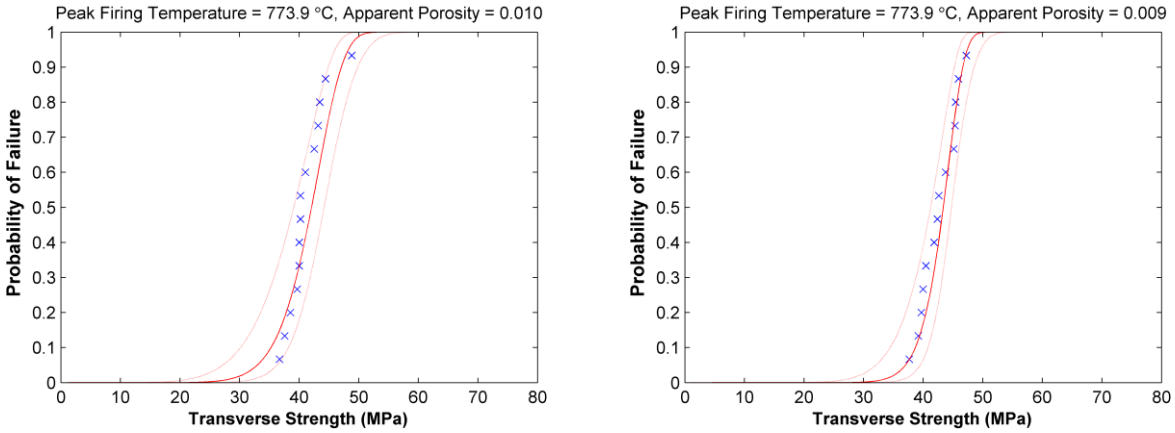

(a) (b)

Figure 5-64. Weibull CDF for transverse strength for specimens densified at 773.9°C: a) unpolished and b) polished.

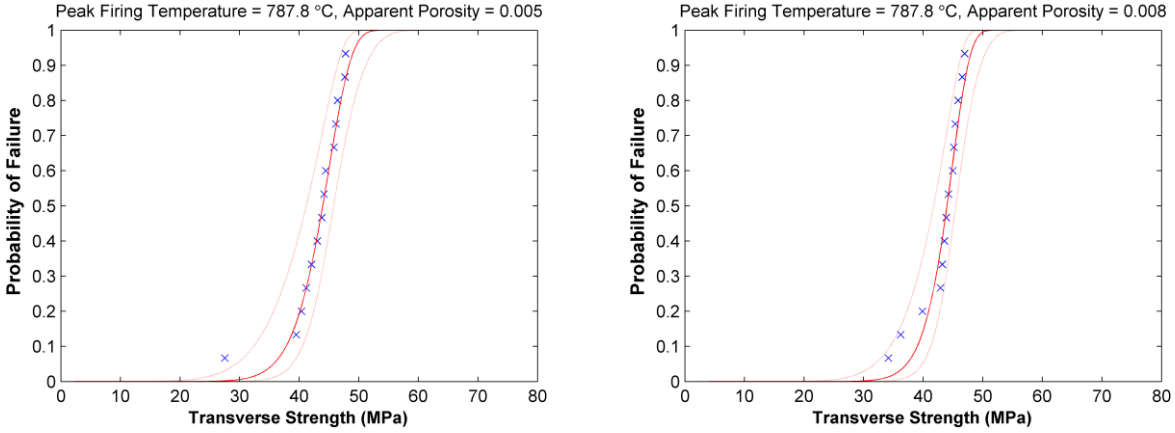

(a) **(b)**

Figure 5-65. Weibull CDF for transverse strength for specimens densified at 787.8°C: a) unpolished and b) polished.

The Weibull analysis data for each batch of transversely loaded specimens is shown graphically in Figures 5-66 & 5-67. In Figure 5-66, the mean transverse strength is plotted against the mean porosity. In Figure 5-67, the Weibull modulus, or shape factor is plotted against mean apparent porosity.

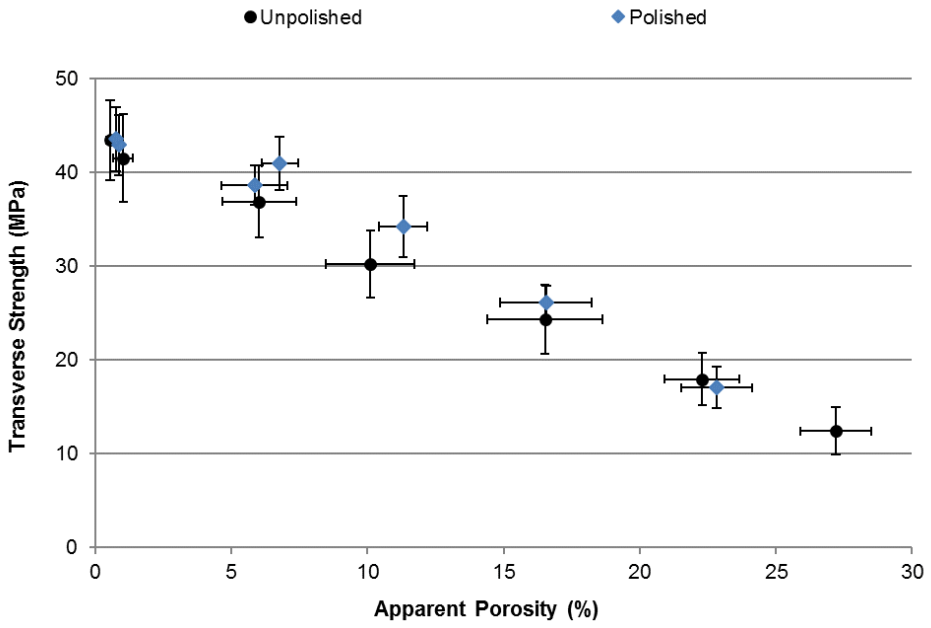

Figure 5-66. Mean flexural strength as a function of porosity.

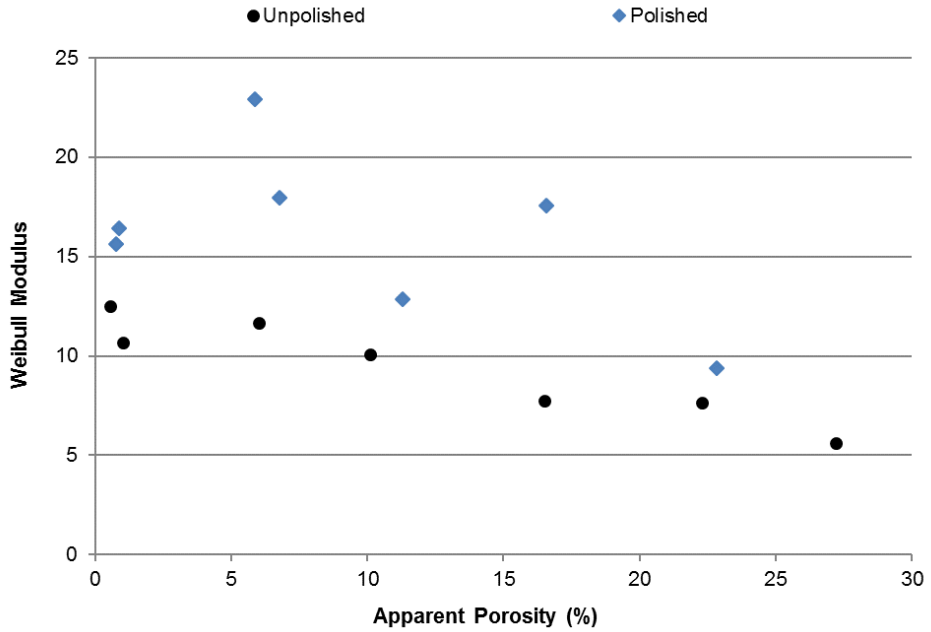

Figure 5-67. Graphical representation of the Weibull Modulus for transverse strength as a function of apparent porosity.

As expected, the mean transverse strength can be observed to increase as apparent porosity decreases. Although the mean values for transverse strength are generally higher for polished rather than unpolished specimens, this difference in strength is much less pronounced

than was observed for compressively loaded specimens (Figure 5-34). As with the compressive data, the standard deviation in strength is larger at lower porosity; however, this behavior is also not as pronounced. In addition, unlike the observations made from the compressive testing data, when comparing the data obtained from only polished or unpolished, specimens do not exhibit similar strength when the apparent porosity is ~10% or less. In Figure 5-67, no trend in the data can be readily observed. Again, in all cases the Weibull modulus for the transverse strength data is higher for polished specimens.

5.4.3.4. Weibull Analysis for Elastic Modulus Under Transverse Loading: A summary of the Weibull analysis for the elastic modulus in flexure is shown in Tables 5-7 & 5-8, and Weibull probability plots are shown in Appendix C.

Table 5-7. Summary of Weibull data for elastic modulus in flexure (unpolished specimens).

Apparent Porosity	Mean (GPa)	Std. Dev. (GPa)	Scale Factor (GPa)	Modulus
27.1977	1.8453	0.5087	2.0336	4.0778
22.2905	2.3838	0.4965	2.5809	5.5474
16.5186	3.5393	0.7612	3.8396	5.3562
10.1077	4.3929	0.4440	4.5839	12.0195
6.0193	5.3443	0.5486	5.5800	11.8244
1.0256	5.3477	0.8639	5.7043	7.3026
0.5436	5.2428	0.8671	5.5997	7.1197

Table 5-8. Summary of Weibull data for elastic modulus in flexure (polished specimens).

Apparent Porosity	Mean (GPa)	Std. Dev. (GPa)	Scale Factor (GPa)	Modulus
22.8221	5.0231	0.8956	5.3879	6.5657
16.5621	6.3153	0.6357	6.5888	12.07042
11.3108	8.3974	0.4777	8.6077	21.84653
5.8603	8.7821	0.9097	9.1728	11.7110
6.7729	9.2661	1.4502	9.8671	7.5553
0.8730	8.7306	0.6088	8.9970	17.7035
0.7689	8.1508	0.6370	8.4283	15.7254

The tabulated data shows that, for unpolished specimens, the mean values for the elastic modulus in flexure range from 1.84 to 5.35 GPa and values for the Weibull modulus vary from 4.08 to 12.02. For polished specimens, the values for the elastic modulus are approximately twice as high and the values for the Weibull Modulus are also noticeably higher; the elastic modulus varies from 5.02 to 9.27 GPa and the Weibull modulus varies between 6.57 and 21.85.

Once the data was analyzed through the Weibull approach, the cumulative distribution function for each of the seven batches of compressive specimens was calculated. The CDF plots are shown in Figures 5-68 through 5-74. In each of the figures, the experimental data is denoted by blue x's, the Weibull CDF is denoted by the solid red line and the 95% upper and lower confidence bounds are denoted by the dashed red lines.

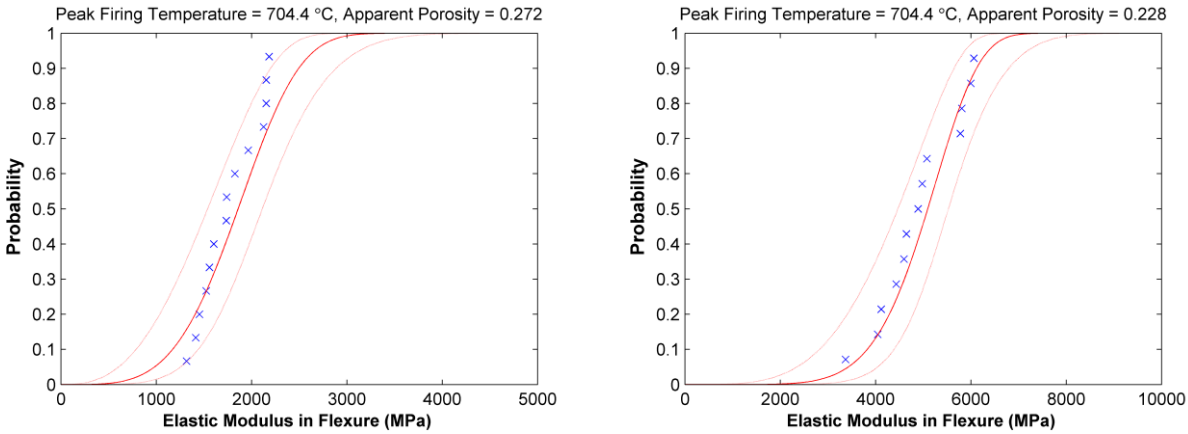

(a) (b)

Figure 5-68. Weibull CDF for elastic modulus in flexure for specimens densified at 704.4°C: a) unpolished and b) polished.

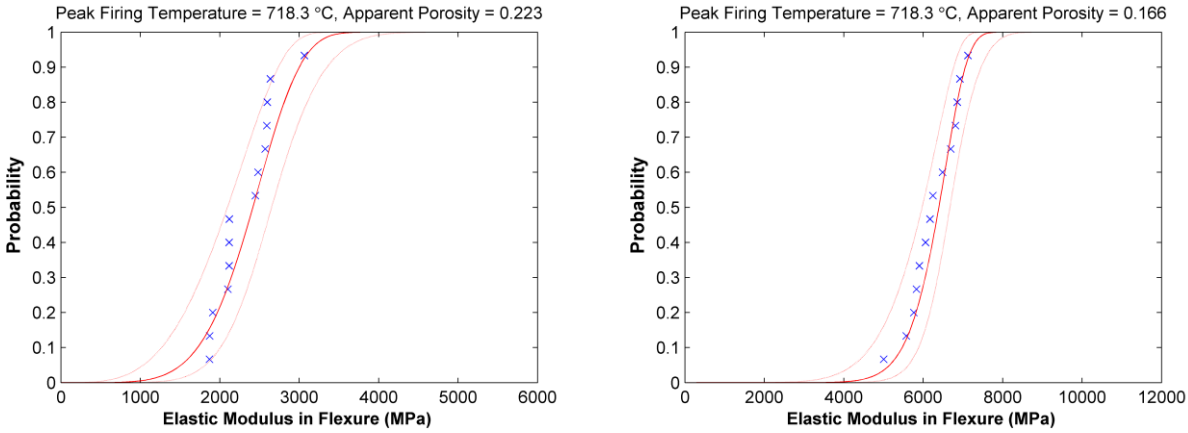

(a) (b)

Figure 5-69. Weibull CDF for elastic modulus in flexure for specimens densified at 718.3°C: a) unpolished and b) polished.

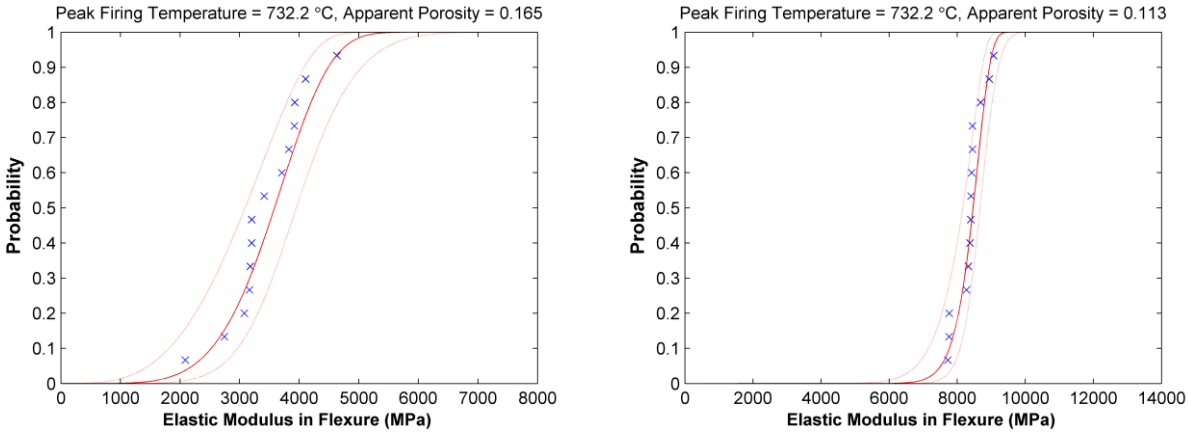

(a) (b)

Figure 5-70. Weibull CDF for elastic modulus in flexure for specimens densified at 732.2°C: a) unpolished and b) polished.

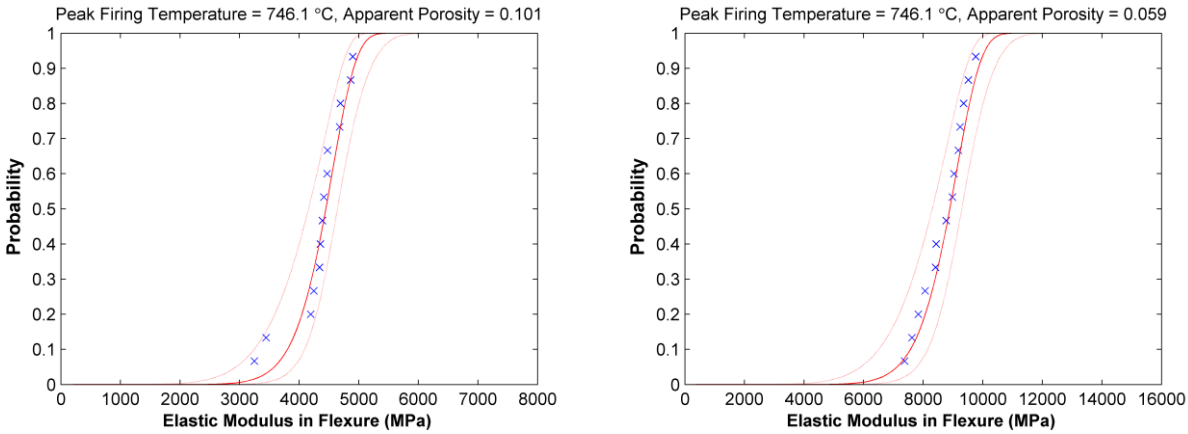

(a) (b)

Figure 5-71. Weibull CDF for elastic modulus in flexure for specimens densified at 746.1°C: a) unpolished and b) polished.

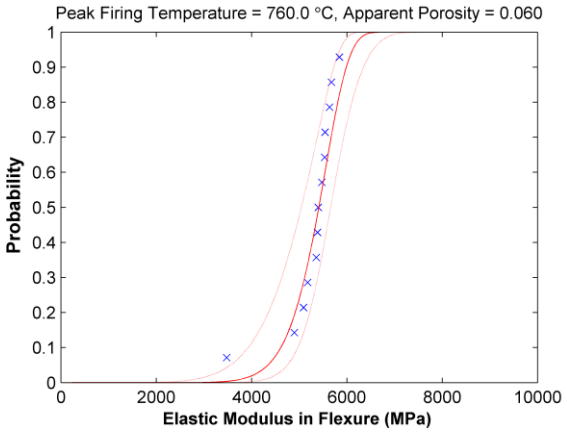

(a)

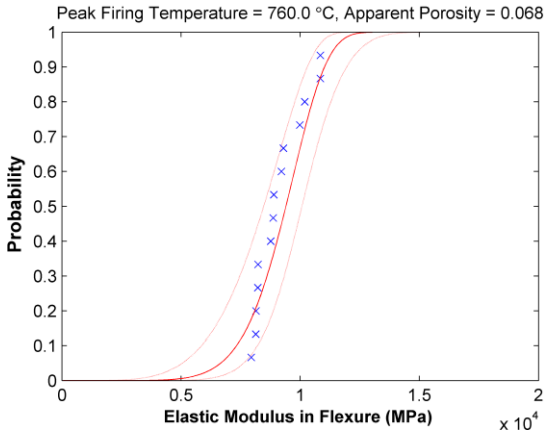

(b)

Figure 5-72. Weibull CDF for elastic modulus in flexure for specimens densified at 760°C: a) unpolished and b) polished.

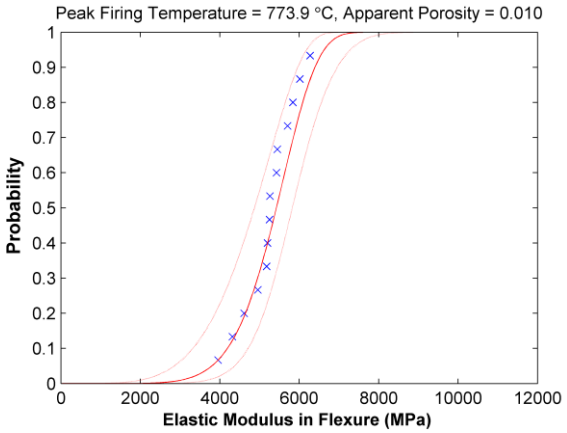

(a)

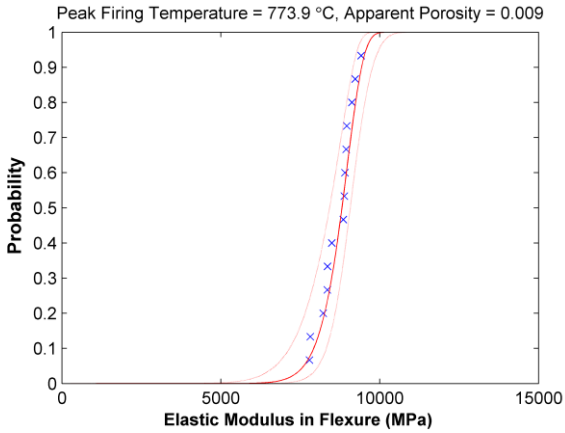

(b)

Figure 5-73. Weibull CDF for elastic modulus in flexure for specimens densified at 773.9°C: a) unpolished and b) polished.

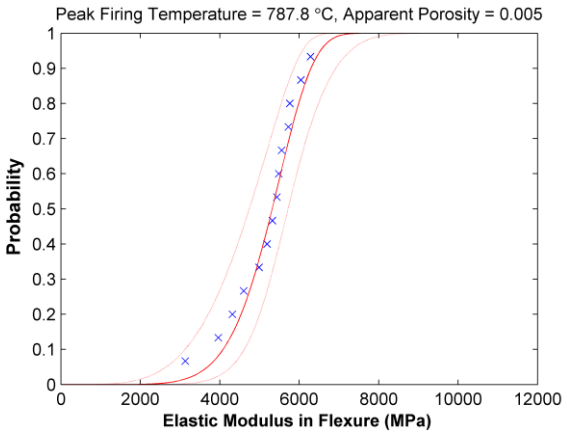

(a)

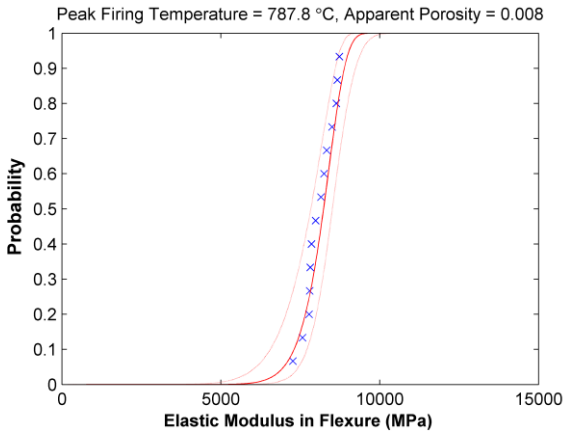

(b)

Figure 5-74. Weibull CDF for elastic modulus in flexure for specimens densified at 787.8°C: a) unpolished and b) polished.

A comparison of the results of the Weibull analysis for the elastic modulus in flexure is shown graphically in Figures 5-75 & 5-76. In Figure 5-75, the mean value for the elastic modulus in flexure is plotted against the porosity. In Figure 5-76, the Weibull modulus, or shape factor is plotted against mean apparent porosity.

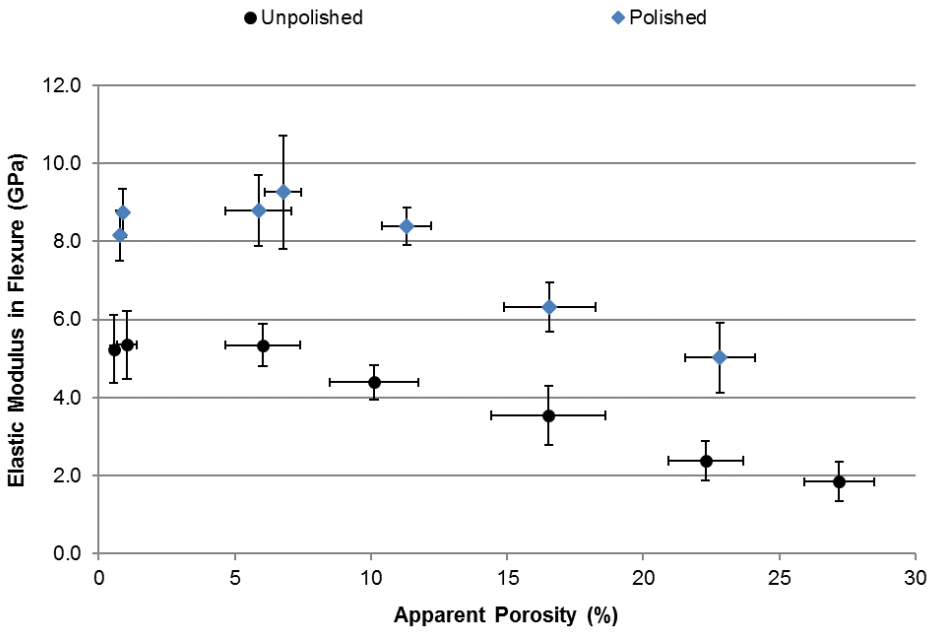

Figure 5-75. Mean value of the elastic modulus in flexure as a function of porosity.

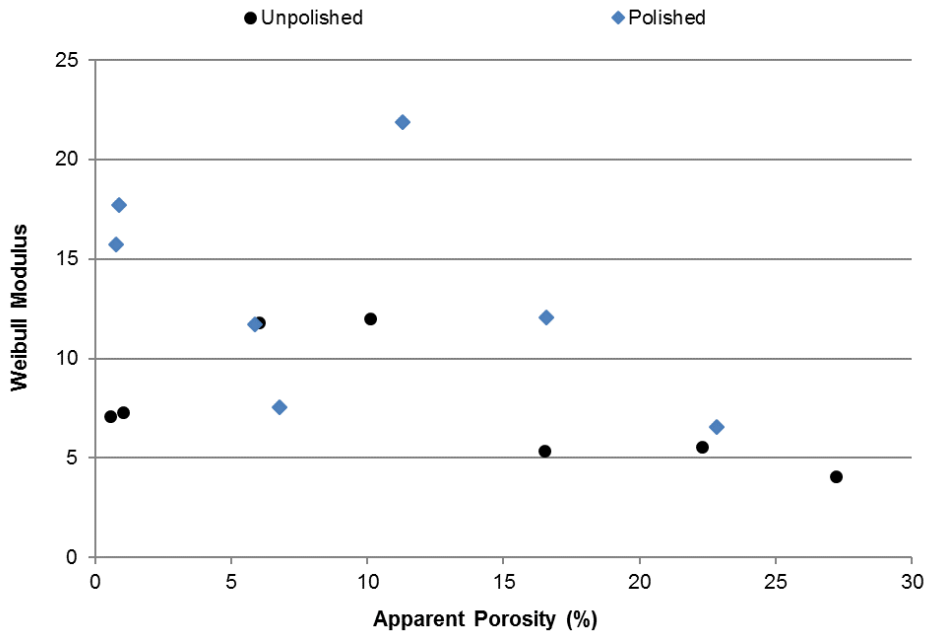

Figure 5-76. Graphical representation of the Weibull Modulus for the elastic modulus in flexure as a function of apparent porosity.

As expected, the mean value of the elastic modulus can be observed to increase as apparent porosity decreases. For unpolished specimens, this difference appears to be more pronounced than was observed in the analysis of the compressive testing data (Figure 5-43). In Figure 5-76, the values of Weibull modulus are scattered between ~4 and ~22, with no observable trends, except that values for polished specimens are again generally higher than values for unpolished specimens. In Figures 5-77 & 5-78, the elastic modulus in flexure is compared to the elastic modulus in compression for both unpolished and polished specimens.

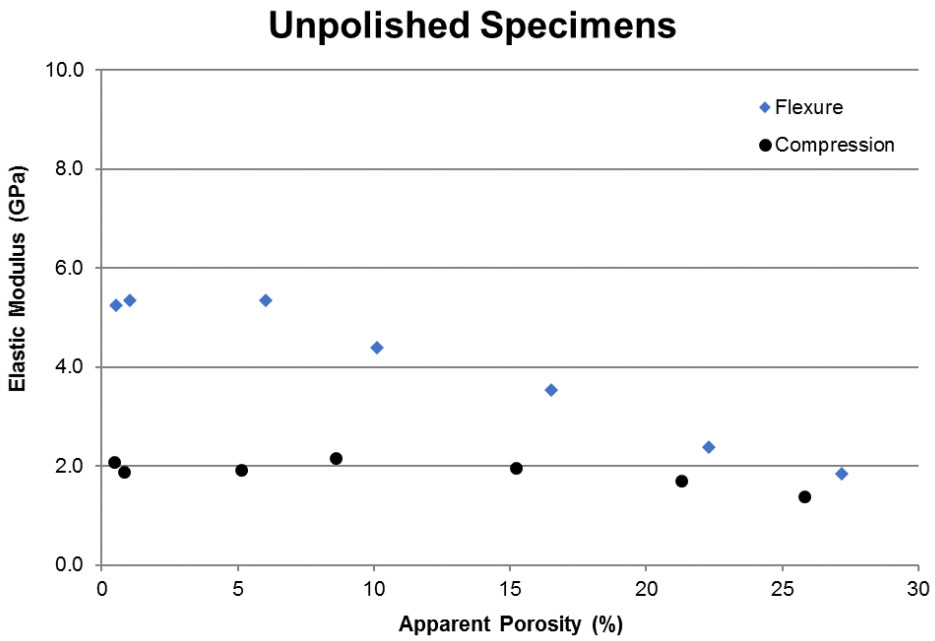

Figure 5-77. Comparison of calculated values for the elastic modulus in compression and flexure (unpolished specimens).

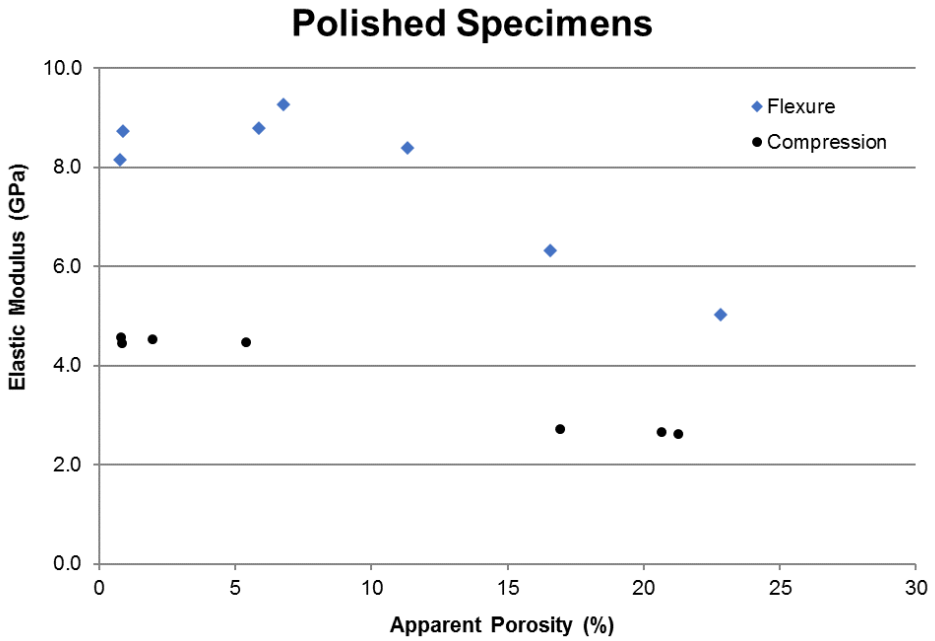

Figure 5-78. Comparison of calculated values for the elastic modulus in compression and flexure (polished specimens).

In both cases, the calculated values follow the same general trend, where the elastic modulus increases with decreasing apparent porosity under compressive and flexural loading.

However, the calculations made from the flexural testing data yielded much higher values compared to the calculations made from the compressive data.

5.5 Comparison to Porosity-Property Models

The data presented in Sections 5.1 through 5.4 indicates that many of the discrepancies in the previous studies of this material[4] could be attributed to variations in specimen geometry. Therefore, the comparison of experimental data to established models that have been used to predict the mechanical properties based on the porosity has been limited to data collected from polished specimens.

5.5.1. Compressive Behavior

5.5.1.1. Compressive Strength: In comparing the experimental results to the published zero porosity compressive strength, an average value was used (Table 2-1). The data was then fit using four approaches. First an exponential relationship was used as was the case in Duckworth's[38] investigation of the relationship between porosity and strength (Equation 2.8). Then the data was fit using the three models for cellular materials proposed by Gibson and Ashby (Equations 2.9-2.11) [14].

In fitting the data using Gibson and Ashby's models, the lower bounds on a and b were set at a value of zero, while φ was allowed to vary between zero and one, where a value of one correlates to open cells and a value of zero correlates to a fully dense material. Calculations were performed in MATLAB and the code is shown in Appendix B. The results are summarized in Table 5-9.

Table 5-9. Summary of curve fitting results for compressive strength, including regression analysis.

Fit Type	Value of Fitting Parameters			R^2	RMSE (MPa)
	a	b	φ		
Duckworth	275.5	--	--	0.9671	149
Gibson-Ashby: Open	0.2917	--	--	0.1532	755
Gibson-Ashby: Open	0.1554	--	--	0.1813	742
Gibson-Ashby: Closed	0.5616	.000082	0.6461	0.1532	893

The data shows that all three of Gibson and Ashby's correlations fit the data quite poorly. These models were developed for highly ordered materials with defined pore geometry, while the material under investigation may be comprised of pores with varying pore geometry and size. By comparison, Duckworth's exponential correlation between strength and porosity appears to fit reasonably well. The exponential fit can be seen graphically in Figure 5-79, where the experimental data is represented by blue dots, the fitted model is represented by the solid red line and the upper and lower 95% confidence bounds are represented by the dashed red lines. It should be noted that, Duckworth's model appears to fit the data from previous study, which used unpolished specimens exhibiting >7% porosity, much more closely[4].

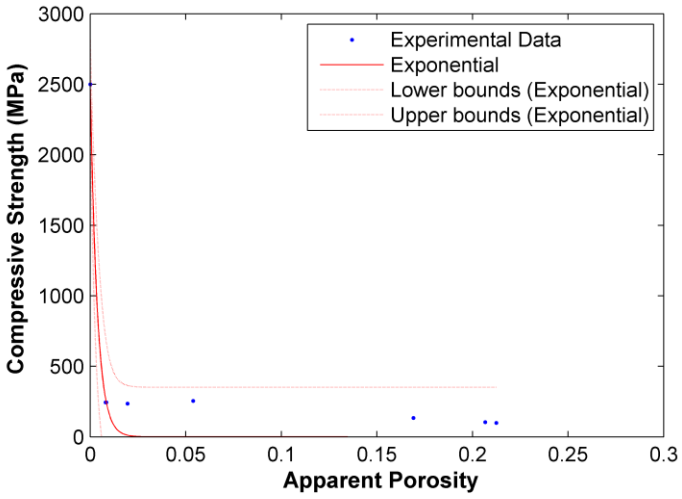

Figure 5-79. Experimental and published zero porosity data fit with an exponential function.

5.5.1.2. Elastic Modulus Under Compressive Loading: As discussed in Chapter 2, many researchers have proposed empirical, semi-empirical or theoretical models to describe the behavior of the elastic modulus with respect to porosity. In this section, ten relevant models will be compared to the experimental data obtained through this research. During the fitting of these models, the value of the zero-porosity elastic modulus was taken as the average of published values and, when applicable, the value of Poisson's was limited by the minimum and maximum of published values (Table 2-1).

In Nielsen's model, P_D, the critical porosity, and M, the pore interaction power, have been set to unity, as suggested when modeling porous glasses. The fitting parameter describes the complexity of the pore structure and was allowed to vary between zero and one. In fitting the Phani-Niyogi model, the parameter a was varied between 1 and 3.85 as suggested in their published work. Fitting was performed in MATLAB (Appendix B) and the results are summarized in Table 5-10.

Table 5-10. Summary of fitting results for porosity vs. elastic modulus in compression, including regression analysis.

Fit Type	Value of Fitting Parameters				R^2	RMSE (GPa)
	a	b	n	v_o		
Hasselman	1430	--	--	--	0.9904	2.32
Nielsen	0.000701	--	--	--	0.9901	2.35
Wang	338.7	-1524	--	--	0.9869	2.92
Wagh - Poeppel-Singh	--	--	328.2	--	0.9844	2.95
Phani - Niyogi	1	--	328.2	--	0.9844	3.18
Spriggs	--	--	329.4	--	0.9844	2.95
MacKenzie	25.79	104.2	--	--	<0.001	35.54
Brown - Biddulph - Wilcox	3.368	--	--	--	<0.001	38.28
Ramakrishnan	--	--	--	0.21	<0.001	47.75
Hashin	--	--	--	0.24	<0.001	55.84

Based on the calculated values for R^2 and the root mean square error, the Hasselman and Nielsen models appear to fit the data most accurately. The models proposed by Wang, Wagh et al., Phani-Niyogi, and Spriggs also fit quite well; however, it should be noted that the best fit for the Phani-Niyogi model occurred when the value of *a* was set at unity. This renders the Phani-Niyogi model identical to the model proposed by Wagh et al. The models proposed by MacKenzie and Brown et al. are much less accurate. Both of these models use a polynomial approach and data are fit through manipulation of the coefficients. Ramakrishnan and Hashin's models, which utilize the zero porosity Poisson's ratio, fit very poorly as well. The ten models are plotted with the experimental data in Figures 5-80 through 5-89 on the following pages; they are presented according to the R^2 values, in descending order.

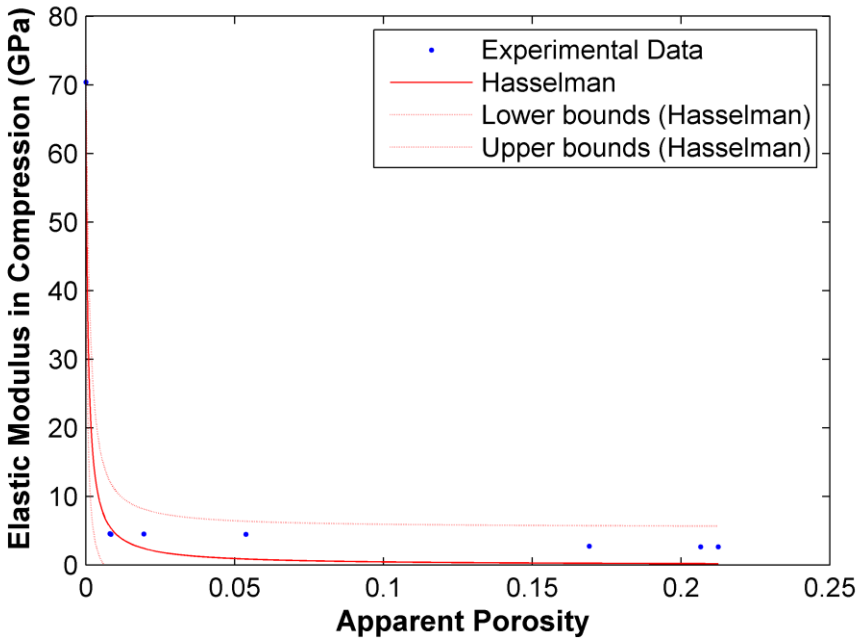

Figure 5-80. Porosity vs. mean elastic modulus in compression data fitted with the Hasselman correlation.

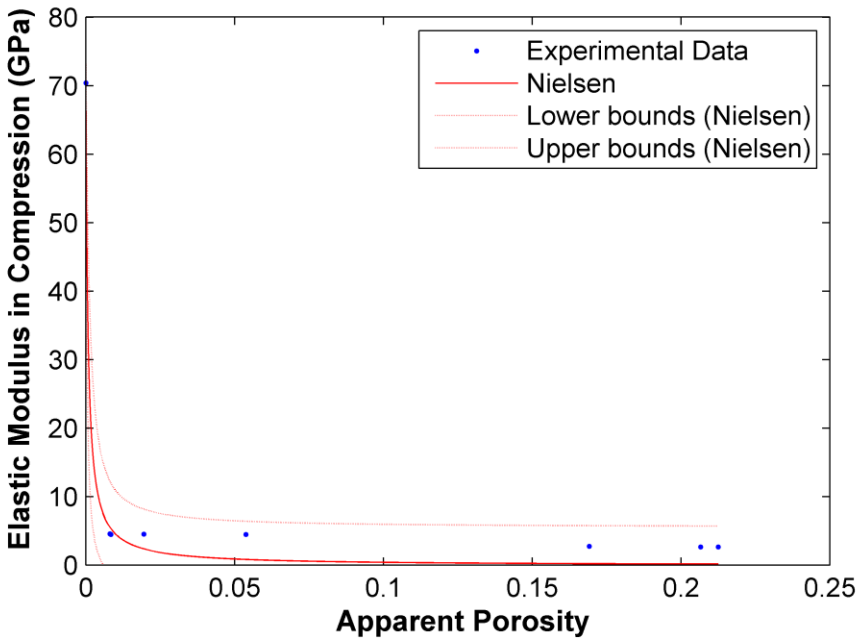

Figure 5-81. Porosity vs. mean elastic modulus in compression data fitted with the Nielsen correlation.

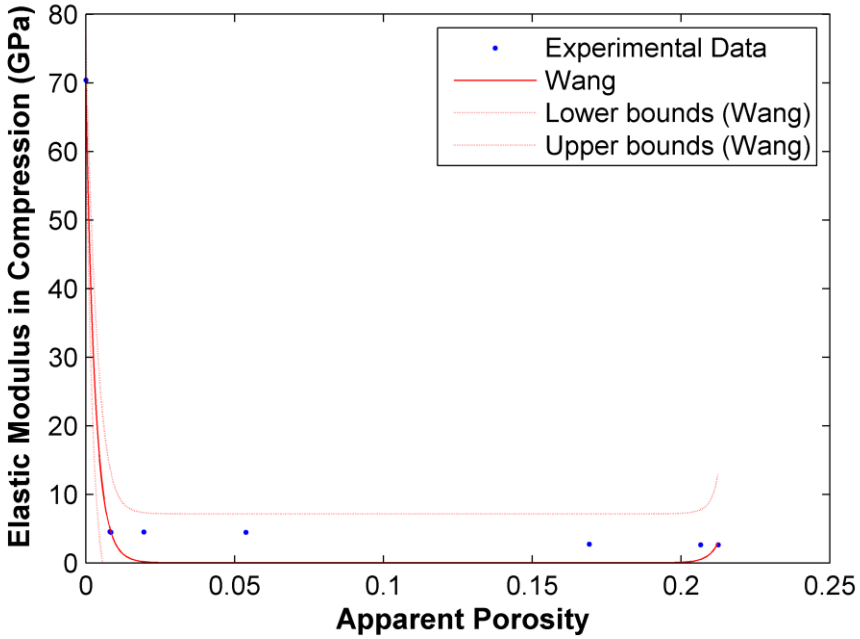

Figure 5-82. Porosity vs. mean elastic modulus in compression data fitted with the Wang correlation.

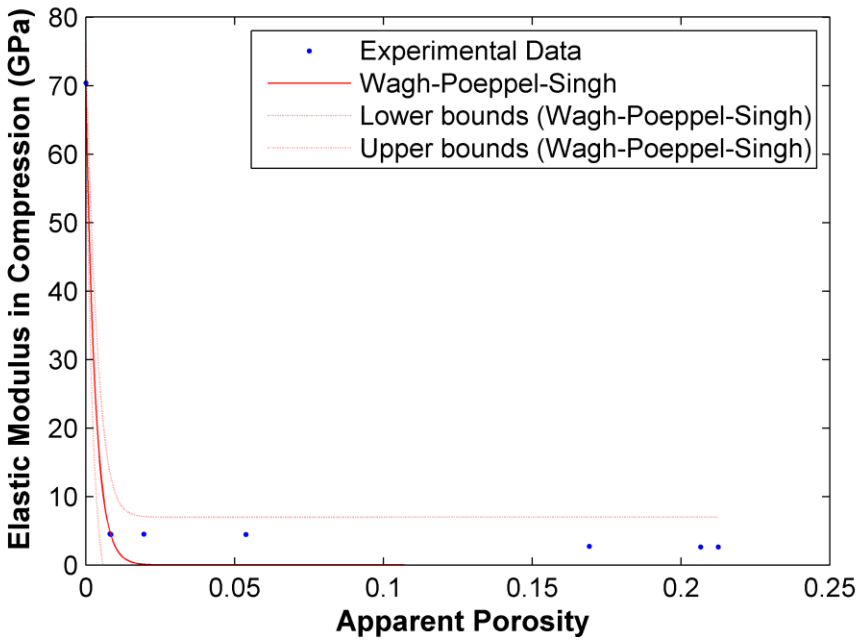

Figure 5-83. Porosity vs. mean elastic modulus in compression data fitted with the Wagh-Poeppel-Singh correlation.

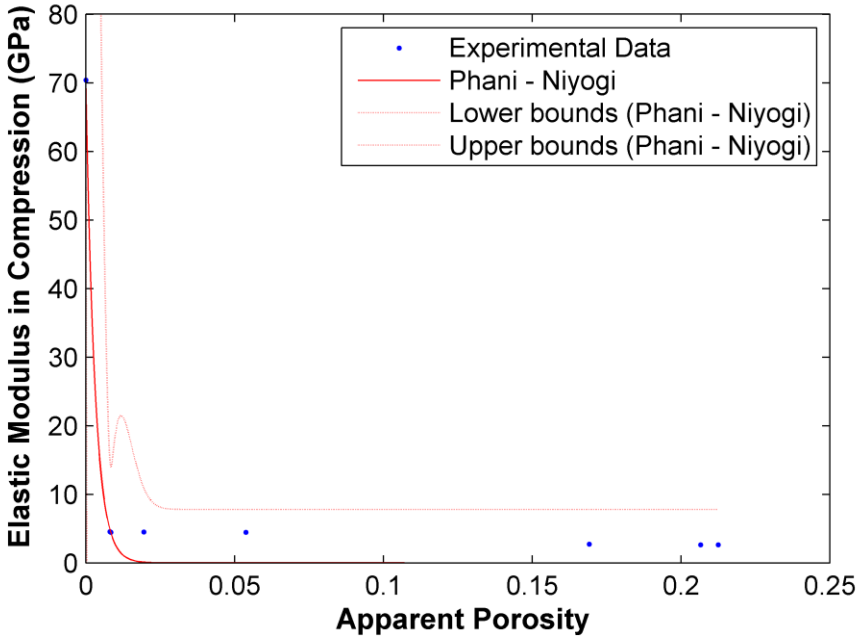

Figure 5-84. Porosity vs. mean elastic modulus in compression data fitted with the Phani-Niyogi correlation.

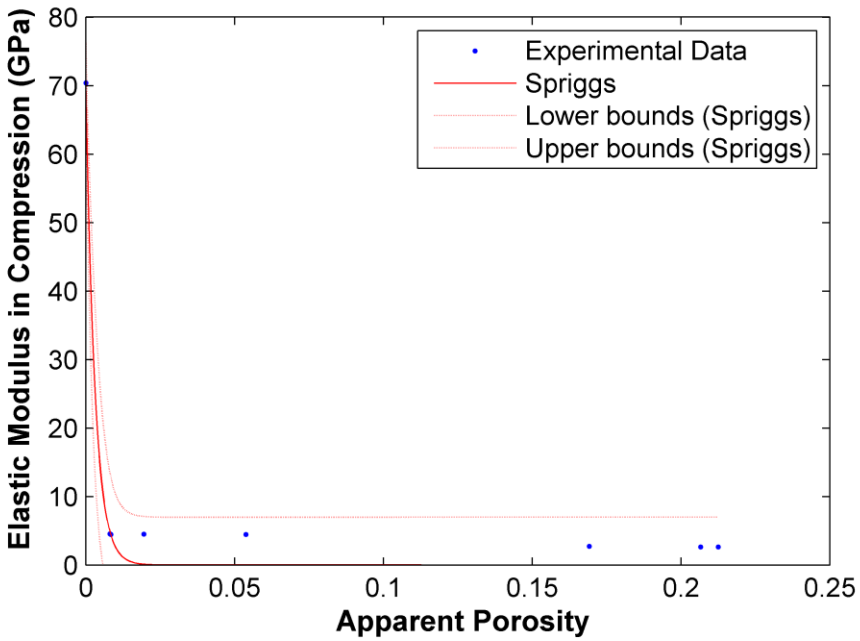

Figure 5-85. Porosity vs. mean elastic modulus in compression data fitted with the Spriggs correlation.

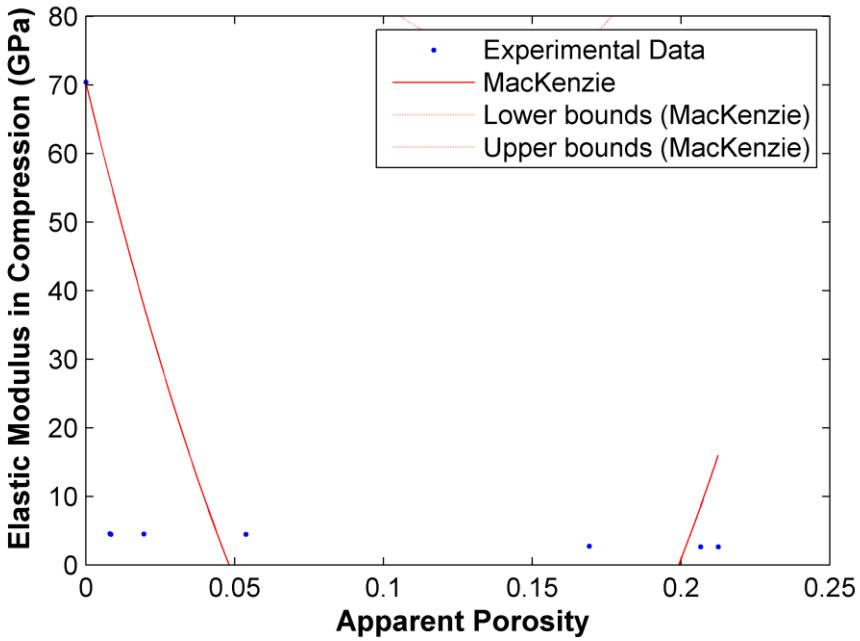

Figure 5-86. Porosity vs. mean elastic modulus in compression data fitted with the MacKenzie correlation.

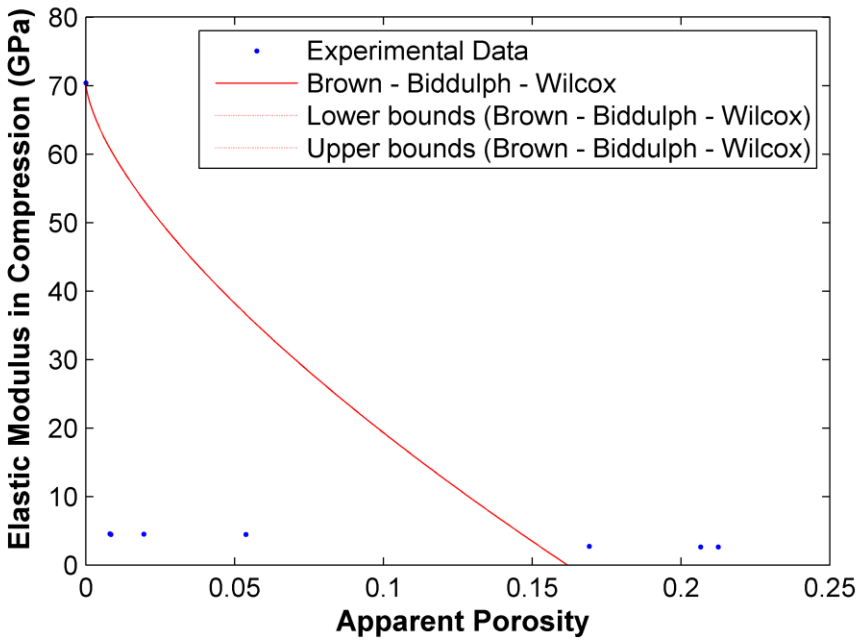

Figure 5-87. Porosity vs. mean elastic modulus in compression data fitted with the Brown-Biddulph-Wilcox correlation.

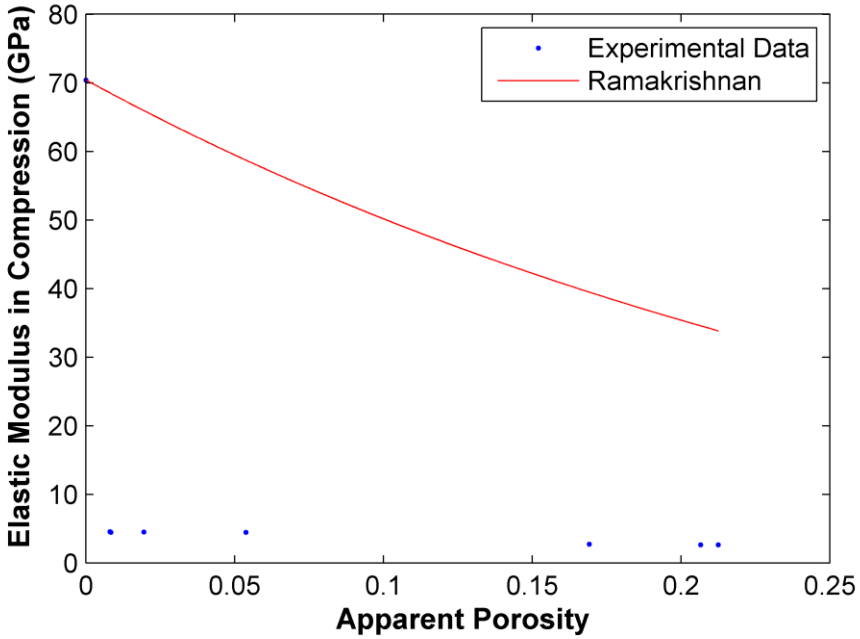

Figure 5-88. Porosity vs. mean elastic modulus in compression data fitted with the Ramakrishnan correlation.

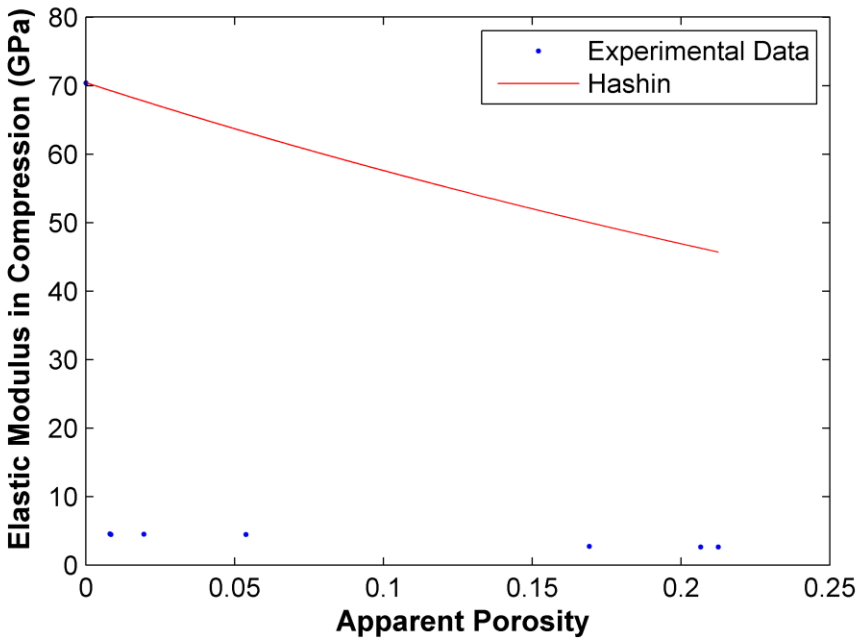

Figure 5-89. Porosity vs. mean elastic modulus in compression data fitted with the Hashin correlation.

Through inspection of the preceding figures, it can be seen that Hasselman and Nielsen's models fits the data most accurately based on the narrow 95% confidence interval as well as the high R^2 value. The Hasselman, Nielsen, Wang, Spriggs, Wagh-Singh-Poeppel and Phani-Niyogi models all fit the data reasonably well in the higher porosity ranges; however, the shape of the curves differs in the lower porosity ranges. The models proposed by MacKenzie, Brown et al., Ramakrishnan and Hashin fit the data quite poorly. The 95% confidence bounds on all four of these models are so large that they do not appear on the plots. In general, the confidence intervals calculated for these models can be observed to become slightly larger as the adjusted R^2 value increases, as would be expected. A comparison of the five most accurate models is shown graphically in Figure 5-90.

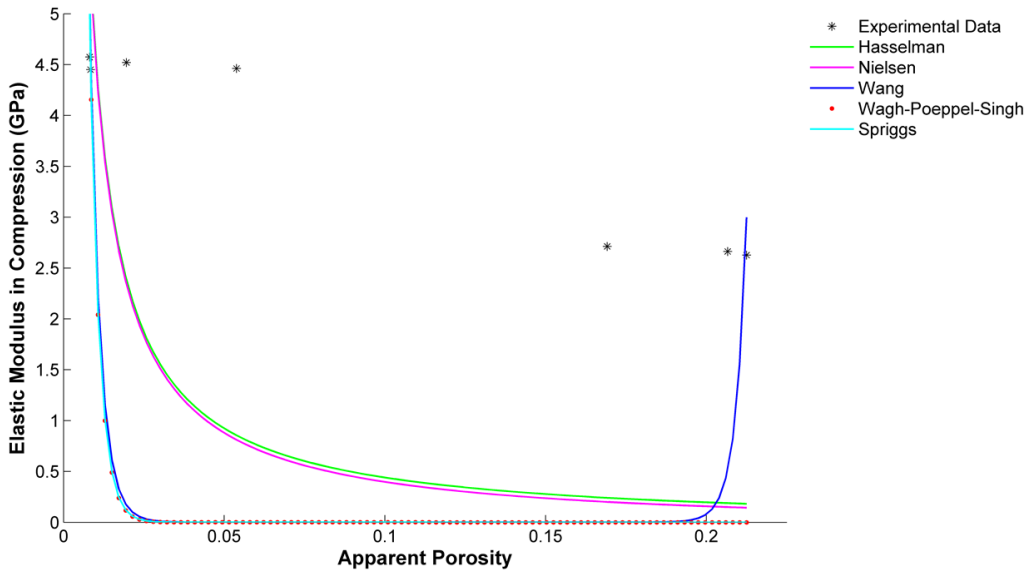

Figure 5-90. Comparison of porosity vs. elasticity models (compressive loading).

When models are compared within the range of experimental data, it can be seen that, although most correlations fit the data well in the lower porosity range, there is considerable deviation from the experimental data. Several models predict the elastic modulus in compression reasonable well when with respect to 95% confidence bounds; however these models all underpredict the values throughout most of the porosity range.

5.5.2. Comparison of Flexural Behavior to Models

5.5.2.1. Transverse Strength: In comparing the experimental results to the published zero-porosity transverse strength, an average value of published data was used (Table 2-1). The data was then fit using the exponential model (Eq. 2.8); Gibson and Ashby's models were not used as they were established for compressive strength alone. The results are shown in the Table 5-11 below and depicted graphically in Figure 5-90. The exponential model fits the experimental data for transverse rupture strength very poorly and the 95% confidence interval is extremely large.

Table 5-11. Summary of curve fitting results for transverse strength, including regression analysis.

Fit Type	Value of Fitting Parameters			R^2	RMSE (MPa)
	a	b	φ		
Duckworth (polished)	138	--	--	0.4250	27.57

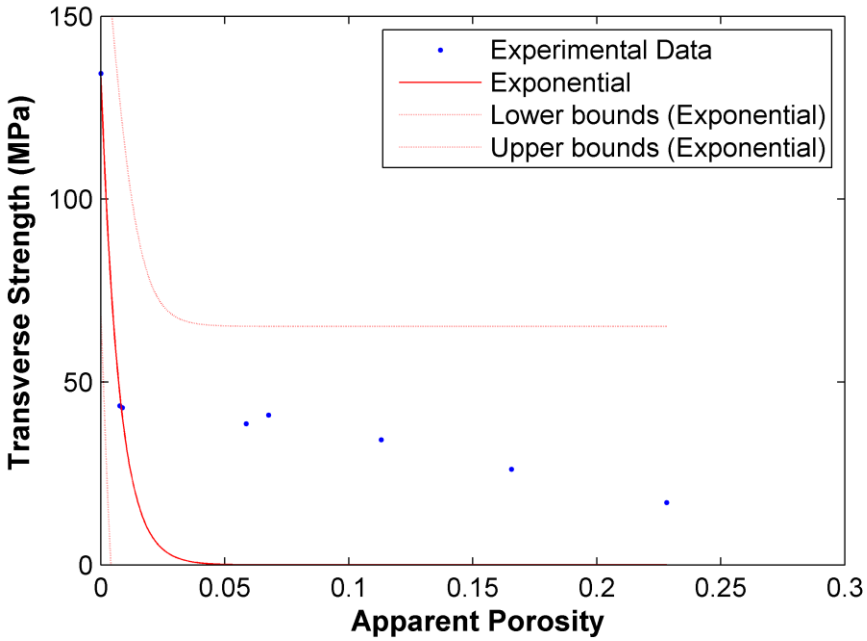

Figure 5-91. Experimental and published zero porosity data fit with an exponential function.

5.5.2.2. Elastic Modulus Under Transverse Loading: The experimental data for the elastic modulus in flexure was then fit using established models that relate the elastic modulus to the porosity of the specimens. A summary of the fitting analysis can be seen in Table 5-12 where the models are listed in descending order of adjusted R^2 value.

Table 5-12. Summary of fitting results for porosity vs. elastic modulus in flexure, including regression analysis.

Fit Type	Value of Fitting Parameters				R^2	RMSE
	a	b	n	v_o		
Hasselman	715.2	--	--	--	0.9311	5.82
Nielsen	0.001391	--	--	--	0.9296	5.88
Wang	270.2	-1133	--	--	0.9195	6.80
Spriggs	--	--	261	--	0.9121	6.58
Wagh - Poeppel-Singh	--	--	260	--	0.9121	6.58
Phani - Niyogi	1	--	260	--	0.9121	6.58
MacKenzie	15.57	53.17	--	--	<0.001	32.43
Brown - Biddulph - Wilcox	3.469	--	--	--	<0.001	32.16
Ramakrishnan	--	--	--	0.21	<0.001	43.61
Hashin	--	--	--	0.24	<0.001	51.78

As with the compressive testing data, the Hasselman and Nielsen models fit the data most accurately in terms of R^2 values and root mean square error. The models proposed by Wang, Spriggs, Wagh et al. and Phani-Niyogi also fit quite well, while the models proposed by MacKenzie, Brown et al., Ramakrishnan and Hashin fit quite poorly. As with the compressive data, the Phani-Niyogi model is rendered essentially identical to the Wagh-Poeppel-Singh model, as the fitting parameter *a* has been solved at unity. The models are plotted in Figures 5-92 through 5-101 along with the experimental data.

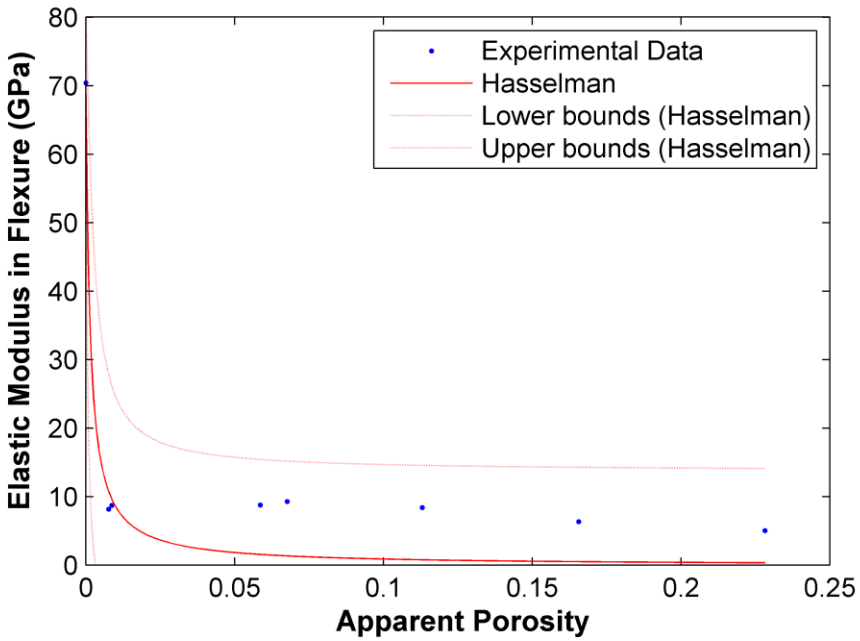

Figure 5-92. Porosity vs. mean elastic modulus in flexure data fitted with the Hasselman correlation.

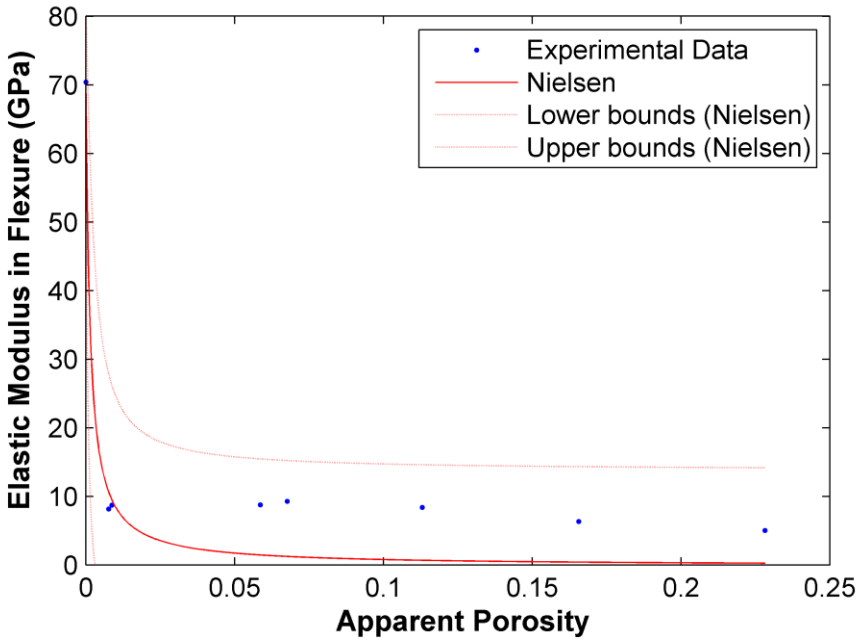

Figure 5-93. Porosity vs. mean elastic modulus in flexure data fitted with the Nielsen correlation.

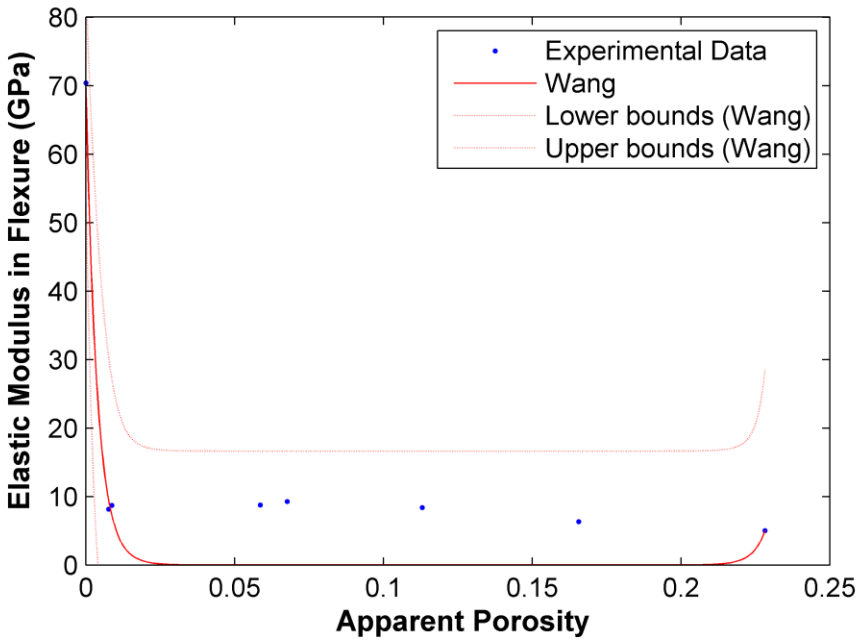

Figure 5-94. Porosity vs. mean elastic modulus in flexure data fitted with the Wang correlation.

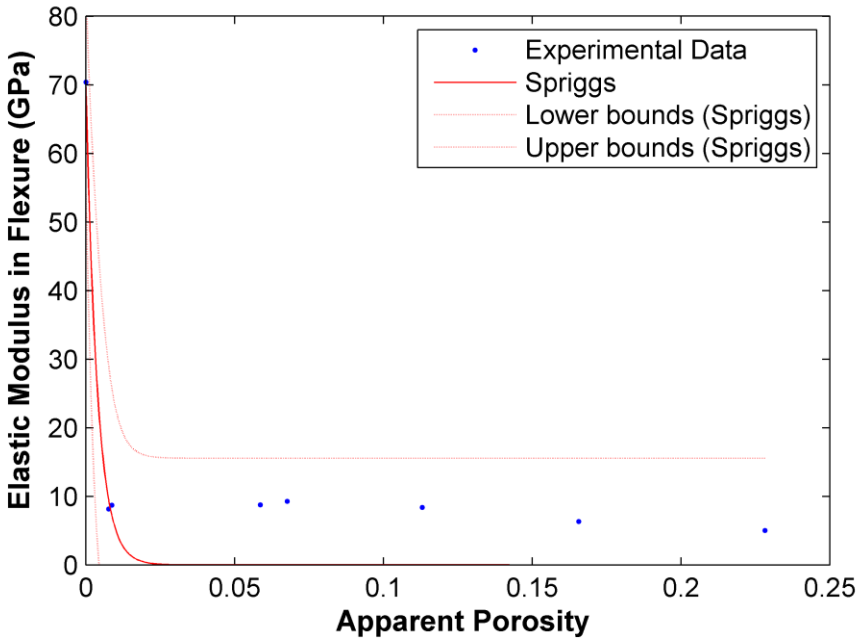

Figure 5-95. Porosity vs. mean elastic modulus in flexure data fitted with the Spriggs correlation.

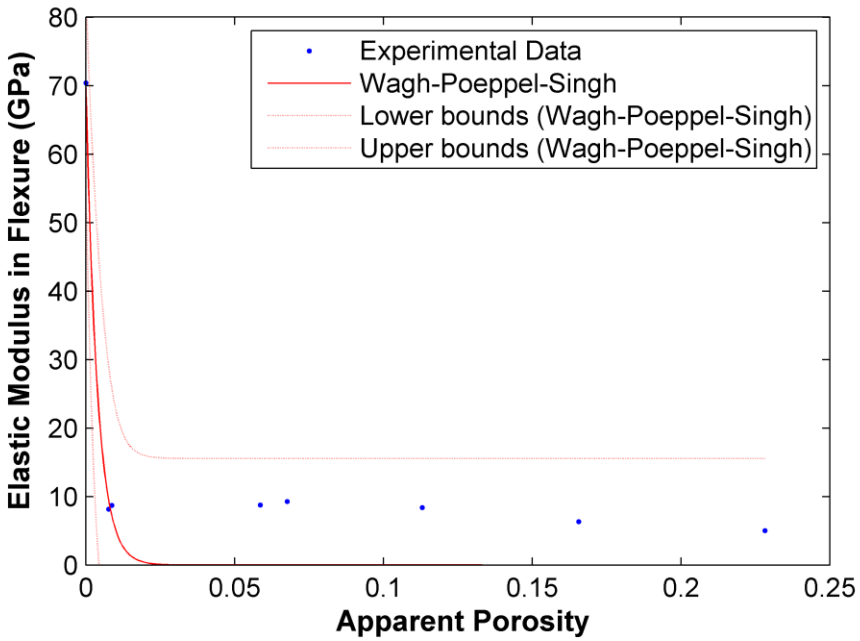

Figure 5-96. Porosity vs. mean elastic modulus in flexure data fitted with the Wagh-Poeppel-Singh correlation.

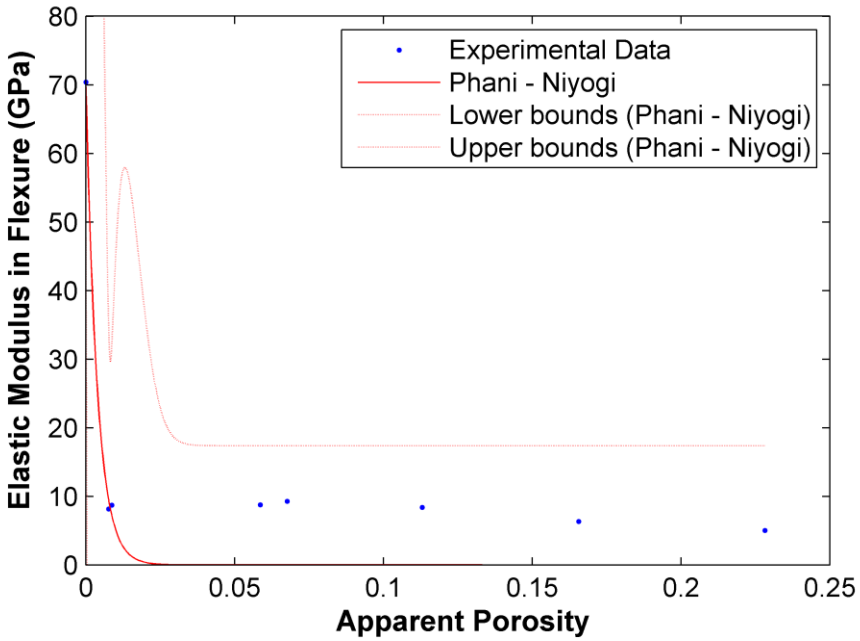

Figure 5-97. Porosity vs. mean elastic modulus in flexure data fitted with the Phani-Niyogi correlation.

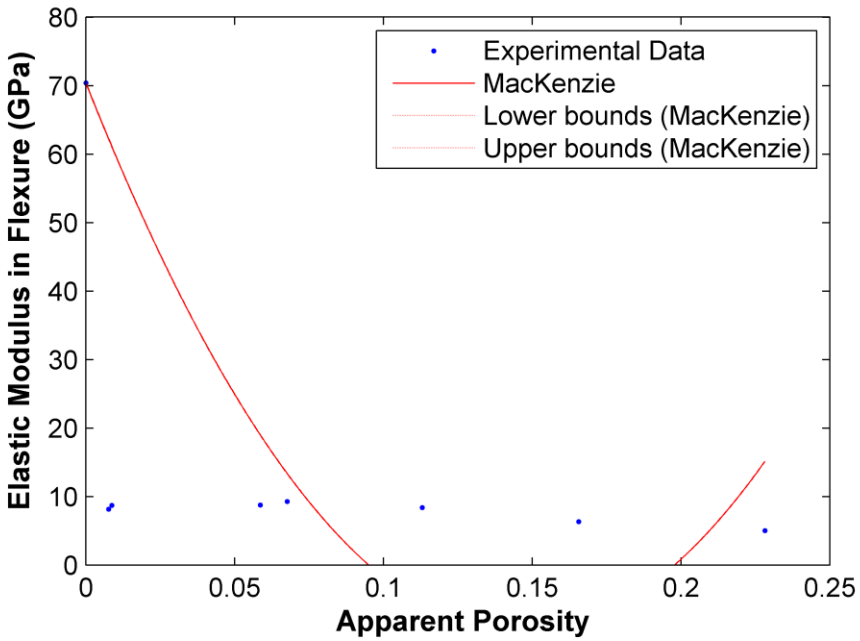

Figure 5-98. Porosity vs. mean elastic modulus in flexure data fitted with the MacKenzie correlation.

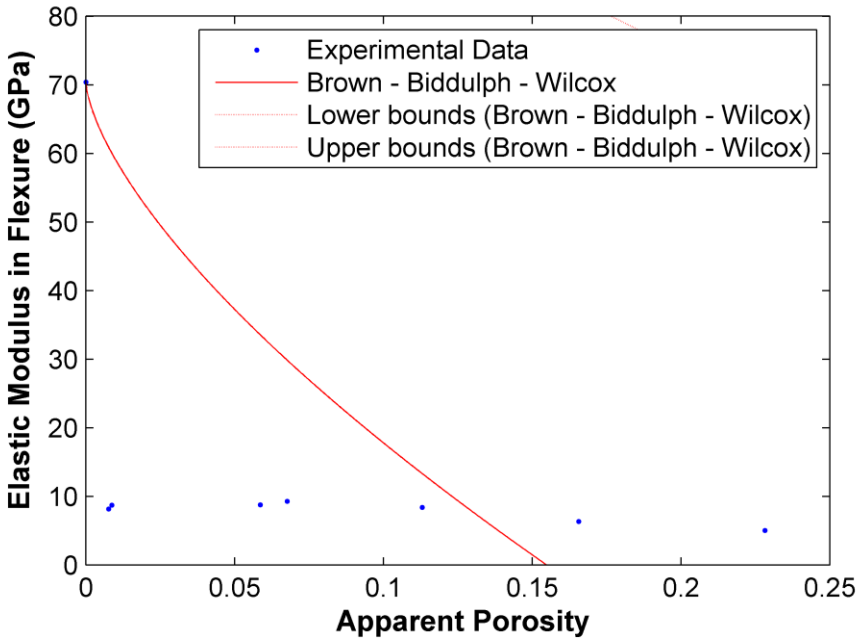

Figure 5-99. Porosity vs. mean elastic modulus in flexure data fitted with the Brown-Biddulph-Wilcox correlation.

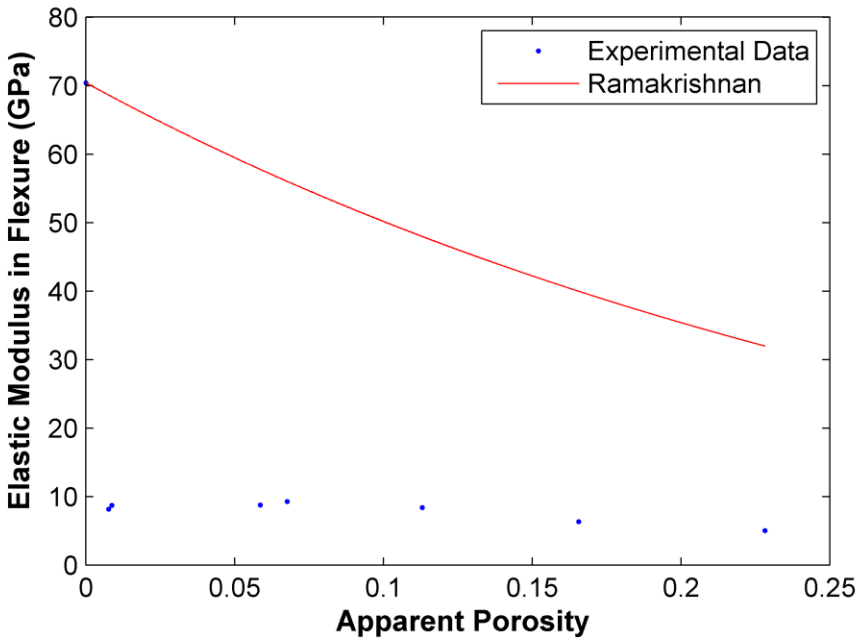

Figure 5-100. Porosity vs. mean elastic modulus in flexure data fitted with the Ramakrishnan correlation.

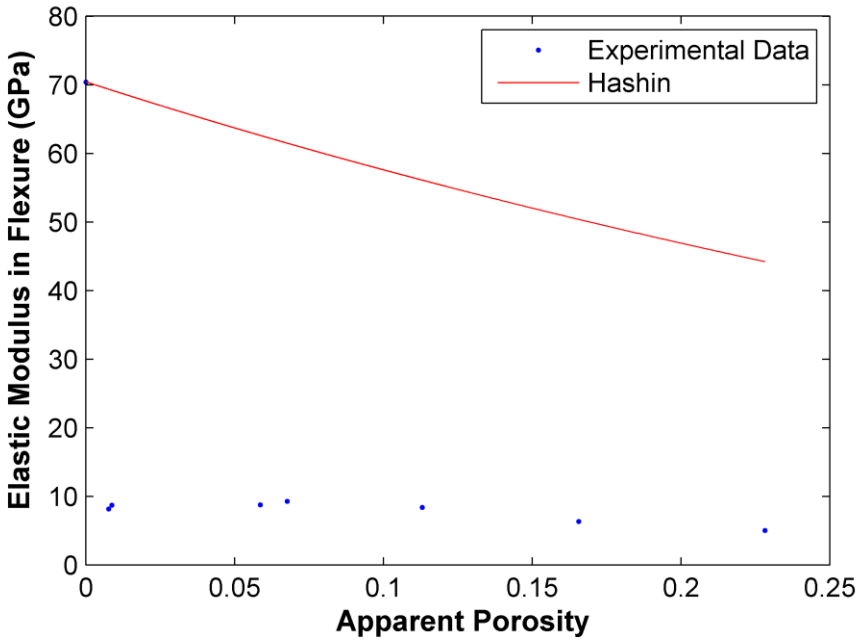

Figure 5-101. Porosity vs. mean elastic modulus in flexure data fitted with the Hashin correlation.

Through inspection of the preceding figures, it appears that none of the models predict the behavior of specimens subjected to transverse loading as accurately as the behavior of

compressively loaded specimens. The Hasselman and Nielsen's correlations again provide the most accurate fit to the data based on the narrow 95% confidence interval and the high R^2 values. However, even for these two models, the predicted values to not correspond as closely to the experimental data and confidence bounds are larger. The models proposed by MacKenzie, Brown et al., Ramakrishnan and Hashin fit the data quite poorly. Again, the 95% confidence bounds on both the Ramakrishnan and Hashin models are so large that they do not appear on the plots. A comparison of the five most accurate models is shown graphically in Figure 5-90.

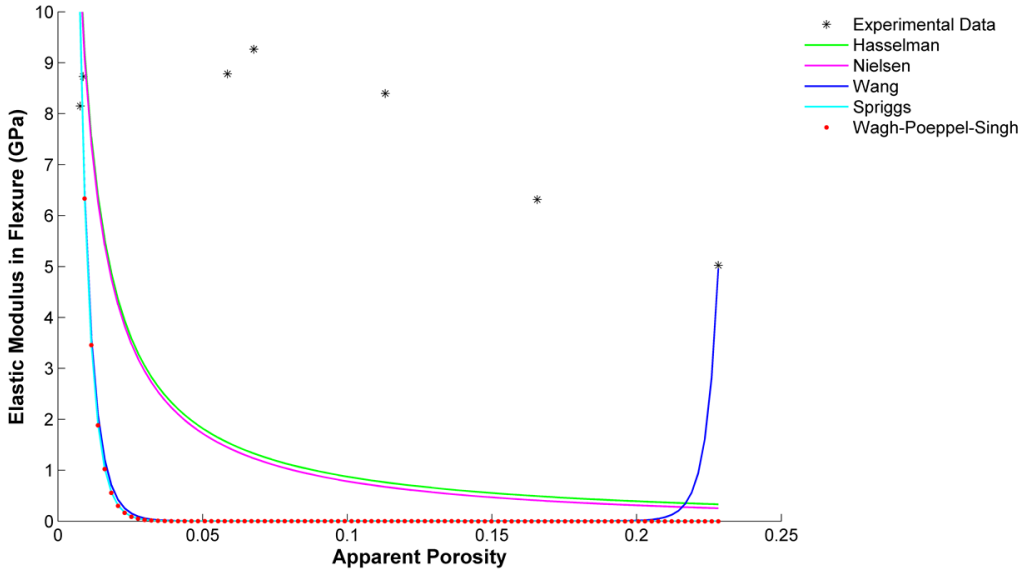

Figure 5-102. Porosity vs. mean elastic modulus in flexure data fitted with the Ramakrishnan correlation.

As with the data obtained through compressive testing, when models are compared within the range of experimental data, it can be seen that, although most correlations fit the data well in the lower porosity range, there is considerable deviation from the experimental data. While these models predict the elastic modulus in compression reasonable well when with respect to 95% confidence bounds, all five underpredict the values throughout most of the porosity range.

5.6. FRACTOGRAPHY

Flexure specimens were photographed following flexural testing and a representative sample of these micrographs can be seen in Figures 5-103 and 5-104, on the following pages. Images in Figure 5-103 depict characteristic unpolished specimens densified at three different temperatures, while images in Figure 5-104 depict similar specimens from polished batches. Photographs could not be obtained from compressive test specimens, as in all cases, the specimens were essentially reduced to powder and the majority of the material was ejected from the apparatus under high velocity.

Unpolished Specimen Densified at ~705°C

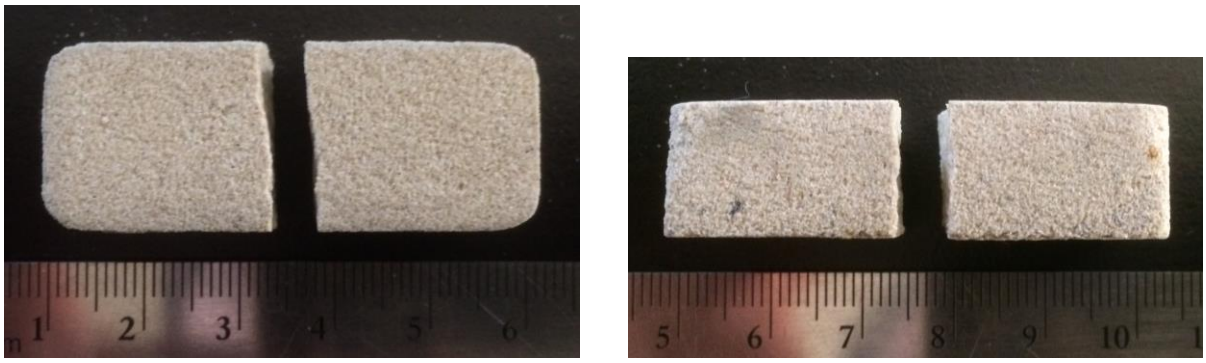

(a) (b)

Unpolished Specimen Densified at ~745°C

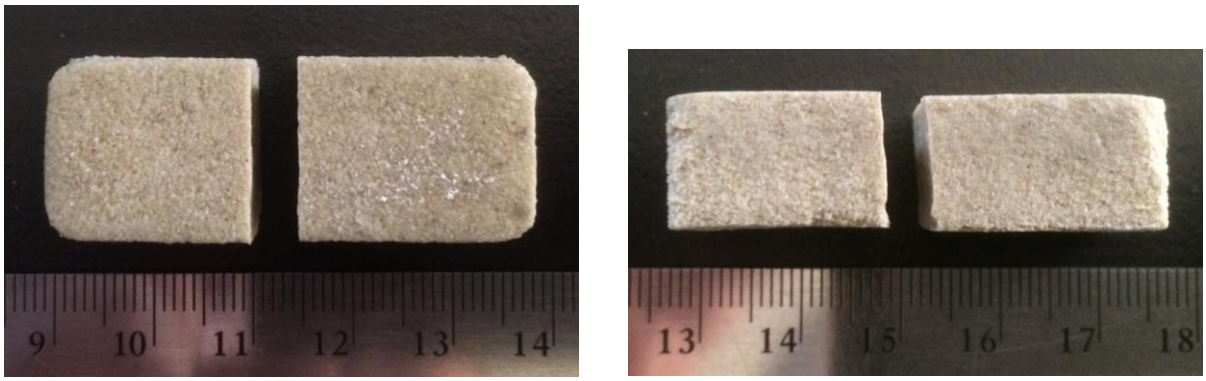

(c) (d)

Unpolished Specimen Densified at ~790°C

(e) (f)

Figure 5-103. Photographs of three characteristic unpolished specimens after failure due to 3-point bending. Images a), c) and e) show the loading surface of each specimen. Images b), d) and f) show the side view.

Polished Specimen Densified at ~705°C

(a)

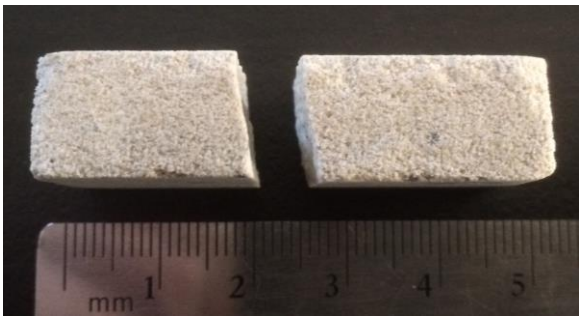

(b)

Polished Specimen Densified at ~745°C

(c)

(d)

Polished Specimen Densified at ~790°C

(e)

(f)

Figure 5-104. Photographs of three characteristic polished specimens after failure due to 3-point bending. Images a), c) and e) show the loading surface of each specimen. Images b), d) and f) show the side view.

In examining the photographs on the previous pages, it can be seen that failure occurs towards the center of each specimen. This region is the gage section in the 3-point bend test and these results were expected. Looking at the side views (right column), the majority of specimens appear to exhibit roughly vertical fracture surfaces. This makes sense, as the direction of crack propagation and growth would be dependent on the location and size of pores. Because the pores are randomly sized and distributed, non-planar fracture surfaces would be expected.

CHAPTER 6. DISCUSSION

Overall, the results confirm the preliminary findings that contaminated waste glass could be densified successfully through very low temperature sintering[4]. The peak densification temperatures can be varied between 705°C and 790°C to produce materials that exhibit a broad range of apparent porosity. The volumetric strain that occurs through the densification process is directly related to this porosity and within the 705 to 760°C temperature range, the relationship appears to be linear (Figure 5-10). The same can be said of the relationship between peak densification temperature and apparent porosity (Figure 5-11), as well as the relationship between peak densification temperature and bulk density (Figure 5-12). Above 760°C these linear relationships are not observed. As discussed in Chapter 5, limitations of the volumetric strain measurement technique and of the Archimedes' test method may have contributed to this behavior. However, 750°C marks the onset of crystallization in soda-lime silicate glasses and it is quite likely that progression of the sintering phenomena also played a role.

6.1 PROCESS DEVELOPMENT

The data collected and analyzed over the course of this investigation appears to confirm that inconsistencies in specimen formation procedures and geometric distortion present in fired specimens contributed to disagreement between expected and observed physical and mechanical behavior previously observed[4]. The results presented in section 5.1.1. indicate that the press force used during specimen formation in prior investigations was below the resolution of the equipment. In addition, the forces employed may not have allowed for full compaction of the specimens, so irregularities in packing density were likely present.

Moreover, the results presented in section 5.2. confirm that improper seating of specimens during compressive and flexural loading led to poorly behaved stress-strain data.

Although geometric distortion was not completely eliminated during this investigation, polishing of the loading surfaces allowed for specimens to make full contact with the loading plates. This, in turn, led to more evenly distributed loading and minimized cleavage and premature fracture of specimens.

6.2. Compressive Behavior

Although prior investigations indicated that this material does not behave in a manner consistent with brittle solids, where unloading occurs abruptly at the point where maximum stress is achieved, similar observations made from polished specimens contradict this finding (Figures 5-13 through 5-19). Because unpolished specimens exhibit geometric distortion, particularly in the lower porosity ranges, the specimens are not uniformly loaded during testing. It is quite likely that small pieces of the specimens are cleaving off during testing, which may account for discontinuities observed in the elastic region of the curve and plateaus observed after maximum stress was achieved. This research shows that once the specimens are polished and allowed to make full contact with the loading surfaces, discontinuities, load drops and stepped unloading are minimized. Instead the specimens exhibit well behaved, linear stress-strain behavior in the elastic region of the curves and experience sudden and catastrophic failure. This was observed to be true throughout the full range of peak densification temperatures used in this investigation. Both of these phenomena are consistent with the behavior of dense ceramics, porous media and brittle materials in general[22].

The compressive strength and elastic modulus in compression results from this investigation could not be directly compared to the results from prior investigations, as the specimen formation process was modified. Although data was collected from unpolished

specimens in this investigation, the formation pressures were increased as a result of the process development tasks discussed in Section 4.1.

The results of this work are very encouraging when compared to ASTM standards for common structural ceramic building products. The requirements for compressive strength vary with application and regional considerations. In facing brick and building brick products are expected to withstand between 10 and 21 MPa respectively before failure[59, 60], while requirements for paving brick products range from 21 to 56 MPa[61]. Through compressive testing it was determined that compressive strength values between ~99 and ~245 MPa can be achieved at peak densification temperatures in the range of ~705°C and 790°C.

6.2. Flexural Behavior

The results of flexural testing followed similar trends as those discussed above for the compressive data. Under transverse loads, the material behaved in a manner consistent with both brittle solids and porous materials. Unloading occurred abruptly, immediately following the point of maximum stress (Figures 5-45 through 5-51). Again, for polished specimens the stress strain curves were much better behaved, maximum stress values were higher, and the variation in those values was considerably smaller. In addition, the transverse strength was substantially higher than the compressive strength in all cases, which is generally the case for brittle and porous materials[22]. Although discontinuities and load drops are present in the data for unpolished specimens these behaviors are far less pronounced than was the case under compressive loading (Figures 5-13 through 5-19).

Under transverse loading, the elastic portion of the curves for polished specimens appears to be considerably more non-linear (Figures 5-52 through 5-58). Again, even in the case of polished specimens, the stress-strain behavior appears to be non-linear during initial loading.

Further inspection of the stress-strain curves also shows that, in all cases, the maximum stress exhibited by specimens in a given batch is more consistent than was observed under compressive loading (Figures 5-20 through 5-26). However, the elastic portion of the stress-strain curves shows considerably more variability in slope in both polished and unpolished specimens.

As with the compressive data the, strength and elastic modulus results from this investigation could not be directly compared to the results from prior investigations, as the specimen formation process was modified (Section 4.1). Because structural ceramics are brittle in nature, they are not often specified for transverse loading situations. In building materials, the most common application is roof tiles, which are required to withstand 7.5 to MPa before failure[55]. Through flexural testing it was determined that transverse strength values between 17 and 43.5 MPa can be achieved at peak densification temperatures in the range of ~705°C and 790°C.

It should be noted that, because the strain under transverse loading was calculated from crosshead extension data, a degree of inherent error may be present. In future studies, more accurate results may be obtained through direct measurement of strain via strain gages. Further, the equations used in calculating both the stress and strain under transverse loading assume that the neutral surface bisects the specimen. This is likely not accurate for several reasons. First, the cross-sectional shape is not rectangular and instead varies from specimen to specimen as a result of densification through heating. Second, it is unlikely that the pore distribution is uniform throughout the specimens. This non-uniform distribution can be attributed to the random size and shape of particles present in the feedstock, which would allow for the creation of both isolated and interconnected pores that are randomly distributed. It could also be brought about through processing conditions. During specimen formation, friction between the material and the tooling

(e.g. molds and dies) can cause considerable variations in density during powder compaction process, such as CIP. This could be further intensified during densification through the evolution of gaseous byproducts. In addition, fired ceramics often exhibit increased densification on the free surfaces.

6.3. Porosity-Property Modeling

Comparison of the experimental data with correlations established for predicting the mechanical properties of porous materials as a function of their porosity yielded mixed results. Although several correlations fit the data reasonably well with respect to error analyses, almost half fit quite poorly (Tables 5-9 through 5-12). Observations of Figures 5-80 through 5-89 (compressive loading) and Figures 5-91 through 5-100 (transverse loading) show that, of the empirical and semi-empirical correlations, the Hasselman, Wang, Wagh-Poeppel-Singh and Spriggs models predicted the elastic modulus reasonably well, while the Phani-Niyogi, MacKenzie, and Brown-Biddulph performed very poorly. This was somewhat unexpected as the correlations proposed by Wang and Spriggs made the assumption of spherical particles in a cubic packing arrangement, while the model proposed by Brown et.al. was created based on observations of pore geometry and orientation.

The two-phase models proposed by Hashin and Ramakrishnan, which incorporated the zero-porosity value of Poisson's ratio, were among the worst at accurately modeling the experimental data. As expected, Nielsen's model, which is based on phenomenological criteria fit quite well; however, the fitted value for the dimensionless shape factor (μ_o) was much smaller (0.0007) than expected based on his investigations of porous glass, which exhibited values that ranged from 0.25 to 0.5.

Overall, the correlations do not appear to model the mechanical behavior of the material as well as was shown in the previous study[4], which did not include data from specimens that exhibit porosity values below ~7%. This is important, as it is within the lower porosity ranges that the greatest increase in values for the elastic modulus would be expected. Above ~10% porosity all models predict roughly linear behavior, whereas below ~10% the highest degree of non-linearity in the models is present.

CHAPTER 7. CONCLUSIONS

During the course of this research several processing issues were identified. These include limitations in CIP equipment, improper specimen seating during mechanical testing and error in calculation of mechanical properties due to machine compliance. Once these issues were addressed, the physical and mechanical behavior of the material were evaluated and the mechanical properties were compared to theoretical models. Based on the experimental investigation the following conclusions can be made:

1. Marchelli and Prabhakar's process for creating macro-scale porous materials, from recycled glass results in predictable physical and mechanical behavior.
2. Volumetric shrinkage, apparent porosity, and bulk density follow linear relationships within the 705°C and 760°C range of peak densification temperatures. However, above 760°C these relationships are no longer observed.
3. Under both compressive and transverse loading the material exhibit stress-strain behavior consistent with brittle solids and cellular or porous material. Irregularities observed previously appear to be largely due to improper seating of specimens during mechanical testing. Inconsistent packing during formation via CIP may also have played a role.
4. Both compressive and transverse strength can be related reasonably well to apparent porosity through an exponential relationship. Comparison of data obtained through compressive testing to models for cellular materials yielded poor results. This is consistent with the fact that the material does not exhibit an ordered pore structure composed solely of open or closed cells.

5. A phenomenological approach to modeling the relationship between porosity and the elastic modulus provides the most accurate results. In general, empirical and semi-empirical models for predicting the elastic modulus based on the apparent porosity do not accurately predict the behavior of the material. The semi-empirical models that assumed spherical particles performed somewhat well, while, in general, those that accounted for the zero-porosity value of Poisson's ratio performed worst.

6. As was the case in the previous study[4], values for the elastic modulus obtained through compressive and flexural testing do not agree. This contradicts the original hypothesis that irregular specimen geometry played the largest role in this disagreement. Larger values for the elastic modulus under transverse rather than compressive loading may be due to inherent anisotropy of the material. However, the effects of contamination may also have played a role in this observation.

7. The densification process used during experimentation is compatible with contaminated waste glass. The presence of micro-scale organic and inorganic contaminants has not prevented sintering and through manipulation of peak densification temperature, sufficient strength can be achieved for a variety of construction applications.

8. High strength materials can be created at much lower temperatures than previously thought, which results in end products with very low embodied energy. This would reduce both greenhouse gas emissions and manufacturing costs.

CHAPTER 8. RECOMMENDATIONS FOR FUTURE WORK

1. As Prabhakar stated[4], characterization of the mechanical behavior of this material would benefit from 4-point bending tests, rather than 3-point. In the 4-point bend test, shear forces between the two loading members is zero and bending stresses are uniform over the entire area between the two loads. Because the area over which bending stresses are applied is larger, the probability of encountering a defect is larger as well. Hence, the 4-point method may yield more realistic values of transverse rupture strength.

2. This research would benefit from a thorough fractographic investigation of failed specimens throughout the range of porosity. Inspection of the Weibull probability plots for compressive strength (Appendix C) indicate that a linear fit may not be applicable in all cases, particularly in the lower porosity ranges. Although analysis of the data using the three-parameter Weibull distribution may provide more reliable information regarding the probability of failure in components, taking a phenomenological approaching may explain these discrepancies in a way that would provide information useful towards further process development.

3. The flexural behavior of larger specimens is currently unknown. It is widely recognized that the transverse rupture strength of porous and brittle materials does not remain constant with changes in specimen size. A thorough investigation of this phenomenon in porous glass materials has not yet been performed.

4. Although established theoretical models have been shown to fit the experimental reasonably well, it is possible that a more accurate, phenomenological model can be developed. Because of the high variability in the waste glass feedstock, a phenomenological model would prove more useful in industry.

5. Very little work has been performed with contaminated waste glass. Successfully using waste glass as a primary feedstock will require a comprehensive understanding of how contaminants in the supply will affect the microstructure and mechanical properties.

REFERENCES

1. EPA. *Glass*. Common Wastes & Materials June 21, 2014; Available from: http://www.epa.gov/waste/conserve/materials/glass.htm.
2. Marchelli, G.P., R., *Porous glass articles formed using cold work process* USPTO, Editor. 2013.
3. Marchelli, G. and R. Prabhakar, *NSF SBIR Phase I Final Report*. 2012.
4. Prabhakar, R. and M. Ramulu, *Compressive and flexural properties of porous building materials created from contaminated waste glass. Thesis*. 2012, University of Washington.
5. EPA. *Municipal Solid Waste Generation, Recycling, and Disposal in the United States: Facts and Figures for 2012*. 2014; Available from: https://www3.epa.gov/epawaste/nonhaz/municipal/pubs/2012_msw_fs.pdf.
6. *The Bottle Bill & Redemption Centers: About the Bottle Bill*. Available from: https://www.oregon.gov/OLCC/pages/bottle_bill.aspx.
7. *Waste Management Inc.: Single Stream Recycling Restaurant Solutions*. 2016; Available from: http://www.wm.com/enterprise/food-and-retail/Restaurant-Solutions/single-stream-recycling.jsp.
8. Lakhan, C., *A Comparison of Single and Multi-Stream Recycling Systems.* Resources, 2015. **4**: p. 384-397.
9. Guilherme, P., M.J. Ribeiro, and J.A. Labrincha, *Behaviour of different industrial ceramic pastes in extrusion process.* Advances in Applied Ceramics, 2009. **108**(6): p. 347-351.
10. Harper, C.A., *Handbook of ceramics, glasses, and diamonds*. 2001, New York: McGraw-Hill.
11. Bansal, N.P. and R.H. Doremus, *Handbook of glass properties*. 1986, Orlando: Academic Press.
12. Mencík, J., *Strength and fracture of glass and ceramics*. 1992, Amsterdam; New York: Elsevier.
13. Bengisu, M., *Engineering ceramics*. 2001, Berlin; New York: Springer.
14. Gibson, L.J. and M.F. Ashby, *Cellular solids : structure and properties*. 1997, Cambridge; New York: Cambridge University Press.
15. McLellan, G.W. and E.B. Shand, *Glass engineering handbook*. 1984, New York: McGraw-Hill.
16. German, R.M., *Sintering Theory and Practice*. 1996, New York: John Wiley & Sons, Inc.
17. Kuczynski, G.C. *Sintering processes*. in *International Conference on Sintering Related Phenomena*. New York: Plenum Press.
18. Rahaman, M.N., *Sintering of ceramics*. 2008, Boca Raton, FL: CRC Press.
19. Scott, W.D., *Densification, Crystallization, and Sticking Behavior of Crushed Waste Glass Sintered in Refractory Molds with Release Agents*. 2000, Clean Washington Center: Seattle.
20. Djohari, H., J.I. Martínez-Herrera, and J.J. Derby, *Transport mechanisms and densification during sintering: I. Viscous flow versus vacancy diffusion.* Chemical Engineering Science, 2009. **64**(17): p. 3799-3809.
21. Hibbeler, R.C., *Mechanics of materials*. 1997, Upper Saddle River, N.J.: Prentice Hall.
22. Dowling, N., *Mechanical behavior of materials: engineering methods for deformation, fracture, and fatigue.* 1993, Upper Saddle River: Prentice Hall.
23. Enke, D., F. Janowski, and W. Schwieger, *Porous glasses in the 21st century––a short review.* Microporous and Mesoporous Materials, 2003. **60**(1–3): p. 19-30.
24. Haux, E.H., *Method of Preparing Cellular Materials*, USPTO, Editor. 1940.
25. Ford, D., *Nodulated Cellular Glass and Method of Forming*, USPTO, Editor. 1954.
26. Spiridonov, Y.A. and L.A. Orlova, *Problems of Foam Glass Production.* Glass and Ceramics Glass and Ceramics, 2003. **60**(9/10): p. 313-314.
27. Manevich, V. and K. Subbotin, *Mechanism of foam-glass formation.* Glass and Ceramics, 2008. **65**(5-6): p. 5-6.

28. Manevich, V. and K. Subbotin, *Foam glass and problems of energy conservation.* Glass and Ceramics, 2008. **65**(3-4): p. 3-4.
29. Demidovich, B.K., et al., *New Production Line for the Manufacture of High Quality Foam Glass.* Glass and Ceramics (English translation of Steklo i Keramika), 1972. **29**(9-10): p. 651-654.
30. Éidukyavichus, K.K., et al., *Use of cullet of different chemical compositions in foam glass production.* Glass and Ceramics (English translation of Steklo i Keramika), 2004. **61**(3-4): p. 77-80.
31. Tulyaganov, D.U., et al., *Preparation and characterization of high compressive strength foams from sheet glass.* Journal of Porous Materials, 2006. **13**(2): p. 133-139.
32. Bernardo, E., et al., *Recycling of waste glasses into partially crystallized glass foams.* Journal of Porous Materials, 2010. **17**(3): p. 359-365.
33. Bernardo, E. and G. Scarinci, *Fast sinter crystallisation of waste glasses.* Advances in Applied Ceramics: Structural, Functional & Bioceramics, 2008. **107**(6): p. 344-349.
34. Bernardo, E., E. Bonomo, and A. Dattoli, *Optimisation of sintered glass–ceramics from an industrial waste glass.* Ceramics International, 2010. **36**(5): p. 1675-1680.
35. Rosli, N.R., et al., *Characterisation and properties of sintered recycled glass utilising CIP method*. 2011. p. 245-250.
36. Schabbach, L.M., et al., *Integrated approach to establish the sinter-crystallization ability of glasses from secondary raw material.* Journal of Non-Crystalline Solids, 2011. **357**(1): p. 10-17.
37. Ryshkewitch, E., *Compression Strength of Porous Sintered Alumina and Zirconia.* J American Ceramic Society Journal of the American Ceramic Society, 1953. **36**(2): p. 65-68.
38. Duckworth, W., *Discussion of Ryshkewitch Paper by Winston Duckworth*.* J American Ceramic Society Journal of the American Ceramic Society, 1953. **36**(2): p. 68-68.
39. Spriggs, R.M., *Expression for Effect of Porosity on Elastic Modulus of Polycrystalline Refractory Materials, Particularly Aluminum Oxide.* J American Ceramic Society Journal of the American Ceramic Society, 1961. **44**(12): p. 628-629.
40. Knudsen, F.P., *Dependence of Mechanical Strength of Brittle Polycrystalline Specimens on Porosity and Grain Size.* J American Ceramic Society Journal of the American Ceramic Society, 1959. **42**(8): p. 376-387.
41. Brown, S.D., R.B. Biddulph, and P.D. Wilcox, *A Strength-Porosity Relation Involving Different Pore Geometry and Orientation.* Journal of the American Ceramic Society, 1964. **47**(7): p. 320-322.
42. Wang, J.C., *Young's modulus of porous materials.* Journal of Materials Science, 1984. **19**(3): p. 801-808.
43. Phani, K.K. and S.K. Niyogi, *Young's modulus of porous brittle solids.* Journal of Materials Science, 1987. **22**(1): p. 257-263.
44. Wagh, A.S., R.B. Poeppel, and J.P. Singh, *Open pore description of mechanical properties of ceramics.* Journal of Materials Science, 1991. **26**(14): p. 3862-3868.
45. Mackenzie, J.K., *The Elastic Constants of a Solid Containing Spherical Holes.* Proceedings of the Physical Society of London Section B, 1950. **63**(361): p. 2-11.
46. Hashin, Z., *Citation Classic - the Elastic-Moduli of Heterogeneous Materials.* Current Contents/Engineering Technology & Applied Sciences, 1988(39): p. 14-14.
47. Hasselman, D.P.H., *On the Porosity Dependence of the Elastic Moduli of Polycrystalline Refractory Materials.* Journal of the American Ceramic Society, 1962. **45**(9): p. 452-453.
48. Ramakrishnan, N., *Effective elastic moduli of porous ceramic materials.* Journal of the American Ceramic Society, 1993. **76:11**: p. 2745-2752.
49. Nielsen, L.F., *Elasticity and Damping of Porous Materials and Impregnated Materials.* J American Ceramic Society Journal of the American Ceramic Society, 1984. **67**(2): p. 93-98.

50. Nielsen, L.F., *Strength and Stiffness of Porous Materials.* Journal of the American Ceramic Society, 1990. **73**(9): p. 2684-2689.
51. Lu, G., G.Q. Lu, and Z.M. Xiao, *Mechanical Properties of Porous Materials.* Journal of Porous Materials, 1999. **6**(4): p. 359.
52. ASTM, *C373 Standard Test Method for Water Absorption, Bulk Density, Apparent Porosity, and Apparent Specific Gravity of Fired Whiteware Products*. 2006, ASTM International: West Conshohocken, PA.
53. ASTM, *E9 Standard Test Methods of Compression Testing of Metallic Materials at Room Temperature*. 2009, ASTM International: West Conshohocken, PA.
54. ASTM, *C67 Standard Test Methods for Sampling and Testing Brick and Structural Clay Tile*. 2011, ASTM International: West Conchocken, PA.
55. ASTM, *C1167 Standard Specification for Clay Roof Tiles*. 2011, ASTM International: West Conshohocken, PA.
56. Kalidindi, S.R., A. Abusafieh, and E. EI-Danaf, *Accurate Characterization of Machine Compliance for Simple Compression Testing.* Experimental Mechanics, 1997. **37**(2): p. 210-215.
57. Rinne, H., *The Weibull distribution : a handbook*. 2009, Boca Raton: CRC Press http://www.crcnetbase.com/doi/pdfplus/10.1201/978142008.
58. ASTM, *C1239 Standard Practice for Reporting Uniaxial Strength Data and Estimating Weibull Distribution Parameters for Advanced Ceramics*. 2012, ASTM International: West Conshococken, PA.
59. ASTM, *C62 Standard Specification for Building Brick*. 2010, ASTM International: West Conshohocken, PA.
60. ASTM, *C216 Standard Specification for Facing Brick*. 2010, ASTM International: West Conshohocken, PA.
61. ASTM, *C902 Standard Specification for Pedestrian and Light Traffic Paving Brick*. 2011.

APPENDIX A. MECHANICAL TESTING DATA

Table A-1. Summary of compressive testing data (unpolished specimens).

Apparent Porosity	Strength (MPa)				Elastic Modulus (GPa)			
(%)	Mean	Std. Dev.	Minimum	Maximum	Mean	Std. Dev.	Minimum	Maximum
25.8038	48.2098	8.9129	30.6902	63.7022	1.3800	0.2295	0.9091	1.6986
21.3026	84.6092	16.0427	60.6869	124.5775	1.7074	0.2774	1.3033	2.0846
15.2209	127.4182	26.3390	94.1543	173.2538	1.9643	0.1954	1.6556	2.2185
8.5837	145.5767	37.8838	92.8494	224.6545	2.1628	0.4064	1.6544	3.1301
5.1337	108.0781	29.7955	46.2846	160.3382	1.9134	0.4091	1.2947	2.6577
0.8033	103.0913	38.0396	39.8364	181.7880	1.8805	0.4208	1.2489	2.8106
0.4497	135.8947	44.1752	80.1342	232.3062	2.0692	0.5145	0.7771	2.7822

Table A-2. Summary of compressive testing data (polished specimens).

Apparent Porosity	Strength (MPa)				Elastic Modulus (GPa)			
(%)	Mean	Std. Dev.	Minimum	Maximum	Mean	Std. Dev.	Minimum	Maximum
21.2498	99.7117	14.2496	85.8643	128.1575	2.6272	0.0586	2.5472	2.7183
20.6624	104.5042	6.2174	92.3891	117.7964	2.6574	0.1284	2.3354	2.8061
16.9154	134.6844	23.7728	88.3424	176.6153	2.7103	0.1366	2.3540	2.8963
5.3815	253.9701	30.5098	190.9075	298.9348	4.4550	0.1566	3.9564	4.6083
1.9528	237.2381	27.1066	196.7077	292.7745	4.5167	0.0931	4.2596	4.6151
0.8404	245.6483	28.8221	200.6868	305.3895	4.4516	0.1014	4.2467	4.6134
0.8121	245.4126	29.3053	192.5237	292.4912	4.5742	0.0656	4.4614	4.6711

Table A-3. Summary of flexural testing data (unpolished specimens).

Apparent Porosity	Strength (MPa)				Elastic Modulus (GPa)			
(%)	Mean	Std. Dev.	Minimum	Maximum	Mean	Std. Dev.	Minimum	Maximum
27.1977	12.5047	2.1269	9.6259	18.0133	1.8576	0.4395	1.3173	3.1164
22.2905	17.9515	2.5725	14.5633	22.3226	2.3954	0.4318	1.8707	3.4297
16.5186	24.4377	3.1008	19.8947	31.7271	3.5475	0.7132	2.0864	5.0349
10.1077	30.2283	3.4330	22.3979	36.3009	4.3863	0.4789	3.2450	5.1000
6.0193	37.0050	3.3047	30.1067	43.9244	5.3436	0.6135	3.4793	6.3234
1.0256	41.7520	3.6717	36.6869	50.1213	5.3717	0.7564	3.9558	7.1172
0.5436	43.3170	5.0819	27.5174	49.8960	5.2364	0.8995	3.1292	6.7480

Table A-4. Summary of flexural testing data (polished specimens).

Apparent Porosity	Strength (MPa)				Elastic Modulus (GPa)			
(%)	Mean	Std. Dev.	Minimum	Maximum	Mean	Std. Dev.	Minimum	Maximum
22.8221	17.1101	1.9094	14.1254	21.1825	5.0211	0.8697	3.3697	6.4937
16.5621	26.1376	1.6608	23.2960	29.0308	6.3135	0.6174	5.0057	7.2709
11.3108	34.2973	2.8528	29.7954	39.8830	8.4085	0.4197	7.7222	9.1204
5.8603	38.6442	1.7919	36.0137	41.9226	8.7999	0.8175	7.3724	10.4374
6.7729	40.9965	2.5525	36.7041	44.7609	9.3149	1.2023	7.9429	12.1570
0.873	42.9431	3.0041	37.6540	47.5609	8.7430	0.5459	7.7876	9.7832
0.7689	43.4502	3.8306	34.1562	49.0075	8.1787	0.5171	7.2685	9.3402

APPENDIX B. MATLAB CODE

ELASTIC MODULUS IN COMPRESSION

```
%%
% This code calculates the elastic modulus for a batch of flexure specimens.
% You will need to copy and paste this file directly into the folder that
% contains the .CSV files from the Instron testing.

%%
clear all; close all;
clc;

%% User inputs.

%{
These values are used in the chart titles and must be changed for each
batch of specimens. Add different chart titles as appropriate.
Use 3 decimal precision wherever an integer is not appropriate.
%}

batch = 187;
porosity = 1.953; % 3 decimal precision
PeakFiringTemperature = 760; % 2 decimal precision if integer not appropriate

% Used in truncating the data for elastic modulus calculations.
LL = 0.1; % Lower limit
UL = 0.9; % Upper limit

%% Importing Compressive Compliance Data
a = 'RawData_Compression_Compliance.xlsx';

SpecimenData = xlsread(a,'AluminumDisk','B3:B5');
L = SpecimenData(1); % Thickness (in)
A = SpecimenData(2); % area (in^2)
D = SpecimenData(3); % diameter (in)
AluminumModulus = 10000000; % (psi)

TestDataAl = xlsread(a,'AluminumDisk','B18:E6590');
Deflection_Total = TestDataAl(:,1);
Load = TestDataAl(:,2);
LLL = length(Load);

%% Calculating Machine Compliance
Deflection_Al = Load*L/(AluminumModulus*A);
Deflection_Machine = Deflection_Total - Deflection_Al;

% Polynomial fit
[p1,S1,mu1] = polyfit(Load,Deflection_Machine,25);

%% This sets the number of specimens.
files = dir('*.CSV');
n = length(files); % Number of raw data files in this batch
```

```
%% This calculates the porosity as a decimal value.
porosity = porosity/100;

%%
for i= 1:n
    S=int2str(i);
    filename = ['Specimen_RawData_' S '.CSV'];
    sheetname = ['Specimen_RawData_' S];
    M = xlsread(filename, sheetname,'A14:E50000');
    T = xlsread(filename, sheetname,'B3');

    M(:,4)=M(:,4)/100; % Convert from % as reported by Bluehill
    M(:,5)=M(:,5)*6.89475728; % Convert from ksi to MPa

    % Brings strain back to zero if gage length wasn't reset
    if M(1,2) ~= 0
        M(:,2) = M(:,2)-M(1,2);
        M(:,4) = M(:,2)/T;
        M(1,4) = 0;
    end

    % Plot stress-strain curve
    figure(1)
    hold all

    plot(M(:,4),M(:,5));
    axis tight
    xlabel('Strain', 'FontSize',10.5, 'FontWeight', 'bold');
    ylabel('Stress (MPa)','FontSize',10.5, 'FontWeight', 'bold');
    title(sprintf('Peak Firing Temperature = %0.1f \\circC, Apparent Porosity
    = %0.3f', PeakFiringTemperature , porosity))

    if i==n
        set(gca,'fontsize',10)
        set(gcf, 'paperunits', 'inches', 'paperposition', [0 0 5 3.5])
        timestamp = datestr(now,'yyyymmdd_HHMMSS');
        b = int2str(batch);
        fname = 'C:\Users\EnVitrum\Desktop\Random Matlab Figures';
        filename = ['B' b ' CompStressStrain_' timestamp];
        print(fullfile(fname,filename), '-dtiff', '-r600')
        saveas(gcf,fullfile(fname,filename),'fig')
    end


    % Compliance correction

    Deflection_Machine2 = polyval(p1,M(:,3),[],mu1);
    Deflection_Actual = M(:,2) - Deflection_Machine2;
    Strain_Actual = Deflection_Actual./T;
    M(:,4) = Strain_Actual;

   % Removing catastrophic failures
    [C,I] = max(M(:,5));
    if C < 10/6.89475728;
        M = ones(I,5);
```

```
end

% removing all data after UL% of maximum is reached.
for j= 1:length(M)
    if M(j,5) > C * UL
       k=j;
       break
    end
end
M = M(1:k,1:5);

% Plot stress-strain curve w/ compliance correction
figure(2)
hold all
plot(M(:,4),M(:,5))
axis tight
xlabel('Strain', 'FontSize',10.5, 'FontWeight', 'bold');
ylabel('Stress (MPa)','FontSize',10.5, 'FontWeight', 'bold');
title(sprintf('Peak Firing Temperature = %0.1f \\circC, Apparent Porosity
= %0.3f', PeakFiringTemperature , porosity))
axessize = axis; % gives min/max of x/y axes to use in subsequent plot

if i==n
    set(gca,'fontsize',10)
    set(gcf, 'paperunits', 'inches', 'paperposition', [0 0 5 3.5])
    timestamp = datestr(now,'yyyymmdd_HHMMSS');
    fname = 'C:\Users\EnVitrum\Desktop\Random Matlab Figures';
    filename = ['B' b ' CompStressStrain_Compliance_' timestamp];
    print(fullfile(fname,filename), '-dtiff', '-r600')
    saveas(gcf,fullfile(fname,filename),'fig')
end

% removing all data when stress is less than (LL*100)% of maximum.
for j = 1:length(M)
    if M(1,5) < C * LL
        M(1,:)=[];
    else
        break
    end
end


% Plot "linear" portion of the stress-strain curve
figure(3)
hold all
plot(M(:,4),M(:,5))
axis(axessize)
xlabel('Strain', 'FontSize',10.5, 'FontWeight', 'bold');
ylabel('Stress (MPa)','FontSize',10.5, 'FontWeight', 'bold');
title(sprintf('Peak Firing Temperature = %0.1f \\circC, Apparent Porosity
= %0.3f', PeakFiringTemperature , porosity))

if i==n
    set(gca,'fontsize',10)
    set(gcf, 'paperunits', 'inches', 'paperposition', [0 0 5 3.5])
```

```
        timestamp = datestr(now,'yyyymmdd_HHMMSS');
        fname = 'C:\Users\EnVitrum\Desktop\Random Matlab Figures';
        filename = ['B' b ' CompStressStrain_Truncated_' timestamp];
        print(fullfile(fname,filename), '-dtiff', '-r600')
        saveas(gcf,fullfile(fname,filename),'fig')
    end

    % calculate the compressive Modulus
    p = polyfit(M(:,4),M(:,5),1);

    % Calculate R^2
    y = polyval(p, M(:,4));
    yresid = M(:,5) - y;
    SSresid = sum(yresid.^2);
    SStotal = (length(M(:,5))-1) * var(M(:,5));
    rsq = 1 - SSresid/SStotal;

    CompMod(i,1) = p(1);
    CompMod(i,2) = rsq;
 %}
end

format long g
CompMod(:,1) % This is a vector that contains the elastic moduli.
CompMod(:,2) % This is a vector that contains the R^2 values.

Rsqr = mean(CompMod(:,2)) % This is the avg. R^2 value.
```

ELASTIC MODULUS IN FLEXURE

```
%%
% This code calculates the elastic modulus for a batch of flexure specimens.
% You will need to copy and paste this file directly into the folder that
% contains the .CSV files from the Instron testing.

%%
clear all; close all;
clc;

%% User inputs.

%{
These values are used in the chart titles and must be changed for each
batch of specimens. Add different chart titles as appropriate.
Use 3 decimal precision wherever an integer is not appropriate.
%}

batch = 193;
porosity = 5.860; % 3 decimal precision
PeakFiringTemperature = 746.11; % 2 decimal precision

% Used in truncating the data for elastic modulus calculations.
LL = 0.2; % Lower limit
UL = 0.95; % Upper limit

%% Importing Flexural Compliance Data
a = 'Summary_of_Instron_Flexure_Compliance.xlsx';

SpecimenData = xlsread(a,'2nd_Test','B3:B5');
L = SpecimenData(1); % span length (in)
d = SpecimenData(2); % thickness (in)
b = SpecimenData(3); % width (in)
AluminumModulus = 1000000; % (psi)

TestDataAl = xlsread(a,'2nd_Test','B17:E559');
Deflection_Total = TestDataAl(:,1);
Load = TestDataAl(:,2);
Strain_Total = TestDataAl(:,3);
Stress = TestDataAl(:,4);

%% Calculating Machine Compliance
Deflection_Al = L^3*Load/(4*b*d^3*AluminumModulus);
Deflection_Machine = Deflection_Total - Deflection_Al;

% Polynomial fit
[p1,S1,mu1] = polyfit(Load,Deflection_Machine,45);


%% This sets the number of specimens.
files = dir('*.CSV');
n = length(files); % Number of raw data files in this batch
```

```
%% This calculates the porosity as a decimal value.
porosity = porosity/100;

%%
for i= 1:n
    S=int2str(i);
    filename = ['Specimen_RawData_' S '.CSV'];
    sheetname = ['Specimen_RawData_' S];
    M = xlsread(filename, sheetname,'A10:E350');
    T = xlsread(filename, sheetname,'B3:B4');

    M(:,4)=M(:,4)/100; % Convert from % as reported by Bluehill
    M(:,5)=M(:,5)*6.89475728; % Convert from ksi to MPa

    % Brings strain back to zero if gage length wasn't reset
    if M(1,2) ~= 0
        M(:,2) = M(:,2)-M(1,2);
        M(:,4) = M(:,2)*T(2)*6/(T(1)^2);
        M(1,4) = 0;
    end

    % Plot stress-strain curve
    figure(1)
    hold all

    plot(M(:,4),M(:,5));
    axis tight
    xlabel('Strain', 'FontSize',10.5, 'FontWeight', 'bold');
    ylabel('Stress (MPa)','FontSize',10.5, 'FontWeight', 'bold');
     title(sprintf('Peak Firing Temperature = %0.1f \\circC, Apparent Porosity
     = %0.3f', PeakFiringTemperature , porosity))


    if i==n
        set(gca,'fontsize',10)
        set(gcf, 'paperunits', 'inches', 'paperposition', [0 0 5 3.5])
        timestamp = datestr(now,'yyyymmdd_HHMMSS');
        b = int2str(batch);
        fname = 'C:\Users\EnVitrum\Desktop\Random Matlab Figures';
        filename = ['B' b ' FlexStressStrain_' timestamp];
        print(fullfile(fname,filename), '-dtiff', '-r600')
        saveas(gcf,fullfile(fname,filename),'fig')
    end

    % Compliance correction
    Deflection_Machine2 = polyval(p1,M(:,3),[],mu1);
    Deflection_Actual = M(:,2) - Deflection_Machine2;
    Strain_Actual = 6*Deflection_Actual*d/L^2;
    M(:,4) = Strain_Actual;

    % removing all data after failure
    [C,I] = max(M(:,5));% finding index value at max stress
    M = M(1:I,1:5);

    % Plot stress-strain curve w/ compliance correction
```

```
figure(2)
hold all
plot(M(:,4),M(:,5))
axis tight
xlabel('Strain', 'FontSize',10.5, 'FontWeight', 'bold');
ylabel('Stress (MPa)','FontSize',10.5, 'FontWeight', 'bold');
title(sprintf('Peak Firing Temperature = %0.1f \\circC, Apparent Porosity
= %0.3f', PeakFiringTemperature , porosity))

if i==n
    set(gca,'fontsize',10)
    set(gcf, 'paperunits', 'inches', 'paperposition', [0 0 5 3.5])
    timestamp = datestr(now,'yyyymmdd_HHMMSS');
    fname = 'C:\Users\EnVitrum\Desktop\Random Matlab Figures';
    filename = ['B' b ' FlexStressStrain_Compliance_' timestamp];
    print(fullfile(fname,filename), '-dtiff', '-r600')
    saveas(gcf,fullfile(fname,filename),'fig')
end

% removing all data when stress is less than (LL*100)% of maximum.
for j = 1:length(M)
    if M(1,5) < C * LL
        M(1,:)=[];
    else
        break
    end
end
%}

% Plot "linear" portion of the stress-strain curve
figure(3)
hold all
plot(M(:,4),M(:,5))
axis(axessize)
xlabel('Strain', 'FontSize',10.5, 'FontWeight', 'bold');
ylabel('Stress (MPa)','FontSize',10.5, 'FontWeight', 'bold');
title(sprintf('Peak Firing Temperature = %0.1f \\circC, Apparent Porosity
= %0.3f', PeakFiringTemperature , porosity))

if i==n
    set(gca,'fontsize',10)
    set(gcf, 'paperunits', 'inches', 'paperposition', [0 0 5 3.5])
    timestamp = datestr(now,'yyyymmdd_HHMMSS');
    fname = 'C:\Users\EnVitrum\Desktop\Random Matlab Figures';
    filename = ['B' b ' FlexStressStrain_Truncated_' timestamp];
    print(fullfile(fname,filename), '-dtiff', '-r600')
    saveas(gcf,fullfile(fname,filename),'fig')
end

% calculate the flexural Modulus
p = polyfit(M(:,4),M(:,5),1);

% Calculate R^2
y = polyval(p, M(:,4));
yresid = M(:,5) - y;
SSresid = sum(yresid.^2);
```

```
    SStotal = (length(M(:,5))-1) * var(M(:,5));
    rsq = 1 - SSresid/SStotal;

    FlexMod(i,1) = p(1);
    FlexMod(i,2) = rsq;

end

format long g
FlexMod(:,1) % This is a vector that contains the elastic moduli.
FlexMod(:,2) % This is a vector that contains the R^2 values.

Rsqr = mean(FlexMod(:,2)) % This is the avg. R^2 value.
```

WEIBULL CODE

MAIN CODE

```
%% Description

% This code takes compression or flexure data from the spreadsheets and
% performs statistical calculations using the Weibull Distribution.
% This file must be in the same folder as the spreadsheet you are
% analyzing.

%%
clear all; close all;
clc;

%% User inputs.

% The code below pulls porosity and flexure or compression data from the
spreadsheet you specify below.

% Importing data from Excel file
a = '2015.07.24_235.xlsx'; % Change this as necessary.

%{
Uncomment the appropriate 3 lines of code below.
Make sure the other 3 sections (each containing 3 lines of code) are
commented out.
Make sure to relabel the graphs when you switch between flexure and
compression.
%}


data = importTestData(a,'Compression','A5:G24');
%data = importTestData(a,'Compression','A5:G19'); % Just for Batch 235
Porosity = importTestData(a,'Porosity & Density', 'B14:C14');
%Porosity = importTestData(a,'Porosity & Density by Set #', 'B14:C14'); %
Just for Batch 235
FormationPressure = importTestData(a, 'Press Force', 'F25:F27');
PeakFiringTemperature = importTestData(a, 'Conditions', 'C16:D16');
%}

%{
data = importTestData(a,'Flexure','A5:G24');
Porosity = importTestData(a,'Porosity & Density', 'B14:C14');
FormationPressure = importTestData(a, 'Press Force', 'F25:F27');
PeakFiringTemperature = importTestData(a, 'Conditions', 'C16:D16');
%}

% Pulls the Batch Number from the spreadsheet.
Batch = importTestData(a,'Conditions','A1:B1');
Batch = (Batch(2));
%% Calculations
%data(2,:)=[]
%data(10,:)=[]
%data(16,:)=[]
```

```
% Reports porosity as a decimal rather than a percentage.
P = Porosity(1)/100;

% Stores data in vectors.
Specimen = data(:,1);
MaxExt = data(:,2);
MaxLoad = data(:,3);
MaxStrain = data(:,4);
MaxStress = data(:,5);
MaxStress_SI = data(:,5)*0.00689475728; % Conversion from psi to MPa
Modulus = data(:,7);

% Removing untested specimens
MaxExt(MaxExt==0)=[];
MaxLoad(MaxLoad==0)=[];
MaxStrain(MaxStrain==0)=[];
MaxStress(MaxStress==0)=[];
MaxStress_SI(MaxStress_SI==0)=[];
Modulus(Modulus==0)=[];

% Calculates statistics based on Weibull Distribution.
[x1,y1,z1] = WeibullFunction(MaxStress);

[xsi,ysi,zsi] = WeibullFunction(MaxStress_SI);

[x2,y2,z2] = WeibullFunction(Modulus);


%% Plots

figure (1)
plot(ysi(:,1),ysi(:,2),'bx');
hold on
plot(zsi(:,1),zsi(:,2),'r-',zsi(:,1),zsi(:,3),'r:',zsi(:,1),zsi(:,4),'r:');
hold off

title(sprintf('Peak Firing Temperature = %0.1f \\circC, Apparent Porosity =
%0.3f',PeakFiringTemperature(2), P))
xlabel('Compressive Strength (MPa)','FontSize',10.25, 'FontWeight', 'bold');
%xlabel('Transverse Strength (MPa)','FontSize',10.25, 'FontWeight', 'bold');
ylabel('Probability of Failure','FontSize',10.5, 'FontWeight', 'bold');

set(gca,'fontsize',10)
set(gcf, 'paperunits', 'inches', 'paperposition', [0 0 5 3.5])
timestamp = datestr(now,'yyyymmdd_HHMMSS');
b = int2str(Batch);
fname = 'C:\Users\EnVitrum\Desktop\Random Matlab Figures';
filename = ['B' b ' CompStrength' timestamp];
%filename = ['B' b ' FlexStrength' timestamp];
print(fullfile(fname,filename), '-dtiff', '-r600')
saveas(gcf,fullfile(fname,filename),'fig')
```

```
figure (2)
plot(y2(:,1),y2(:,2),'bx');
hold on
plot(z2(:,1),z2(:,2),'r-',z2(:,1),z2(:,3),'r:',z2(:,1),z2(:,4),'r:');
hold off
title(sprintf('Peak Firing Temperature = %0.1f \\circC, Apparent Porosity =
%0.3f',PeakFiringTemperature(2), P))
xlabel('Elastic Modulus in Compression (MPa)','FontSize',10.25, 'FontWeight',
'bold'); %
%xlabel('Elastic Modulus in Flexure (MPa)','FontSize',10.25, 'FontWeight',
'bold');
ylabel('Probability','FontSize',10.5, 'FontWeight', 'bold');

set(gca,'fontsize',10)
set(gcf, 'paperunits', 'inches', 'paperposition', [0 0 5 3.5])
timestamp = datestr(now,'yyyymmdd_HHMMSS');
fname = 'C:\Users\EnVitrum\Desktop\Random Matlab Figures';
filename = ['B' b ' CompModulus_' timestamp];
%filename = ['B' b ' FlexModulus_' timestamp];
print(fullfile(fname,filename), '-dtiff', '-r600')
saveas(gcf,fullfile(fname,filename),'fig')

figure (3)
wblplot(MaxStress_SI)
title(sprintf('Peak Firing Temperature = %0.1f \\circC, Apparent Porosity =
%0.3f',PeakFiringTemperature(2), P))
xlabel('Compressive Strength (MPa)','FontSize',10.25, 'FontWeight', 'bold');
%xlabel('Transverse Strength (MPa)','FontSize',10.25, 'FontWeight', 'bold');
ylabel('Probability of Failure','FontSize',10.25, 'FontWeight', 'bold');

set(gca,'fontsize',10)
set(gcf, 'paperunits', 'inches', 'paperposition', [0 0 5 3.5])
timestamp = datestr(now,'yyyymmdd_HHMMSS');
fname = 'C:\Users\EnVitrum\Desktop\Random Matlab Figures';
filename = ['B' b ' CompProbability_' timestamp];
%filename = ['B' b ' FlexProbability_' timestamp];
print(fullfile(fname,filename), '-dtiff', '-r600')
saveas(gcf,fullfile(fname,filename),'fig')

%%
format long g

fprintf('Here are the Weibull mean, variance, scale factor and Weibull
modulus for Stress (psi).\n')
stressstats = x1
fprintf('Here are the Weibull mean, variance, scale factor and Weibull
modulus for the Elastic Modulus (GPa).\n')
modulusstats = x2
%fprintf('Here are the Weibull mean, variance, scale factor and Weibull
modulus for Stress (MPa).\n')
%stressstats_SI = xsi %Gives you the Weibull mean, variance and parameters
for the Stress (MPa)
```

WEIBULL FUNCTION

```
function [WeibullValues, Weibull_emp, Weibull_CI] = WeibullFunction(data)

[empF,x,empFlo,empFup] = ecdf(data); % Calculates empirical CDF

% Estimating Weibull parameters (2-param method: paramEsts(1)==scale factor;
paramsEsts(2)==shape factor)
paramEsts = wblfit(data);
[mean,variance] = wblstat(paramEsts(1),paramEsts(2));

% Fitting the Weibull distribution to the data
[nlogl,paramCov] = wbllike(paramEsts,data);
Max = 1.5*max(data); % Setting maximum x-axis value
xx = linspace(1,Max,500); % Generating vector for Weibull model
alpha = 0.05; % Confidence interval = (1 - alpha)
[wblF,wblFlo,wblFup] = wblcdf(xx,paramEsts(1),paramEsts(2),paramCov, alpha);

WeibullValues(1,1) = mean;
WeibullValues(2,1) = variance;
WeibullValues(3,1) = paramEsts(1); % Scale Factor
WeibullValues(4,1) = paramEsts(2); % Shape Factor

x(1,:)=[];
empF(1,:)=[];
empFlo(1,:)=[];
empFup(1,:)=[];
nn=length(x);
x(nn,:)=[];
empF(nn,:)=[];
empFlo(nn,:)=[];
empFup(nn,:)=[];

Weibull_emp(:,1) = x;
Weibull_emp(:,2) = empF;
Weibull_emp(:,3) = empFlo;
Weibull_emp(:,4) = empFup;

Weibull_CI(:,1) = xx;
Weibull_CI(:,2) = wblF;
Weibull_CI(:,3) = wblFlo;
Weibull_CI(:,4) = wblFup;
```

POROSITY-PROPERTY MODELING

DUCKWORTH

```
%% Raw data

% Polished compression
porosity = [21.2498, 20.6624, 16.9154, 5.3815, 1.9528, 0.8404, 0.8121,
0]./100;
stress = [99.1981, 104.1739, 134.6681, 254.5172, 236.3286, 245.0149,
245.2810, 2500];
name = 'Comp_Pol_';
%}

%% Initialization.

% Initialize arrays to store fits and goodness-of-fit.
fitresult = cell( 2, 1 );
gof = struct( 'sse', cell( 2, 1 ), ...
    'rsquare', [], 'dfe', [], 'adjrsquare', [], 'rmse', [] );

%% Fit: 'Exponential'.
[xData, yData] = prepareCurveData(porosity, stress);

% Set up fittype and options.
ft = fittype( '2500*exp(-a*x)', 'independent', 'x', 'dependent', 'y' );
opts = fitoptions( ft );
opts.Display = 'Off';
opts.Lower = -Inf;
opts.StartPoint = 0.959291425205444;
opts.Upper = Inf;

% Fit model to data.
[fitresult{1}, gof(1)] = fit( xData, yData, ft, opts );

% Plot fit with data.
figure( 'Name', 'Exponential' );
h = plot( fitresult{1}, xData, yData, 'predobs' );
legend( h, 'Experimental Data', 'Exponential', 'Lower bounds (Exponential)',
'Upper bounds (Exponential)', 'Location', 'NorthEast' );

% Label axes
axis([0 .30 0 3000]);
xlabel( 'Apparent Porosity','FontSize', 10.5, 'FontWeight', 'bold' );
ylabel( 'Compressive Strength (MPa)','FontSize', 10.5,'FontWeight', 'bold' );

set(gca,'fontsize',10)
set(gcf, 'paperunits', 'inches', 'paperposition', [0 0 5 3.5])
timestamp = datestr(now,'yyyymmdd_HHMMSS');
filename = ['Exponential_' name timestamp];
print(filename, '-dtiff', '-r600')
saveas(gcf,filename,'fig')
```

```
%% Raw Data

% Polished Compression
Rdensity =
[1.8461,1.9016,2.0601,2.1163,2.1338,2.0658,2.0795,2.496666667]'/2.496666667;
stress =
[99.1981,104.1739,134.6681,254.5172,236.3286,245.0149,245.2810,2500]';
timestamp = datestr(now,'yyyymmdd_HHMMSS');
name = '_Pol_';
%}

[xData, yData] = prepareCurveData( Rdensity, stress );


%% Initialization.

% Initialize arrays to store fits and goodness-of-fit.
fitresult = cell( 3, 1 );
gof = struct( 'sse', cell( 3, 1 ), ...
    'rsquare', [], 'dfe', [], 'adjrsquare', [], 'rmse', [] );

%% Fit: 'Gibson - Open_Density Correction'.

% Set up fittype and options.
ft = fittype( '2500*a*x^(3/2)*(1+x^.5)', 'independent', 'x', 'dependent', 'y'
);
opts = fitoptions( ft );
opts.Display = 'Off';
opts.Lower = 0;
opts.StartPoint = 0;
opts.Upper = Inf;

% Fit model to data.
[fitresult{1}, gof(1)] = fit( xData, yData, ft, opts );

% Plot fit with data.
figure( 'Name', 'Gibson - Open_High Density' );
h = plot( fitresult{1}, xData, yData, 'predobs' );
legend( h, 'stress vs. Rdensity', 'Gibson - Open (Density Correction)',
'Lower bounds', 'Upper bounds', 'Location', 'NorthEast' );

% Label axes
axis([0 1 0 3000]);
xlabel( 'Relative Density' );
ylabel( 'stress' );

set(gca,'fontsize',10)
set(gcf, 'paperunits', 'inches', 'paperposition', [0 0 5 3.5])
filename = ['CompStrength_GAopen_HighDensity' name timestamp];
print(filename, '-dtiff', '-r600')
saveas(gcf,filename,'fig')
```

```
%% Fit: 'Gibson - Open'.

% Set up fittype and options.
ft = fittype( '2500*a*x^(3/2)', 'independent', 'x', 'dependent', 'y' );
opts = fitoptions( ft );
opts.Display = 'Off';
opts.Lower = 0;
opts.StartPoint = 0.0318328463774207;
opts.Upper = Inf;

% Fit model to data.
[fitresult{2}, gof(2)] = fit( xData, yData, ft, opts );

% Plot fit with data.
figure( 'Name', 'Gibson - Open' );
h = plot( fitresult{2}, xData, yData, 'predobs' );
legend( h, 'stress vs. Rdensity', 'Gibson - Open', 'Lower bounds', 'Upper
bounds', 'Location', 'NorthEast' );

% Label axes
axis([0 1 0 3000]);
xlabel( 'Relative Density' );
ylabel( 'stress' );

set(gca,'fontsize',10)
set(gcf, 'paperunits', 'inches', 'paperposition', [0 0 5 3.5])
filename = ['CompStrength_GAopen' name timestamp];
print(filename, '-dtiff', '-r600')
saveas(gcf,filename,'fig')


%% Fit: 'Gibson - Closed'.

% Set up fittype and options.
ft = fittype( '2500*a*(c*x)^(3/2)+b*(1-c)*x', 'independent', 'x',
'dependent', 'y' );
opts = fitoptions( ft );
opts.Display = 'Off';
opts.Lower = [0 0 0];
opts.StartPoint = [0.392227019534168 0.655477890177557 0.171186687811562];
opts.Upper = [Inf Inf 1];

% Fit model to data.
[fitresult{3}, gof(3)] = fit( xData, yData, ft, opts );

% Plot fit with data.
figure( 'Name', 'Gibson - Closed' );
h = plot( fitresult{3}, xData, yData, 'predobs' );
legend( h, 'stress vs. Rdensity', 'Gibson - Closed', 'Lower bounds', 'Upper
bounds', 'Location', 'NorthEast' );

% Label axes
axis([0 1 0 3000]);
xlabel( 'Relative Density' );
ylabel( 'stress' );
```

```
set(gca,'fontsize',10)
set(gcf, 'paperunits', 'inches', 'paperposition', [0 0 5 3.5])
filename = ['CompStrength_GAclosed' name timestamp];
print(filename, '-dtiff', '-r600')
saveas(gcf,filename,'fig')

%%
fitresult_open1 = fitresult{1}
gof1_open1 = gof(1)
fitresult2_open2 = fitresult{2}
gof2_open2 = gof(2)
fitresult3_closed = fitresult{3}
gof3_closed = gof(3)
```

NIELSEN

```
%% Raw Data

% Polished, Gaussian, 2 ton, elastic modulus in flexure
porosity = [22.8221, 16.5621, 11.3108, 5.8603, 6.7729, 0.8730, 0.7689,
0]'./100;
modulus = [5.0231, 6.3153, 8.3974, 8.7821, 9.2661, 8.7306, 8.1508];
modulus = [modulus 70.420]';
yaxistitle = 'Elastic Modulus in Flexure (GPa)';
timestamp = datestr(now,'yyyymmdd_HHMMSS');
filename = ['Nielsen_Flex_Pol_' timestamp];
%}

[xData, yData] = prepareCurveData( porosity, modulus );

%% Initialization.
clear all; close all; clc;

% Initialize arrays to store fits and goodness-of-fit.
fitresult = cell( 9, 1 );
gof = struct( 'sse', cell( 9, 1 ), ...
    'rsquare', [], 'dfe', [], 'adjrsquare', [], 'rmse', [] );

%% Set up fittype and options.

ft = fittype( '70.420*(1-x)/(1+x/(m_o*(1-x)))', 'independent', 'x',
'dependent', 'y' );
opts = fitoptions( ft );
opts.Display = 'Off';
opts.Lower = 0;
opts.StartPoint = 0.5;
opts.Upper = 1;

% Fit model to data.
[fitresult{1}, gof(1)] = fit( xData, yData, ft, opts );

% Plot fit with data.
figure( 'Name', 'Nielsen' );
h = plot( fitresult{1}, xData, yData, 'predobs' );
legend( h, 'Experimental Data', 'Nielsen', 'Lower bounds (Nielsen)', 'Upper
bounds (Nielsen)', 'Location', 'NorthEast' );

% Label axes
axis([0 .25 0 80]);
xlabel( 'Apparent Porosity','FontSize', 10.5, 'FontWeight', 'bold' );
ylabel( yaxistitle ,'FontSize', 10.5,'FontWeight', 'bold' );

set(gca,'fontsize',10)
set(gcf, 'paperunits', 'inches', 'paperposition', [0 0 5 3.5])
print(filename, '-dtiff', '-r600')
saveas(gcf,filename,'fig')
```

```
%% Raw Data

% Polished, elastic modulus in compression
porosity = [21.2498, 20.6624, 16.9154, 5.3815, 1.9528, 0.8404, 0.8121,
0]'./100;
modulus = [2.6264, 2.6632, 2.7128, 4.4617, 4.5210, 4.4505, 4.5740];
modulus = [modulus 70.420]';
yaxistitle = 'Elastic Modulus in Compression (GPa)';
%}

[xData, yData] = prepareCurveData(porosity, modulus );


%% Initialization.
clear all; close all; clc;

% Initialize arrays to store fits and goodness-of-fit.
fitresult = cell( 9, 1 );
gof = struct( 'sse', cell( 9, 1 ), ...
    'rsquare', [], 'dfe', [], 'adjrsquare', [], 'rmse', [] );


%% Fit: 'Hasselman'.
% Set up fittype and options.
ft = fittype( '70.420*(1-(a*x)/(1+(a-1)*x))', 'independent', 'x',
'dependent', 'y' );
opts = fitoptions( ft );
opts.Display = 'Off';
opts.Lower = -Inf;
opts.StartPoint = 0.568823660872193;
opts.Upper = Inf;

% Fit model to data.
[fitresult{1}, gof(1)] = fit( xData, yData, ft, opts );

% Plot fit with data.
figure( 'Name', 'Hasselman' );
h = plot( fitresult{1}, xData, yData, 'predobs' );
legend( h, 'Experimental Data', 'Hasselman', 'Lower bounds (Hasselman)',
'Upper bounds (Hasselman)', 'Location', 'NorthEast' );

% Label axes
axis([0 .25 0 80]);
xlabel( 'Apparent Porosity','FontSize', 10.5, 'FontWeight', 'bold' );
ylabel( yaxistitle ,'FontSize', 10.5,'FontWeight', 'bold' );

set(gca,'fontsize',10)
set(gcf, 'paperunits', 'inches', 'paperposition', [0 0 5 3.5])
timestamp = datestr(now,'yyyymmdd_HHMMSS');
filename = ['Hasselman_' timestamp];
print(filename, '-dtiff', '-r600')
```

```
saveas(gcf,filename,'fig')
%}
%% Fit: 'Brown - Biddulph - Wilcox'.
% Set up fittype and options.
ft = fittype( '70.420*(1-a*x^(2/3))', 'independent', 'x', 'dependent', 'y' );
opts = fitoptions( ft );
opts.Display = 'Off';
opts.Lower = -Inf;
opts.StartPoint = 0.616044676146639;
opts.Upper = Inf;

% Fit model to data.
[fitresult{2}, gof(2)] = fit( xData, yData, ft, opts );

% Plot fit with data.
figure( 'Name', 'Brown - Biddulph - Wilcox' );
h = plot( fitresult{2}, xData, yData, 'predobs' );
legend( h, 'Experimental Data', 'Brown - Biddulph - Wilcox', 'Lower bounds
(Brown - Biddulph - Wilcox)', 'Upper bounds (Brown - Biddulph - Wilcox)',
'Location', 'NorthEast' );

% Label axes
axis([0 .25 0 80]);
xlabel( 'Apparent Porosity','FontSize', 10.5, 'FontWeight', 'bold' );
ylabel( yaxistitle ,'FontSize', 10.5,'FontWeight', 'bold' );

set(gca,'fontsize',10)
set(gcf, 'paperunits', 'inches', 'paperposition', [0 0 5 3.5])
timestamp = datestr(now,'yyyymmdd_HHMMSS');
filename = ['Brown - Biddulph - Wilcox_' timestamp];
print(filename, '-dtiff', '-r600')
saveas(gcf,filename,'fig')
%}

%% Fit: 'Phani - Niyogi'.
% Set up fittype and options.
ft = fittype( '70.420*(1-a*x)^n', 'independent', 'x', 'dependent', 'y' );
opts = fitoptions( ft );
opts.Display = 'Off';
opts.Lower = [1 -Inf];
opts.StartPoint = [1.425 1];
opts.Upper = [3.85 Inf];

% Fit model to data.
[fitresult{3}, gof(3)] = fit( xData, yData, ft, opts );
fitobject = fit( xData, yData, ft, opts );

% Plot fit with data.
figure( 'Name', 'Phani - Niyogi' );
h = plot( fitresult{3}, xData, yData, 'predobs' );
legend( h, 'Experimental Data', 'Phani - Niyogi', 'Lower bounds (Phani -
Niyogi)', 'Upper bounds (Phani - Niyogi)', 'Location', 'NorthEast' );

% Label axes
axis([0 .25 0 80]);
```

```
xlabel( 'Apparent Porosity','FontSize', 10.5, 'FontWeight', 'bold' );
ylabel( yaxistitle ,'FontSize', 10.5,'FontWeight', 'bold' );

set(gca,'fontsize',10)
set(gcf, 'paperunits', 'inches', 'paperposition', [0 0 5 3.5])
timestamp = datestr(now,'yyyymmdd_HHMMSS');
filename = ['Phani - Niyogi_' timestamp];
print(filename, '-dtiff', '-r600')
saveas(gcf,filename,'fig')

%}

%% Fit: 'Hashin'.
% Set up fittype and options.
ft = fittype( '70.420*(1-x)/(1+(1+v)*(13-15*v)/(2*(7-5*v))*x)',
'independent', 'x', 'dependent', 'y' );
opts = fitoptions( ft );
opts.Display = 'Off';
opts.Lower = 0.21;
opts.StartPoint = 0.22;
opts.Upper = 0.24;

% Fit model to data.
[fitresult{4}, gof(4)] = fit( xData, yData, ft, opts );

% Plot fit with data.
figure( 'Name', 'Hashin' );
h = plot( fitresult{4}, xData, yData);%, 'predobs' );
legend( h, 'Experimental Data', 'Hashin');%, 'Lower bounds (Hashin)', 'Upper
bounds (Hashin)', 'Location', 'NorthEast' );

% Label axes
axis([0 .25 0 80]);
xlabel( 'Apparent Porosity','FontSize', 10.5, 'FontWeight', 'bold' );
ylabel( yaxistitle ,'FontSize', 10.5,'FontWeight', 'bold' );

set(gca,'fontsize',10)
set(gcf, 'paperunits', 'inches', 'paperposition', [0 0 5 3.5])
timestamp = datestr(now,'yyyymmdd_HHMMSS');
filename = ['Hashin_' timestamp];
print(filename, '-dtiff', '-r600')
saveas(gcf,filename,'fig')
%}

%% Fit: 'Spriggs'.
% Set up fittype and options.
ft = fittype( '70.420*exp(-b*x)', 'independent', 'x', 'dependent', 'y' );
opts = fitoptions( ft );
opts.Display = 'Off';
opts.Lower = -Inf;
opts.StartPoint = 0.145538980384717;
opts.Upper = Inf;

% Fit model to data.
[fitresult{5}, gof(5)] = fit( xData, yData, ft, opts );
```

```
% Plot fit with data.
figure( 'Name', 'Spriggs' );
h = plot( fitresult{5}, xData, yData, 'predobs' );
legend( h, 'Experimental Data', 'Spriggs', 'Lower bounds (Spriggs)', 'Upper
bounds (Spriggs)', 'Location', 'NorthEast' );

% Label axes
axis([0 .25 0 80]);
xlabel( 'Apparent Porosity','FontSize', 10.5, 'FontWeight', 'bold' );
ylabel( yaxistitle ,'FontSize', 10.5,'FontWeight', 'bold' );

set(gca,'fontsize',10)
set(gcf, 'paperunits', 'inches', 'paperposition', [0 0 5 3.5])
timestamp = datestr(now,'yyyymmdd_HHMMSS');
filename = ['Spriggs_' timestamp];
print(filename, '-dtiff', '-r600')
saveas(gcf,filename,'fig')
%}

%% Fit: 'Ramakrishnan'.
% Set up fittype and options.
ft = fittype( '70.420*(1-x)^2/(1+(2-3*v)*x)', 'independent', 'x',
'dependent', 'y' );
opts = fitoptions( ft );
opts.Display = 'Off';
opts.Lower = 0.21;
opts.StartPoint = 0.22;
opts.Upper = 0.24;

% Fit model to data.
[fitresult{6}, gof(6)] = fit( xData, yData, ft, opts );

% Plot fit with data.
figure( 'Name', 'Ramakrishnan' );
h = plot( fitresult{6}, xData, yData); %, 'predobs' );
legend( h, 'Experimental Data', 'Ramakrishnan');%, 'Lower bounds
(Ramakrishnan)', 'Upper bounds (Ramakrishnan)', 'Location', 'NorthEast' );

% Label axes
axis([0 .25 0 80]);
xlabel( 'Apparent Porosity','FontSize', 10.5, 'FontWeight', 'bold' );
ylabel( yaxistitle ,'FontSize', 10.5,'FontWeight', 'bold' );

set(gca,'fontsize',10)
set(gcf, 'paperunits', 'inches', 'paperposition', [0 0 5 3.5])
timestamp = datestr(now,'yyyymmdd_HHMMSS');
filename = ['Ramakrishnan_' timestamp];
print(filename, '-dtiff', '-r600')
saveas(gcf,filename,'fig')
%}

%% Fit: 'Wagh-Poeppel-Singh'.
% Set up fittype and options.
ft = fittype( '70.420*(1-x)^n', 'independent', 'x', 'dependent', 'y' );
```

```
opts = fitoptions( ft );
opts.Display = 'Off';
opts.Lower = -Inf;
opts.StartPoint = 1;
opts.Upper = Inf;

% Fit model to data.
[fitresult{7}, gof(7)] = fit( xData, yData, ft, opts );

% Plot fit with data.
figure( 'Name', 'Wagh-Poeppel-Singh' );
h = plot( fitresult{7}, xData, yData, 'predobs' );
legend( h, 'Experimental Data', 'Wagh-Poeppel-Singh', 'Lower bounds (Wagh-
Poeppel-Singh)', 'Upper bounds (Wagh-Poeppel-Singh)', 'Location', 'NorthEast'
);

% Label axes
axis([0 .25 0 80]);
xlabel( 'Apparent Porosity','FontSize', 10.5, 'FontWeight', 'bold' );
ylabel( yaxistitle ,'FontSize', 10.5,'FontWeight', 'bold' );

set(gca,'fontsize',10)
set(gcf, 'paperunits', 'inches', 'paperposition', [0 0 5 3.5])
timestamp = datestr(now,'yyyymmdd_HHMMSS');
filename = ['Wagh-Poeppel-Singh_' timestamp];
print(filename, '-dtiff', '-r600')
saveas(gcf,filename,'fig')
%}

%% Fit: 'Wang'.


% Set up fittype and options.
ft = fittype( '70.420*exp(-(b*x+c*x^2 ))', 'independent', 'x', 'dependent',
'y' );
opts = fitoptions( ft );
opts.Display = 'Off';
opts.Lower = [-Inf -Inf];
opts.StartPoint = [0.956134540229802 0.575208595078466];
opts.Upper = [Inf Inf];

% Fit model to data.
[fitresult{8}, gof(8)] = fit( xData, yData, ft, opts );

% Plot fit with data.
figure( 'Name', 'Wang' );
h = plot( fitresult{8}, xData, yData, 'predobs' );
legend( h, 'Experimental Data', 'Wang', 'Lower bounds (Wang)', 'Upper bounds
(Wang)', 'Location', 'NorthEast' );

% Label axes
axis([0 .25 0 80]);
xlabel( 'Apparent Porosity','FontSize', 10.5, 'FontWeight', 'bold' );
ylabel( yaxistitle ,'FontSize', 10.5,'FontWeight', 'bold' );
```

```
set(gca,'fontsize',10)
set(gcf, 'paperunits', 'inches', 'paperposition', [0 0 5 3.5])
timestamp = datestr(now,'yyyymmdd_HHMMSS');
filename = ['Wang_' timestamp];
print(filename, '-dtiff', '-r600')
saveas(gcf,filename,'fig')
%}

%% Fit: 'MacKenzie'.
% Set up fittype and options.
ft = fittype( '70.420*(1-f1*x+f2*x^2)', 'independent', 'x', 'dependent', 'y'
);
opts = fitoptions( ft );
opts.Display = 'Off';
opts.Lower = [-Inf -Inf];
opts.StartPoint = [0 0];
opts.Upper = [Inf Inf];

% Fit model to data.
[fitresult{9}, gof(9)] = fit( xData, yData, ft, opts );

% Plot fit with data.
figure( 'Name', 'MacKenzie' );
h = plot( fitresult{9}, xData, yData, 'predobs' );
legend( h, 'Experimental Data', 'MacKenzie', 'Lower bounds (MacKenzie)',
'Upper bounds (MacKenzie)', 'Location', 'NorthEast' );

% Label axes
axis([0 .25 0 80]);
xlabel( 'Apparent Porosity','FontSize', 10.5, 'FontWeight', 'bold' );
ylabel( yaxistitle ,'FontSize', 10.5,'FontWeight', 'bold' );

set(gca,'fontsize',10)
set(gcf, 'paperunits', 'inches', 'paperposition', [0 0 5 3.5])
timestamp = datestr(now,'yyyymmdd_HHMMSS');
filename = ['MacKenzie_' timestamp];
print(filename, '-dtiff', '-r600')
saveas(gcf,filename,'fig')
%}
```

APPENDIX C. WEIBULL PROBABILITY PLOTS

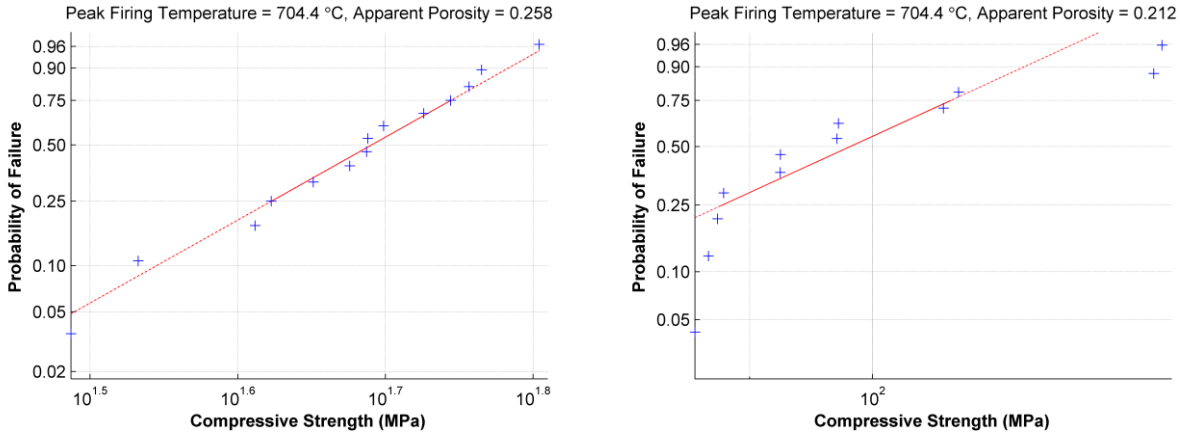

(a) (b)

Figure A-1. Weibull probability plot of compressive strength for specimens densified at 704.4°C: a) unpolished and b) polished.

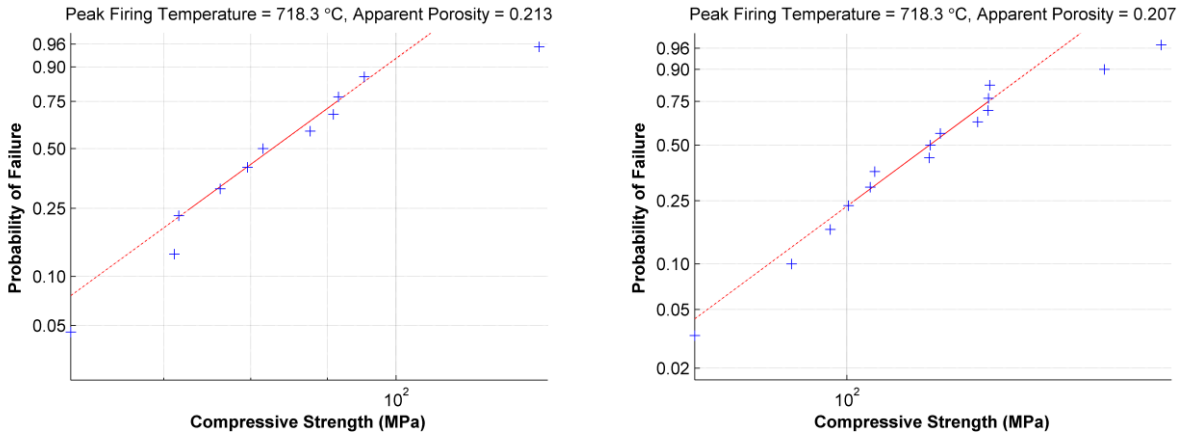

(a) (b)

Figure A-2. Weibull probability plot of compressive strength for specimens densified at 718.3°C: a) unpolished and b) polished.

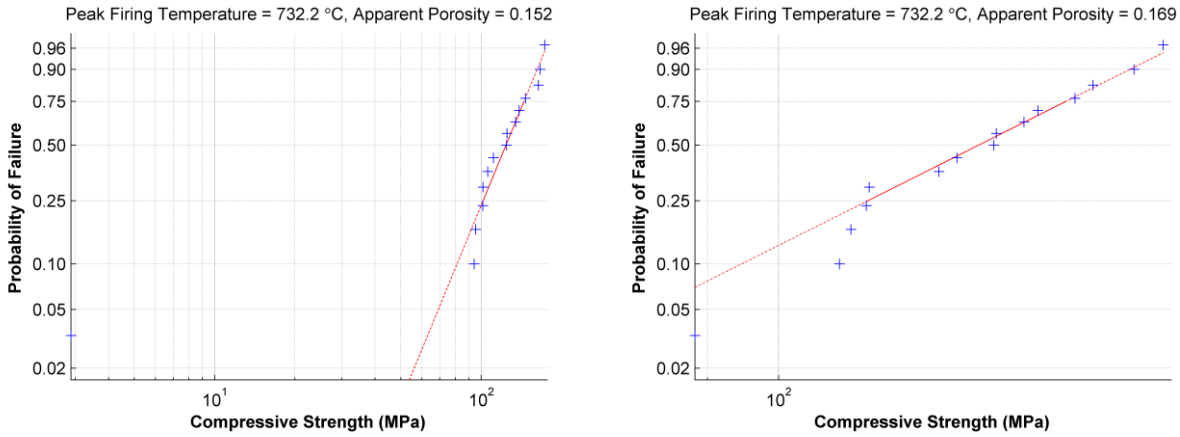

(a) (b)

Figure A-3. Weibull probability plot of compressive strength for specimens densified at 732.2°C: a) unpolished and b) polished.

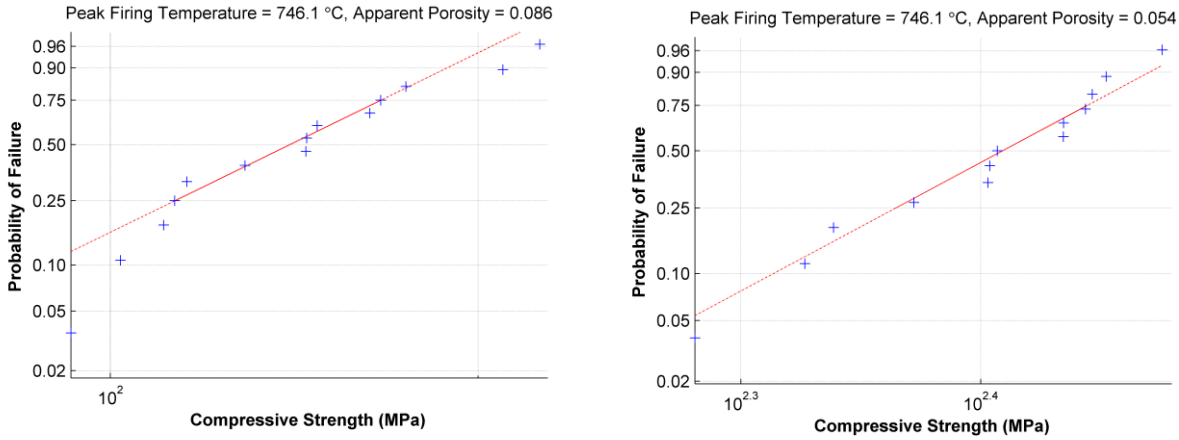

(a) (b)

Figure A-4. Weibull probability plot of compressive strength for specimens densified at 746.1°C: a) unpolished and b) polished.

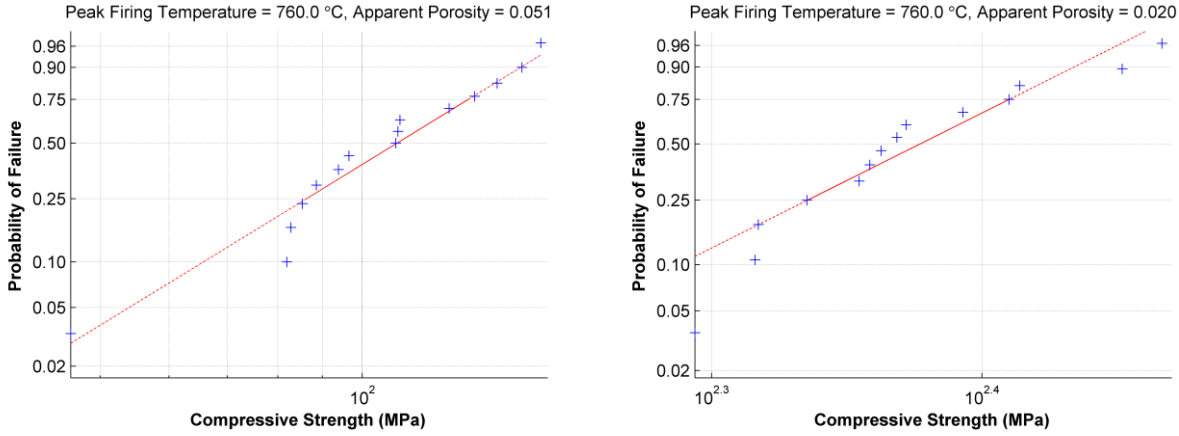

(a) (b)

Figure A-5. Weibull probability plot of compressive strength for specimens densified at 760°C: a) unpolished and b) polished.

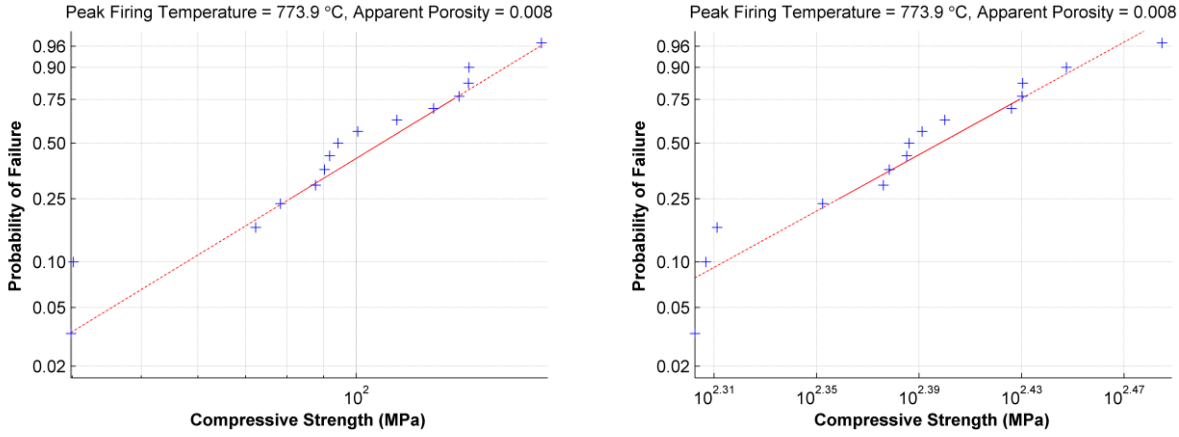

(a) (b)

Figure A-6. Weibull probability plot of compressive strength for specimens densified at 773.9°C: a) unpolished and b) polished.

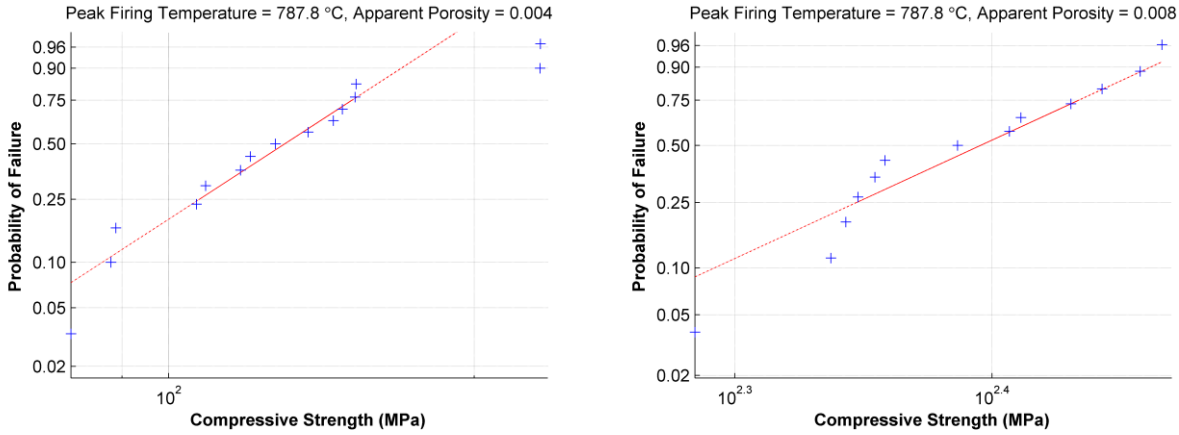

(a) **(b)**

Figure A-7. Weibull probability plot of compressive strength for specimens densified at 787.8°C: a) unpolished and b) polished.

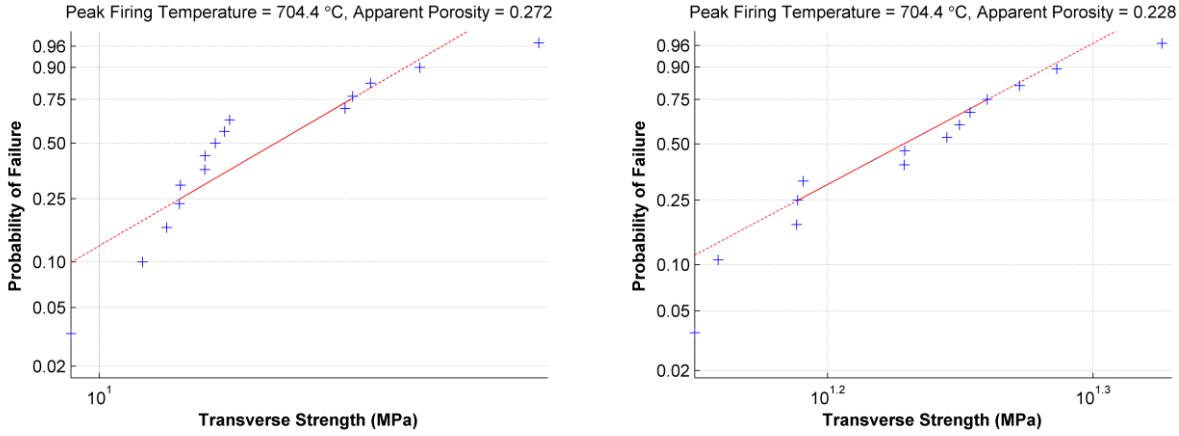

(a) (b)

Figure A-8. Weibull probability plot of transverse strength for specimens densified at 704.4°C: a) unpolished and b) polished.

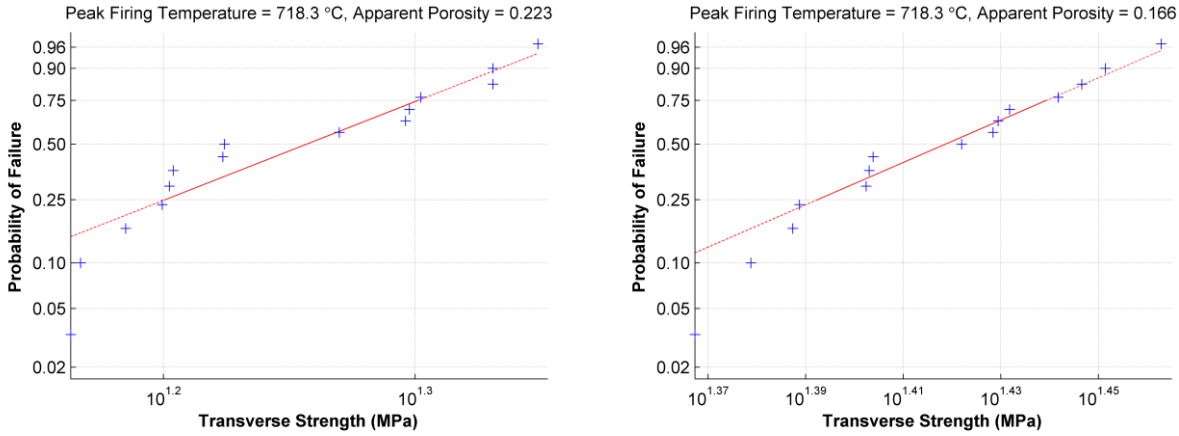

(a) (b)

Figure A-9. Weibull probability plot of transverse strength for specimens densified at 718.3°C: a) unpolished and b) polished.

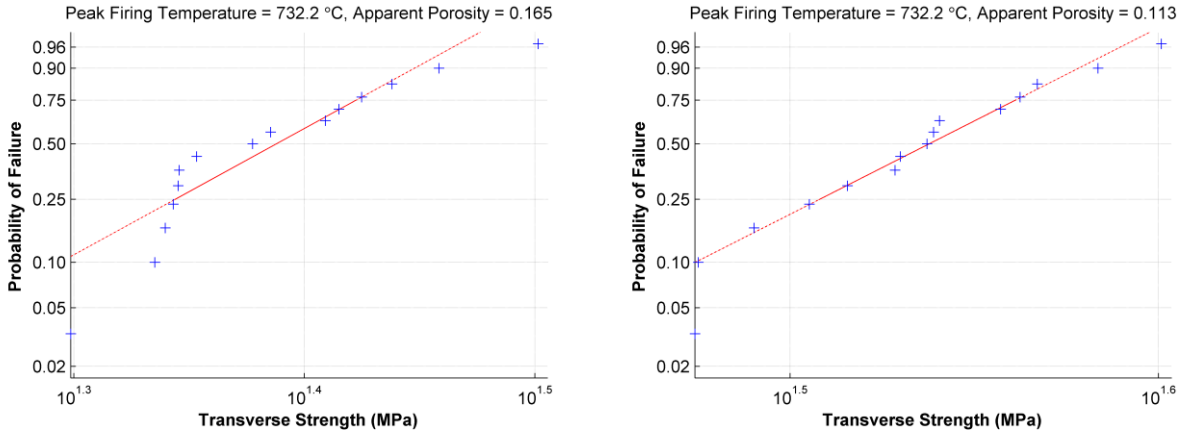

(a) (b)

Figure A-10. Weibull probability plot of transverse strength for specimens densified at 732.2°C: a) unpolished and b) polished.

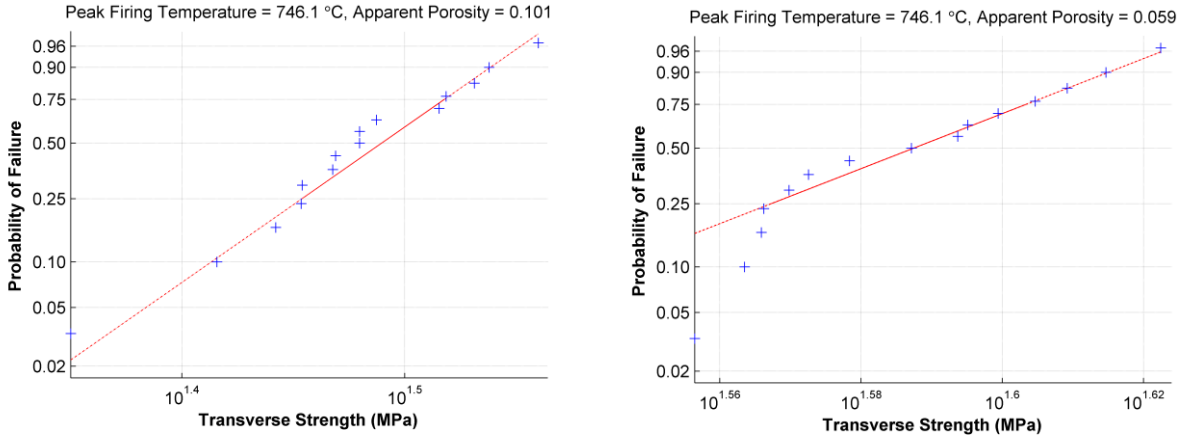

(a) (b)

Figure A-11. Weibull probability plot of transverse strength for specimens densified at 746.1°C: a) unpolished and b) polished.

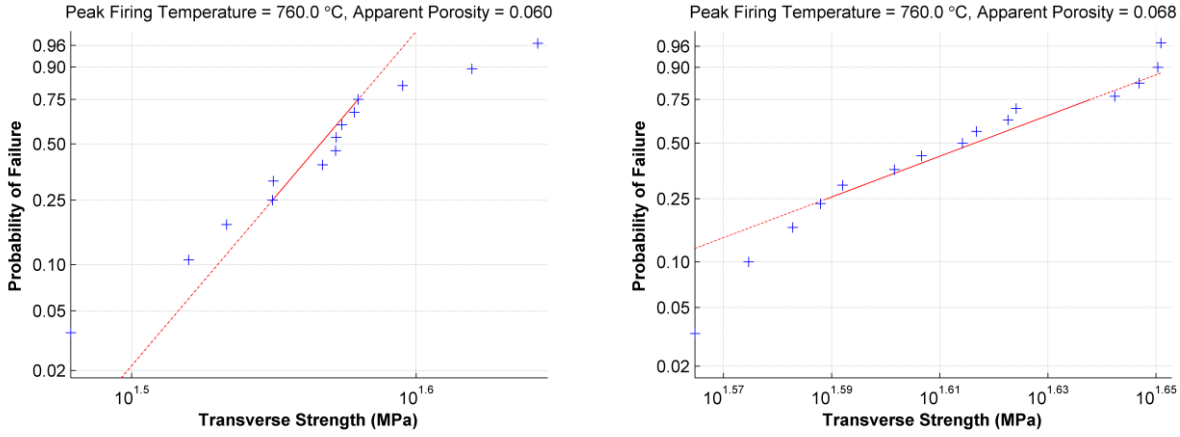

(a) (b)

Figure A-12. Weibull probability plot of transverse strength for specimens densified at 760°C: a) unpolished and b) polished.

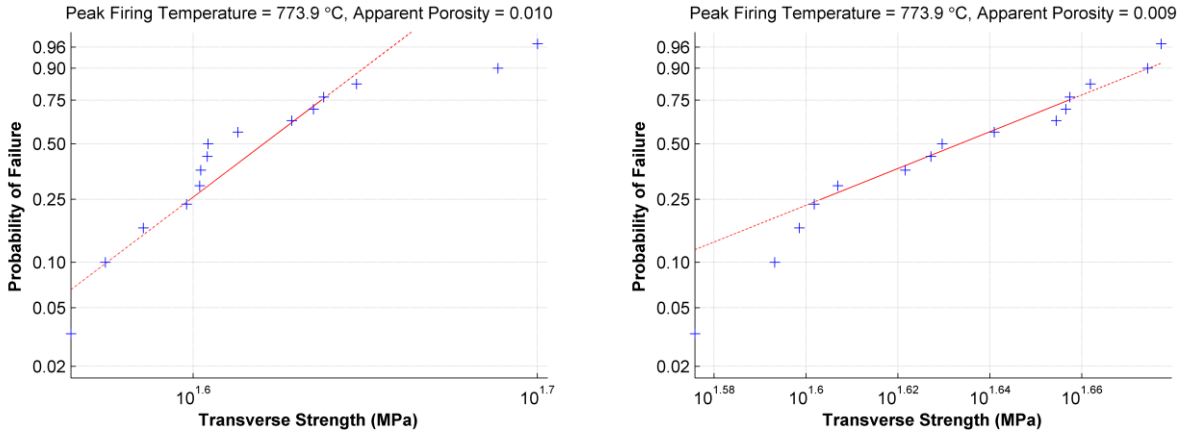

(a) (b)

Figure A-13. Weibull probability plot of transverse strength for specimens densified at 773.9°C: a) unpolished and b) polished.

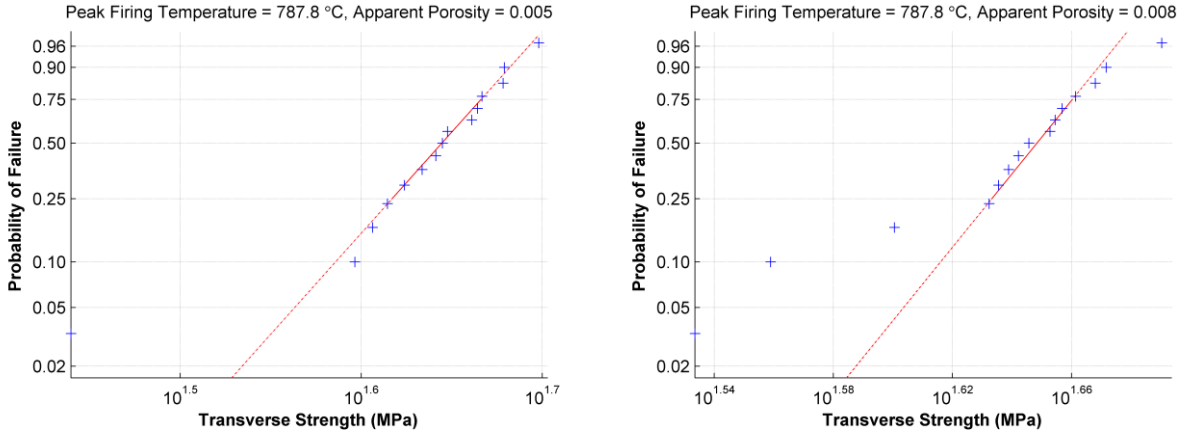

(a) **(b)**

Figure A-14. Weibull probability plot of transverse strength for specimens densified at 787.8°C: a) unpolished and b) polished.